# Chiral symmetry and hadronic measurements on the lattice

**Dissertation**

zur Erlangung des Doktorgrades
der Naturwissenschaften (Dr. rer. nat.)
der naturwissenschaftlichen Fakultät II – Physik
der Universität Regensburg

vorgelegt von

**Stefan Schaefer**

aus Friedrichsdorf

Oktober 2002

Die Arbeit wurde von Prof. Dr. A. Schäfer angeleitet.
Das Promotionsgesuch wurde am 29.10.2002 eingereicht.
Das Kolloquium fand am 17.12.2002 statt.

| | | |
|---|---|---|
| Prüfungsausschuß: | Vorsitzender: | Prof. Dr. M. Maier |
| | 1. Gutachter: | Prof. Dr. A. Schäfer |
| | 2. Gutachter: | Prof. Dr. U. Rößler |
| | weiterer Prüfer: | Prof. Dr. U. Krey |

# Contents

# Chapter 1

# Introduction

Confronting our ideas about nature with our observations is at the heart of every science. As we are made almost entirely out of nuclear matter, this is an obvious object of study. Our knowledge of the structure and interactions of the nucleons is condensed in a SU(3) gauge theory named Quantum Chromodynamics (QCD). It describes the nucleons as built of fermions, called *quarks*, which interact via gauge bosons, the *gluons*.

Unfortunately, it is very hard to confront this theory with observations. This is not only due to the fact that the particles we are dealing with are very small (the typical scale is 1 fm). The theory itself is, both, very hard to define and to solve. Nevertheless, the main features of asymptotic freedom and confinement could be made plausible. Most of the success of the theory is based on its perturbative definition in Minkowski space. But the perturbative treatment is restricted to the high energy region where the coupling constant is small. At lower energies, the coupling constant becomes large and the perturbative expansion is no longer possible.

QCD can be formulated non-perturbatively on the lattice where Euclidean space-time is discretized on a hypercubic lattice with a finite lattice spacing. This serves simultaneously as infrared and ultraviolet cut-off. Furthermore, the discretization makes it possible to put the theory on a computer. Using this formulation, we present Monte Carlo results in three different areas: chiral symmetry breaking, the masses of hadrons and, finally, hadron structure.

What is the objective of these investigations? Chiral symmetry is a symmetry of the QCD Lagrangian with massless quarks. According to Noether's theorem a conservation law is associated with every continuous symmetry. Chiral symmetry should imply a definite handedness for all particles which is conserved by the interactions. However, this is not observed. The symmetry is broken in two ways. First, the quark masses are not zero. But as the masses of the light quarks, which build up the nucleons and the light mesons, are much smaller than those of the hadrons, a remnant of the symmetry should be observable. More important is the *spontaneous breaking* of chiral symmetry. It is a dynamical, purely

non-perturbative effect. The most popular model to describe chiral symmetry breaking is the instanton model. This model makes specific predictions about the dominant gauge field contributions to chiral symmetry breaking. In Chapter 2, we verify some of these predictions in a Monte Carlo simulation of QCD. The implementation of chiral symmetry on the lattice has been a longstanding problem. Only since the second half of the 1990s, procedures to implement chirally symmetric fermionic actions on the lattice have become available. Unfortunately, exact chiral symmetry is numerically very expensive with respect to CPU time. However, good chiral properties of the lattice formulation of the theory are an obvious necessity in a study of chiral symmetry breaking. We use a specific action with approximate chiral symmetry which is numerically much less demanding. So we are able to look into this problem in great detail.

We compute the masses of the light hadrons with the same chirally improved action in Chapter 3. These masses are known to great accuracy and not calculable in perturbation theory. Thus they play a pivotal rôle in comparing the predictions of lattice QCD with nature. For the action we use, this is the first test which checks if it reproduces physical observables reasonably well at finite lattice spacing and volume. The mass of the pseudoscalar meson is of special interest as its dependence on the quark mass is a measure for the chiral properties of the fermionic action.

The structure of the hadrons, especially the nucleons, has been in the focus of interest in QCD for a long time, too. The structure relevant in experiments at very high energy is coded in moments of distribution functions, which can be computed on the lattice. The experimental findings can be reproduced by lattice simulation to satisfactory accuracy (within statistical and systematic errors). In Chapter 4, we use these techniques to get further information about the structure of the proton and the $\Lambda$ hyperon, which is not directly accessible by experiment. We study the spin structure of the $\Lambda$ and its relation to the spin structure of the nucleon. For the proton, we are interested in (higher twist) matrix elements, which are relevant to describe experiments at lower energies. These findings can then be used to test models of QCD.

## 1.1 Overview

In the course of this chapter, we introduce the formulations of lattice QCD which we use. This consists mainly in giving the definitions of the various actions for the gluons and the quarks. Most of it can be found in textbooks, e.g. [MM94]. We give the continuum action for these fields in Sec. 1.2. Afterwards, the basic notation for the lattice on which the theory is discretized is subject of Sec. 1.3. The standard lattice gauge actions are introduced in Sec. 1.4. The various discretizations rely on the fact that only the continuum limit of the theory is fixed. At finite lattice spacing, there is a certain arbitrariness which can be utilized to

improve the properties of the theory. Before describing the discretizations of the fermion part of the QCD action (Sec. 1.6), we first give a collection of results on chiral symmetry and its breaking. It has long been believed that it is impossible to construct a theory with chiral symmetry and the correct continuum limit on a lattice. The main problem has always been the appearance of so-called doublers. These are degenerate and unwanted particles which do not vanish in the continuum limit. The first cure to this problem has been given by Wilson. He suggested an action (see Sec. 1.6.2) which gives the doublers a mass which grows in the continuum limit; hence they decouple. Unfortunately, this action breaks chiral symmetry explicitly. The solution to this problem is given by the Ginsparg-Wilson relation [GW82], which was rediscovered about seven years ago. In particular, we give the definition of an approximate solution of this relation, the chirally improved fermions developed by Gattringer, Hip, and Lang [GHL01], which is used in this work.

### 1.1.1 The publications

A lot of the results we are going to present are already published. Concerning chiral symmetry these can be found in:

- C. Gattringer, M. Göckeler, P.E.L. Rakow, S. Schaefer and A. Schäfer, "Properties of near zero modes and chiral symmetry breaking," Nucl. Phys. B **617**, 101 (2001) [arXiv: hep-lat/0107016].

- C. Gattringer, M. Göckeler, P.E.L. Rakow, S. Schaefer and A. Schäfer, "A comprehensive picture of topological excitations in finite temperature lattice QCD," Nucl. Phys. B **618**, 205 (2001) [arXiv: hep-lat/0105023].

- C. Gattringer, R. Hoffmann and S. Schaefer, "The topological susceptibility of SU(3) gauge theory near $T_c$," Phys. Lett. B **535** (2002) 358 [arXiv: hep-lat/0203013].

- C. Gattringer, R. Hoffmann and S. Schaefer, "Setting the scale for the Lüscher-Weisz action," Phys. Rev. D **65**, 094503 [arXiv: hep-lat/0112024].

Additional information on hadron spectroscopy with the chirally improved and fixed point Dirac operator is presented in:

- C. Gattringer, M. Göckeler, P. Hasenfratz, S. Hauswirth, K. Holland, T. Jörg, K.J. Juge, C.B. Lang, F. Niedermayer, P.E.L. Rakow, S. Schaefer, A. Schäfer "Quenched QCD with fixed-point and chirally improved fermions," [arXiv: hep-lat/0209099].

The various aspects of hadron structure are investigated in:

- M. Göckeler, R. Horsley, D. Pleiter, P.E.L. Rakow, S. Schaefer, A. Schäfer and G. Schierholz, [QCDSF Collaboration], "A lattice study of the spin structure of the $\Lambda$ hyperon," Phys. Lett. B **545** (2002) 112 [arXiv:hep-lat/0208017].
- S. Schaefer, A. Schäfer and M. Stratmann, "Impact of higher order and soft gluon corrections on the extraction of higher twist effects in DIS," Phys. Lett. B **514**, 284 (2001) [arXiv: hep-ph/0105174].
- M. Göckeler , R. Horsley, B. Klaus, D. Pleiter, P.E.L. Rakow, S. Schaefer, A. Schäfer and G. Schierholz, "A lattice evaluation of four quark operators in the nucleon," Nucl. Phys. B **623**, 287 (2002) [arXiv: hep-lat/0103038].

## 1.2 The continuum action

QCD is defined through its Lagrangian density which can be formulated using the following conventions. We work in four dimensional Euclidean space-time with time direction 4. The spatial directions are labeled 1 to 3. The quark fields of flavor $f$ are denoted by $\psi^f(x,d,c) \equiv \psi_d^{f,c}(x)$, where $x$ is the space-time index, $d$ the Dirac index and $c$ the color index. Alternatively, the flavor is given by the corresponding letter ($u$, $d$, ...) substituting the $\psi$. As these fields have complex values, the Lagrangian is also a functional of $\bar{\psi}$ with

$$\bar{\psi}_d^{f,c}(x) \equiv (\psi_{d'}^{f,c})^+(x)(\gamma_4)_{d',d} \; . \tag{1.1}$$

A representation of the $\gamma$ matrices is given in Appendix A. Here, as we do in the following, we use the convention that repeated indices are summed over. If no explicit sum is given, the indices of the $\gamma$ matrices are always contracted with the Dirac indices.

The second kind of fields involved is the SU(3) gauge field $A_\mu(x)$ with

$$A_\mu(x) = -igA_\mu^a(x)t_a \; . \tag{1.2}$$

The spin–1 gauge bosons are called gluons. $a$ is again the color index and $\mu$ is the Lorentz index. $g$ is the bare strong coupling constant. The $3 \times 3$ matrices $t_a$ are the Gell-Mann matrices, see App. A, which are the generators of the su(3) algebra. It is useful to define the field strength tensor $F_{\mu\nu}(x)$ by

$$F_{\mu\nu} = \partial_\mu A_\nu(x) + \partial_\nu A_\mu(x) + [A_\mu(x), A_\nu(x)] \, . \tag{1.3}$$

In this formula, the non-abelian character comes into play via the last term. It generates the self interaction of the gauge field. The Lagrangian of the gauge field reads in terms of the field strength tensor

$$\mathcal{L}_{\rm G} = -\frac{1}{2g^2} \, {\rm tr} \, F_{\mu\nu}F^{\mu\nu} \; . \tag{1.4}$$

This describes the dynamics of the gluon field. It contains the free propagation as well as the three and four gluon vertices.

The fermion dynamics is encoded in the Dirac operator $D$ for a massless quark

$$D = \gamma_\mu(\partial_\mu + A_\mu) \ . \tag{1.5}$$

The fermion part of the Lagrangian is given by the sum over the quark flavors

$$\mathcal{L}_{\mathrm{F}} = \sum_f \bar{\psi}^f(x)(D + m^f)\psi^f(x) \tag{1.6}$$

with $m^f$ the mass of the quark of flavor $f$. It describes the motion of a massive spin–$\frac{1}{2}$ particle which is coupled to a gauge field. The full Lagrangian $\mathcal{L}$ is the sum of the two contributions Eq. (1.4) and Eq. (1.6). The QCD action $S$ is the integral over the full Euclidean space-time of the Lagrangian

$$S[\bar{\psi}, \psi, A] = \int \mathrm{d}^4x \left(\mathcal{L}_{\mathrm{F}}[\bar{\psi}, \psi, A] + \mathcal{L}_{\mathrm{g}}[A]\right) \tag{1.7}$$

The major ingredient of the action (1.7) is its invariance under local SU(3) gauge transformation $\Lambda(x)$. Such a transformation acts on the fields as follows

$$\begin{aligned} A'_\mu(x) &= \Lambda(x)A_\mu(x)\Lambda^{-1}(x) + \frac{i}{g}[(\partial_\mu\Lambda(x))\Lambda^{-1}(x)] \\ \psi'(x) &= \Lambda(x)\psi(x) \\ \bar{\psi}'(x) &= \bar{\psi}(x)\Lambda^{+}(x) \end{aligned} \tag{1.8}$$

The gluonic part of the action Eq. (1.4) is gauge invariant as the field strength $F_{\mu\nu}$ transforms under a local gauge transformation as

$$F'_{\mu\nu}(x) = \Lambda(x)F_{\mu\nu}(x)\Lambda^{-1}(x) \tag{1.9}$$

The fermionic part of the action is gauge invariant, too. The form of the coupling of the gauge fields to the quarks is exactly such that the fermionic action is gauge invariant (gauge principle).

## 1.3 Discretization I: The lattice

In order to put the theory on a lattice, one has to discretize space-time. The purpose of doing so is twofold. First we want to do a computer simulation. Therefore we need a defined way to cut the theory from an infinite number of degrees of freedom to a finite number. Furthermore, if we want to compute a quantity in a quantum field theory, we always need a regularization. The regularization methods used in perturbative QCD, e.g., dimensional regularization, are only applicable within the framework of this approximation. The lattice regularization

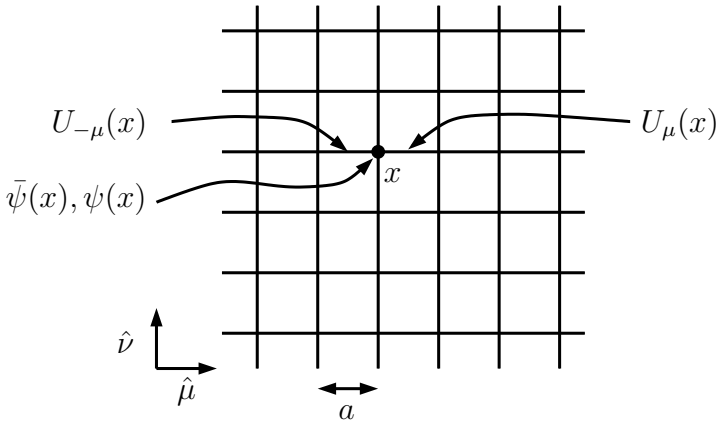


Figure 1.1: In the lattice discretization, the fermion fields $\bar{\psi}(x)$ and $\psi(x)$ are put on the sites of a hypercubic lattice. The link variables live on the links between the sites. Here the $\mu$-$\nu$-plane of the lattice is drawn. The sites are separated by the lattice spacing $a$.

provides us with a non-perturbative ultraviolet and infrared cut-off and thus with an important ingredient of a definition of the theory.

The hypercubic lattice, see Fig. 1.1, is given by sites at the points $x$ separated by the *lattice spacing* $a$

$$x = a\,(n_1,\, n_2,\, n_3,\, n_4) \quad \text{with} \quad n_i \in \{0, \ldots, L_i - 1\}\ . \tag{1.10}$$

The link connecting the point $x$ with the point $x+\hat{\mu}$ ($\hat{\mu}$ being the vector of length $a$ in direction $\mu$) is denoted by $(x, \mu)$.

On such a hypercubic lattice, the quark fields are located on the sites, i.e., the corners of the elementary hypercubes. The variables describing the gauge fields are located on the links between these points. This is a sensible choice as the gauge fields have a vector index $\mu$ and are therefore oriented quantities.

Unfortunately, this regularization breaks the space-time symmetries. The full SO(4) symmetry is broken to the hypercubic group H(4) by the discretization on a hypercubic lattice. Furthermore, the translational invariance of the theory is only present in integer multiples of the lattice spacing $a$. However, in the *continuum limit* $a \to 0$ all theses symmetries are restored.

## 1.4 Discretization II: Gauge actions

The gauge field is a vector field. It has an index which is related to the space-time direction. Thus, it is natural to put it on the links of the lattice as from each site there emerge links in all directions of the space-time. These links, however, connect two sites with a finite separation. The *local* gauge invariance of the

continuum theory Eq. (1.8) has to be reflected by the transformation properties of the lattice variables which describe the gauge field. To this end the *parallel transporters* are introduced which correspond to the path ordered exponentials of the gauge field. On a link $(x, \mu)$ the parallel transporter is denoted by $U_\mu(x)$. The $U_\mu(x)$ are elements of the gauge group SU(3). They are connected to the gauge field $A_\mu(x)$ via

$$U_\mu(x) = e^{aA_\mu(x)} \ . \tag{1.11}$$

Under a gauge transformation $\Lambda(x)$ the parallel transporters transform as

$$U'_\mu(x) = \Lambda(x) U_\mu(x) \Lambda^{-1}(x + \hat{\mu}) \ . \tag{1.12}$$

This relation makes the parallel transporters useful for constructing gauge invariant terms which involve quark fields at different lattice points (as is necessary to construct derivatives). The link variable is defined for negative indices by

$$U_{-\mu}(x) \equiv U^+_\mu(x - \hat{\mu}) \ . \tag{1.13}$$

The discretized action is constructed as a sum of products of the parallel transporters along closed paths. This guarantees its gauge invariance. We use different discretizations of the gauge action. In Sec. 1.4.1 we start with the most simple one, the Wilson gauge action. Then, in Sec. 1.4.2, an action, which improves the continuum limit $a \to 0$ is introduced, followed by a so-called smearing procedure, which smoothes ultra-violet fluctuations in Sec. 1.4.3.

### 1.4.1 The Wilson gauge action

The simplest kind of closed paths on a hypercubic lattice are squares with edges of length $a$, the so-called plaquettes. These can be characterized by one site $x$ and vectors of length $a$ in positive directions $\mu$, $\nu$ and consist of the points

$$(x, x + \hat{\mu}, x + \hat{\nu} + \hat{\mu}, x + \hat{\nu}) \ . \tag{1.14}$$

A short hand notation is $p = (x; \mu, \nu)$. The gauge invariant plaquette variable $U_p$ is the product of the parallel transporters along such a plaquette $p$.

$$U_p \equiv U_{\mu,\nu}(x) \equiv U_\mu(x) U_\nu(x + \hat{\mu}) U_{-\mu}(x + \hat{\nu} + \hat{\mu}) U_{-\nu}(x + \hat{\nu}) \tag{1.15}$$

This is visualized in Fig. 1.2. We start at point $x$ and multiply the link variables along the square. The variables into negative direction are defined in Eq. (1.13). From this quantity Wilson [Wil74] has constructed the *plaquette action*, which is frequently called Wilson gauge action,

$$S[U] = \sum_p S_p(U_p) = \sum_x \sum_{1 \le \mu < \nu \le 4} S_p(U_{\mu,\nu}(x)) \tag{1.16}$$

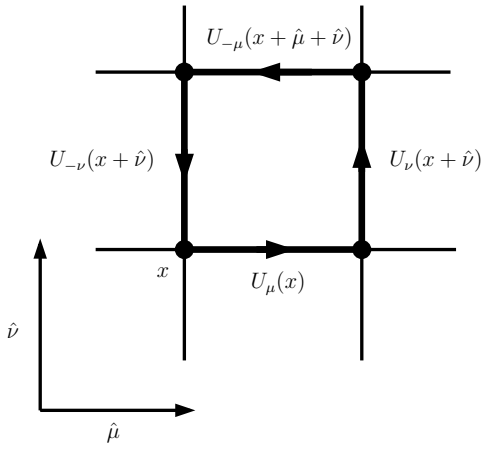


Figure 1.2: The plaquette variable $U_{\mu,\nu}(x)$ is the product the four link variables forming a square. We plotted the $\mu$-$\nu$–plane of the lattice. One corner of the square is in $x$. It lies in the $\mu$-$\nu$–plane and is oriented in positive direction.

with the single plaquette term for the general SU($N$) theory

$$S_p(U_p) = \frac{\beta}{N}\mathrm{Re}\,\mathrm{tr}\,(\mathbf{1} - U_p). \tag{1.17}$$

Such discretizations are in a way arbitrary. The only guide is the continuum limit, i.e. the limit $a \to 0$, where the continuum action has to be approached. This arbitrariness can be used to tune the behavior of the theory. The action can be manipulated by adding terms which vanish in the limit $a \to 0$ but improve the continuum limit for physical quantities. Such improvement programs are discussed later on.

It is fairly easy to see that the plaquette action reproduces the continuum action in the limit $a \to 0$. Using the identification $U_\mu(x) = \exp(igaA^c_\mu(x)t^c)$ and

$$a\partial_\mu A_\nu(x) = A_\nu(x+\hat{\mu}) - A_\nu(x) + \mathcal{O}(a^2)\ . \tag{1.18}$$

the plaquette action turns in the limit $a \to 0$ to

$$S = -\frac{\beta}{4N}\sum_x a^4 \mathrm{tr}\, F_{\mu\nu}(x)F_{\mu\nu}(x) + \mathcal{O}(a^2)\ , \tag{1.19}$$

which leads to a relation between the coupling constant in the continuum action $g$ and the $\beta$ in the Wilson action

$$\beta = \frac{2N}{g^2}\ . \tag{1.20}$$

Finally, we remark that by rescaling the gauge fields $A$, we can get rid of explicit factors of $a$ which amounts to putting $a$ to 1. The lattice constant is determined

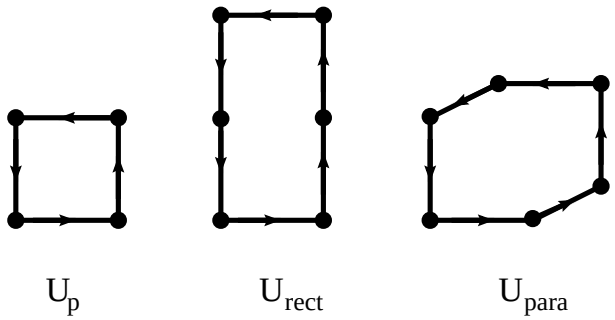


Figure 1.3: The three contributions to the Lüscher-Weisz action. On left we show the standard plaquette term from the Wilson action. In the middle the rectangle contribution. On the right we depict the so-called parallelogram which extends in three space-time directions.

by the comparison of observables measured in a Monte Carlo simulation and the experimental value. This procedure is a consequence of the dynamical generation of the scale in QCD.

### 1.4.2 The Lüscher-Weisz Action

We have seen that the Wilson gauge action has discretization errors of order $a^2$. This can spoil physical results at finite $a$ and make the continuum limit difficult. In particular rotational invariance suffers from these corrections. Therefore an action [CMP83, LW85], commonly called Lüscher-Weisz action, has been proposed in which terms are added to the Wilson gauge action in such a way that the $\mathcal{O}(a^2)$ corrections cancel. These terms are gauge paths of rectangular form and a so-called parallelogram.

$$\begin{aligned} S[U] =& \beta_1 \sum_{\mathrm{p}} \frac{1}{3}\mathrm{Re}\,\mathrm{tr}\,(1 - U_{\mathrm{p}}) + \beta_2 \sum_{\mathrm{rect}} \frac{1}{3}\mathrm{Re}\,\mathrm{tr}\,(1 - U_{\mathrm{rect}}) \\ &+ \beta_3 \sum_{\mathrm{para}} \frac{1}{3}\mathrm{Re}\,\mathrm{tr}\,(1 - U_{\mathrm{para}}) \end{aligned} \tag{1.21}$$

The first sum runs over all plaquettes, the second sum over all $2 \times 1$ rectangles, see Fig. 1.3 on the left and in the middle. Starting on a site $x$ the rectangle which extends 1 unit in $\mu$- and 2 units in $\nu$-direction is given by

$$U_{\mathrm{rect}}(x;\mu,\nu) = U_\mu(x)U_\nu(x+\hat{\mu})U_\nu(x+\hat{\mu}+\hat{\nu})U_\mu^+(x+2\hat{\nu})U_\nu^+(x+\hat{\nu})U_\nu^+(x) \tag{1.22}$$

The third sum in Eq. (1.21) is over all $1 \times 1 \times 1$ parallelograms. Such a parallelogram starting at site $x$ in the $\alpha$-$\mu$-$\nu$–slice is given by, see Fig. 1.3 on the

| $\beta_1$ | 8.00 | 8.10 | 8.20 | 8.30 | 8.45 | 8.60 |
|---|---|---|---|---|---|---|
| ${u_0}^4$ | 0.62107(3) | 0.62894(3) | 0.63599(3) | 0.64252(3) | 0.65176(3) | 0.66018(3) |
| $\beta_2$ | −0.54574 | −0.54745 | −0.54998 | −0.55332 | −0.55773 | −0.56345 |
| $\beta_3$ | −0.05252 | −0.05120 | −0.05020 | −0.04953 | −0.04829 | −0.04755 |
| $a$[fm] | 0.136(1) | 0.125(1) | 0.115(1) | 0.105(1) | 0.095(1) | 0.084(1) |

Table 1.1: Parameters for the Lüscher-Weisz action. We list the values of the $\beta_i$,the expectation value of the plaquette ${u_0}^4 = \mathrm{Re\ tr}\langle U_{pl}\rangle/3$ and the corresponding lattice constants $a$.

right

$$U_{\mathrm{para}}(x;\alpha,\mu,\nu) = \\ U_\alpha(x)U_\mu(x+\hat{\alpha})U_\nu(x+\hat{\alpha}+\hat{\mu})U_\alpha^+(x+\hat{\mu}+\hat{\nu})U_\mu^+(x+\hat{\nu})U_\nu^+(x) \quad (1.23)$$

The coefficients $\beta_2$ and $\beta_3$ of the rectangles and parallelograms have been determined within the framework of tadpole improved perturbation theory [LM93]. They are given in terms of the expectation value of the plaquette variable $\frac{1}{3}\mathrm{tr}\,\langle U_{\mathrm{pl}}\rangle$ [ADL$^+$95].

$$\beta_2 = -\frac{\beta_1}{20u_0^2}[1+0.4805\alpha], \qquad \beta_3 = -\frac{\beta_1}{u_0^2}0.03325\alpha\ . \quad (1.24)$$

with

$$u_0 = (\frac{1}{3}\mathrm{Re\ \ tr}\,\langle U_{\mathrm{pl}}\rangle)^{1/4} \qquad \text{and} \qquad \alpha = -\frac{\ln(\frac{1}{3}\mathrm{Re\ \ tr}\,\langle U_{\mathrm{pl}}\rangle)}{3.06839} \quad (1.25)$$

The values which we use in the actual computations can be found in Table 1.1.

In QCD, the scale is generated dynamically. So, by comparing with physical observables, we have to fix the lattice spacing $a$. A popular method is measuring the static quark-antiquark potential and computing the Sommer parameter $r_0$ [Som94, ALPHA98]. This $r_0$ is the distance between the quark and the antiquark at which the force $F(r_0)$ is given by

$$r_0^2 F(r_0) = 1.65\ . \quad (1.26)$$

The constant on the right hand side of Eq. (1.26) is chosen such [ALPHA98] that $r_0 = 0.5\,\mathrm{fm}$ from the phenomenological description of heavy quark systems. The dependence of the Sommer parameter and the lattice spacing on $\beta_1$ is shown in Fig. 1.4. As an interpolating function valid in the range of $\beta_1$ between 8.0 and 8.6 we give in [GHS02a]

$$\ln(r_0/a) \ = \ 1.55354 \ + \ 0.79840\,(\beta_1 - 8.3) \ - \ 0.09533\,(\beta_1 - 8.3)^2\ . \quad (1.27)$$

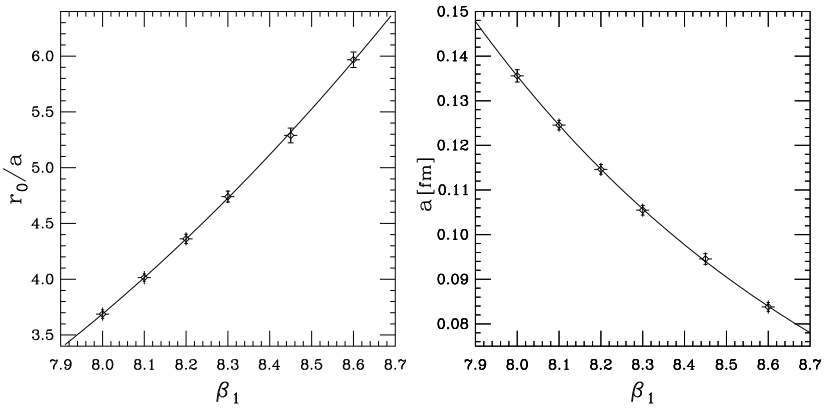


Figure 1.4: The Sommer parameter $r_0/a$ and the lattice spacing $a$ as a function of $\beta_1$ for the Lüscher-Weisz action. The solid lines are the fit given in Eq. (1.27)

It was noted in [GHL01] that the expectation value of the plaquette $\langle U_{\rm pl}\rangle/3$ for the Lüscher-Weisz action is (for the same lattice spacing) considerably closer to 1 than for the Wilson action. Thus the Lüscher-Weisz action tends to suppress ultraviolet fluctuations and typically one obtains better results for approximate Ginsparg-Wilson fermions [GHL01] as well as for the overlap Dirac operator [LDLZ01], see Sec. 1.6.4.

### 1.4.3 HYP smearing

Many simulations suffer from ultraviolet fluctuations as well as from a bad scaling behavior introduced by the gauge action. To cure this problem fat link gauge actions have been introduced. These start from a given gauge configuration and replace each link by a sum over extended paths from the neighborhood of this link. By using only a finite number of paths close to the original link one stays in the same universality class as the original action [HK01]. In the continuum limit $a \to 0$ both actions will lead to the same result. However, measurements are made with a finite $a$. It is important to construct a fattening procedure which is a good compromise between the smoothening of the fields and not destroying the short distance behavior of the theory.

Such a smearing procedure is the *hypercubic blocking (HYP)* introduced in [HK01]. It has proven for the static quark-antiquark potential to reduce the errors significantly and give the same results as the original action [HHK02].

The construction is made in three steps. In each of these steps a link is substituted by a combination of the original link and the links which are part of an elementary hypercube attached to this link

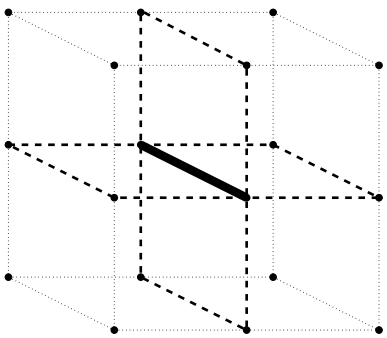

Figure 1.5: Visualization of the construction of the fat links in three dimensions. The fat link in the middle is constructed out of the staples attached to it (dashed lines). Each of those has been constructed in a similar way but with less staples due to the restrictions in the sums of Eq. (1.28).

$$
\begin{aligned}
\overline{V}_{x,\mu;\nu\,\rho} &= \mathcal{P}_{\mathrm{SU(3)}}\left[(1-\alpha_3)U_\mu(x) + \frac{\alpha_3}{2}\sum_{\pm\eta\neq\rho,\nu,\mu} U_\eta(x)U_\mu(x+\hat{\eta})U_\eta^+(x+\hat{\mu})\right], \\
\widetilde{V}_{x,\mu;\nu} &= \mathcal{P}_{\mathrm{SU(3)}}\left[(1-\alpha_2)U_\mu(x) + \frac{\alpha_2}{4}\sum_{\pm\rho\neq\nu,\mu} \overline{V}_{x,\rho;\nu\,\mu}\overline{V}_{x+\hat{\rho},\mu;\rho\,\nu}\overline{V}^+_{x+\hat{\mu},\rho;\nu\,\mu}\right], \\
V_{x,\mu} &= \mathcal{P}_{\mathrm{SU(3)}}\left[(1-\alpha_1)U_\mu(x) + \frac{\alpha_1}{6}\sum_{\pm\nu\neq\mu} \widetilde{V}_{x,\nu;\mu}\widetilde{V}_{x+\hat{\nu},\mu;\nu}\widetilde{V}^+_{x+\hat{\mu},\nu;\mu}\right].
\end{aligned}
\tag{1.28}
$$

In the first step intermediate fields $\overline{V}_{x,\mu;\nu\,\rho}$ are created from the thin-link variables $U_\mu(x)$ (indices $x$ run over all sites of the lattice and $\mu$, $\nu$, $\rho$, and $\eta$ over the four directions). As this new link variable is not necessarily in the gauge group, a reprojection $\mathcal{P}_{\mathrm{SU(3)}}$ has to be done. In the second step the intermediate fields $\overline{V}_{x,\mu;\nu\,\rho}$ are blocked into a second set of intermediate fields $\widetilde{V}_{x,\mu;\nu}$ which in the third step are transformed into the final fields $V_{x,\mu}$, see Fig. 1.5. The restrictions on the indices $\mu$, $\nu$, and $\rho$ implemented in the sums in Eqs. (1.28) ensure that $V_{x,\mu}$ contains only contributions from the hypercubes attached to the link $(x,\mu)$. The parameters $\alpha_1, \alpha_2$ and $\alpha_3$ determine the admixture of staples in each step of the blocking process. These parameters were optimized [HK01] to minimize the fluctuations of the plaquette. Their values are given by $\alpha_1 = 0.75$, $\alpha_2 = 0.6$, and $\alpha_3 = 0.3$.

## 1.5 Chiral Symmetry

The next topic is the discretization of the Dirac operator. In order to understand the arising difficulties, we first have to make a digression on chiral symmetry

which is a symmetry of the QCD Lagrangian with massless quarks. The chiral symmetry transformation is in the continuum

$$\psi_d^c(x) \longrightarrow [e^{-i\omega\gamma_5}]_{dd'}\psi_{d'}^c(x) \qquad \bar{\psi}_d^c(x) \longrightarrow \bar{\psi}_{d'}^c(x)[e^{-i\omega\gamma_5}]_{d'd}\,. \tag{1.29}$$

This symmetry should be manifest as a definite handedness of the particles which is conserved in strong interaction processes. This is not observed. Chirality is broken in two ways.

- The quark masses are non-zero. However, as the $u$ and $d$ quark masses are small ($m_u = 1 \ldots 5$ MeV, $m_d = 3 \ldots 9$ MeV [G$^+$00]) compared to the hadron masses ($> 100$ MeV) the symmetry is at least approximately fulfilled.

- The dynamical generation of a chiral condensate

  $$\langle\bar{\psi}\psi\rangle \neq 0\,. \tag{1.30}$$

  This expression is not invariant under the chiral transformation Eq. (1.29). Therefore, a non-vanishing value indicates that chiral symmetry is not a symmetry of the full theory.

For quarks with zero mass, chiral symmetry is *spontaneously* broken. The Goldstone theorem tells us that for each generator of such a broken symmetry we expect one *massless* Goldstone boson in the particle spectrum (for details see, e.g., [IZ80]). For two massless quarks we have a SU(2) chiral symmetry. It has three generators, e.g., the Pauli matrices. The three Goldstone particles corresponding to these are identified with the three pions $\pi^\pm$ and $\pi^0$. However, their masses are non-zero, 139 MeV and 135 MeV, respectively. The origin of these masses lies in the finite quark masses, i.e., in the explicit breaking of chiral symmetry. This is quantified by the *Gell-Mann–Oakes–Renner relation* [GMOR68]. It relates the pion mass $m_\pi$, the pion decay constant $f_\pi$ and the chiral condensate $\langle\bar{\psi}\psi\rangle$ for mass degenerate $u$ and $d$ quarks with $m_u = m_d = m_q$

$$f_\pi^2 m_\pi^2 = -2m_q\langle\bar{\psi}\psi\rangle \tag{1.31}$$

The square of the pion mass is proportional to the quark masses. It remains to remark that the formation of a chiral condensate is a purely non-perturbative effect.

## 1.6 Discretization III: The Dirac Operator

The fermion part of the QCD action in the continuum is given by a sum over the actions for the individual flavors $f$

$$\begin{aligned} S[\bar{\psi},\psi,A] &= \sum_f \int \mathrm{d}^4x\, \bar{\psi}_d^{f,c}(x)\left[(\gamma_\mu)_{d,d'}(\delta_{c,c'}\partial_\mu + A_\mu(x)_{c,c'}) + m^f\delta_{d,d'}\delta_{c,c'}\right]\psi_{d'}^{f,c'}(x) \\ &\equiv \sum_f \int \mathrm{d}^4x\, \bar{\psi}^f(D+m^f)\psi^f \end{aligned} \tag{1.32}$$

with $\psi^f$ the fermion field of flavor $f$ and $m^f$ its mass. Basically, we are left with the problem of a discretization of the derivative in the continuum Dirac operator. It turns out that this is a very difficult task. The naïve discretization by a difference fails as it produces so-called doublers, i.e., additional mass degenerate states at each corner of the Brillouin zone. This problem is discussed in Sec. 1.6.1.

A general discretization of the derivative involves the quark fields at two different sites. So the Dirac operator is a matrix in the space-time indices and the action for a single flavor takes the following form

$$S[\bar{\psi},\psi,A] = \sum_{x,x'} \bar{\psi}_d^c(x)(D(x,d,c;x',d',c') + m\delta_{d,d'}\delta_{c,c'})\psi_{d'}^{c'}(x') \tag{1.33}$$

where we have rescaled the fields such that the lattice spacing disappears. The Dirac operator depends on the gauge field through products of link variables along paths connecting the quark fields at point $x$ and $x'$. Thereby, the whole part of the action is made gauge invariant. This is exactly the requirement that leads to the specific form of the coupling in the continuum.

The Dirac operator on the lattice should have as many of the continuum properties as possible. Apart from the correct behavior under gauge transformations these are the invariance of the action under charge conjugation, parity, rotations and translations. Furthermore the Dirac operator is required to be $\gamma_5$-hermitian

$$D\,\gamma_5 \;=\; \gamma_5\,D^+\,. \tag{1.34}$$

The next sections are organized as follows. We first discuss the naïve discretization of the Dirac operator and its failure. Then one of the first solutions, the Wilson fermions which explicitly break chiral symmetry, is given in Sec. 1.6.2. The continuum limit is improved by the clover fermions which are subject of Sec. 1.6.3. The final solution of the problem are operators, which solve the Ginsparg-Wilson equation. They are discussed in Sec. 1.6.4.

### 1.6.1 Naïve discretization

In the naïve discretization, the derivative $\partial_\mu \psi(x)$ of the continuum fermion action Eq. (1.32) is substituted by the symmetric nearest neighbor difference

$$\partial_\mu \psi(x) \longrightarrow \frac{1}{2a}(\psi(x+\hat{\mu}) - \psi(x-\hat{\mu})) \tag{1.35}$$

This leads to the following discretization of the free fermionic action with $a = 1$:

$$S[\bar{\psi}, \psi] = \sum_x \left[ m\bar{\psi}^c_d(x)\psi^c_d(x) - \frac{1}{2}\sum_\mu \bar{\psi}^c_d(x+\hat{\mu})(\gamma_\mu)_{d,d'}\psi^c_{d'}(x) \right] . \tag{1.36}$$

where we use the following convention for the summation and the $\gamma$-matrices with negative index

$$\sum_\mu \equiv \sum_{\mu=\pm 1}^{\pm 4} \qquad \text{and} \qquad \gamma_{-\mu} = -\gamma_\mu \ . \tag{1.37}$$

If we suppress the dependence on the gauge fields, Eq. (1.36) corresponds to

$$D(x,d;x',d') = \frac{1}{2}(\delta_{x+\hat{\mu},x'} - \delta_{x-\hat{\mu},x'})(\gamma_\mu)_{dd'} \tag{1.38}$$

However, this ansatz leads to 16 degenerate particles, 15 more than we want to describe. To see this, we have to consider the particle spectrum of the free theory. Each pole in the propagator, i.e., the inverse of the Dirac operator, corresponds to a particle. It is convenient to go to momentum space. There the action reads

$$S = \frac{1}{V}\sum_k \bar{\psi}(k)(D(k) + m)\psi(k) \tag{1.39}$$

The sum in Eq. (1.39) is over all momenta $k_\mu$ in the Brillouin zone

$$k_\mu = 2\pi\frac{n_\mu}{L} \qquad \text{with} \quad n_\mu = 0, \ldots, L-1 \tag{1.40}$$

In particular, for the naïve action Eq. (1.36) we get

$$D = i\gamma_\mu \sin k_\mu \tag{1.41}$$

The propagator $S_F$ is the inverse of the Dirac operator which turns out to be

$$S_F = (D+m)^{-1} = \frac{-i\sin(ak_\mu)\gamma_\mu + m}{\sum_\mu \sin^2(ak_\mu) + m^2} \tag{1.42}$$

The poles of this function give the particles of the free theory. So, we have to determine the zeros of the denominator in Eq. (1.42). The sine function has zeros

at $ak_\mu = 0$ and at $ak_\mu = \pi$. As $\mu = 1, \ldots, 4$ there are 16 particles. These are called doublers. With $E = -ik_4$ all these particles have the correct dispersion relation in the continuum limit $a \to 0$

$$E = \sqrt{m^2 + \mathbf{k}^2} \ . \tag{1.43}$$

The doublers are intrinsically related to chiral symmetry. This is stated by the Nielsen-Ninomiya theorem [NN81a, NN81b], according to which the following four conditions cannot hold simultaneously for the Dirac operator

- **locality**
  $D(r) = D(x, x+r)$ vanishes fast enough for $|r| \to \infty$, i.e., it is bounded by $Ce^{-\gamma|r|}$
- **continuum limit**
  The Fourier transform $\hat{D}(k)$ is for small momenta $\hat{D}(k) = i\gamma_\mu k_\mu + \mathcal{O}(a^2k^2)$ with $k \ll \pi/a$
- **no doublers**
  $\hat{D}(k)$ is invertible for $k \neq 0$ which implies no massless doublers.
- **naïve chiral symmetry**
  $D\gamma_5 + \gamma_5 D = 0$

For a long time, it has been generally believed that this makes it impossible to formulate QCD with chiral symmetry on the lattice. The first cure with the Wilson fermions was to break explicitly chiral symmetry in a way that it can be restored in the continuum limit. The current solution comes under the name of Ginsparg-Wilson fermions. These use the fact that the fourth condition is not the correct lattice version of chiral symmetry. This is discussed in Section 1.6.4.

### 1.6.2 Wilson fermions

The idea of Wilson fermions [Wil77] is to give the doublers a mass which grows in the continuum limit, e.g., $m \propto 1/a$. This is done by adding a term to the naïve action Eq. (1.36)

$$S_{\text{Wilson}} = a^4 \sum_x \left[ (m + \frac{4r}{a})\bar{\psi}(x)\psi(x) - \frac{1}{2a}\sum_\mu \bar{\psi}(x+\hat{\mu})[r+\gamma_\mu]\psi(x) \right] \quad . \tag{1.44}$$

The parameter $r$ can take any value $0 < r \leq 1$. For $r = 0$ the naïve action Eq. (1.36) is recovered. In practical simulation one frequently — as we did — takes $r = 1$. If we now change the normalization of the fermion fields

$$\sqrt{a^3(am+4r)}\psi \to \psi \quad \text{and} \quad \sqrt{a^3(am+4r)}\bar{\psi} \to \bar{\psi} \tag{1.45}$$

we can bring this action into the standard form

$$S_{\text{Wilson}} = \sum_x \left[ \bar{\psi}(x)\psi(x) - \kappa \sum_\mu \bar{\psi}(x+\hat{\mu})[r+\gamma_\mu]\psi(x) \right] \quad . \tag{1.46}$$

Here we introduced the *hopping parameter* $\kappa$ which now encodes the bare mass of the fermion

$$\kappa = \frac{1}{2am + 8r} \tag{1.47}$$

In the free theory the chiral limit $am_q \to 0$ is performed by

$$\frac{1}{\kappa} \to 8r \equiv \frac{1}{\kappa_{\text{c}}^{\text{free}}} \tag{1.48}$$

In a realistic simulation with interacting fermions it has to be determined experimentally which quark mass a given value of $\kappa$ corresponds to. The value of $\kappa$ which gives a zero quark mass is called the *critical hopping parameter* $\kappa_{\text{c}}$. It is not possible to determine it unambiguously. The standard procedure is to look at observables which vanish in the chiral limit as the pion mass or the PCAC quark mass.[1]

In one of our simulations we use Wilson quarks together with the Wilson gauge action at a gauge coupling of $\beta = 6/g_0^2 = 6.0$. Then a perturbative relation between $\kappa$ and the quark mass gives [G+96b]

$$am_q = 0.56(\frac{1}{\kappa} - \frac{1}{\kappa_{\text{c}}}) \ . \tag{1.49}$$

For this $\beta$ the critical hopping parameter was determined by using the PCAC quark mass to $\kappa_{\text{c}} = 6.3642$.

### 1.6.3 Clover Fermions

In Section 1.4.2 we have discussed a method to improve the continuum limit $a \to 0$ of observables. The gauge action can be modified such that the $\mathcal{O}(a^2)$ effects are removed. An analogous procedure for the fermion part of the action comes under the name of *clover improvement*. Here a term proposed by Sheikholeslami and Wohlert [SW85] is added to the fermionic Wilson action

$$S_W \longrightarrow S_W + c_{\text{sw}} \frac{i}{4} a\bar{\psi}(x)\sigma_{\mu\nu}F_{\mu\nu}(x)\psi(x). \tag{1.50}$$

$\sigma_{\mu\nu}$ is defined in Eq. (A.6) and $F_{\mu\nu}$ is a discretization of the field strength tensor. A common discretization of $F_{\mu\nu}$ has the form of a clover leaf and is responsible

[1] The PCAC (partial conservation of the axial-vector current) quark mass is also called axial-vector Ward identity (AWI) mass and defined in Eq. (3.36).

for the name of this term. It includes the plaquettes from the Wilson action that attach to the point $x$ in the $\mu$-$\nu$–plane. The coefficient $c_{\rm sw}$ of the clover term has been determined non-perturbatively for a set of lattice spacings in [LSS+97, EHK98]. We use for the Wilson gauge action with $\beta = 6.0$ the clover parameter of $c_{SW} = 1.769$.

### 1.6.4 Ginsparg-Wilson fermions

A more elaborate approach is used by so-called Ginsparg-Wilson fermions. The continuum definition of chirality is not implemented naïvely on the lattice but modified by a term which vanishes for $a \to 0$. But this violation is necessary to get the correct chiral anomaly. The starting point for this is the Ginsparg-Wilson relation originally given in [GW82] and reconsidered in [HLN98, Has98b]

$$\gamma_5 D + D\gamma_5 = 2aD\gamma_5 RD \tag{1.51}$$

with $D$ the Dirac operator and $R$ some local function of the gauge field. This is frequently set to a constant and in our applications we take $R = 1/2$ and thus get the simplified form

$$\gamma_5 D + D\gamma_5 = aD\gamma_5 D \ . \tag{1.52}$$

Obviously the breaking of chiral symmetry by the term on the right hand side of Eq. (1.51) vanishes in the continuum limit. Eq. (1.52) corresponds to a modification of the chiral symmetry transformation Eq. (1.29). The lattice version can, e.g., be chosen to be [Lüs98]

$$\psi \longrightarrow e^{i\omega\gamma_5(1-\frac{1}{2}aD)}\psi \qquad\qquad \bar{\psi} \longrightarrow \bar{\psi}e^{i\omega(1-\frac{1}{2}aD)\gamma_5} \tag{1.53}$$

There are several operators available, which fulfill the Ginsparg-Wilson relation either exactly or approximately. The most popular exact solution is the overlap operator $D_{\rm ov}$ [NN93b, NN93a, NN95]. Its construction starts from a lattice Dirac operator $D_0$ which fulfills all requirements except chiral symmetry, e.g., the Wilson Dirac operator. Using $H = \gamma_5(D_0 - \mu)$ with some constant $\mu$ the overlap Dirac operator is given by

$$D_{\rm ov} = \mu(1 + \gamma_5 \frac{H}{\sqrt{H^+H}}) \tag{1.54}$$

The computation of the inverse square root of $H^+H$ is very expensive with respect to computer time.

The domain wall fermion approach [Kap92, Sha93, FS95] extends the Wilson fermions into an auxiliary fifth dimension with length $L_5$ and two kinks in the mass term where the sign changes. On the two $4d$ slices where the mass changes sign, fermions with definite chirality are obtained.

Furthermore, there exist several approximate solutions to the Ginsparg-Wilson equation. These are ultra-local, i.e., the support of the Dirac operator is finite. The parameterized Fixed Point action [H$^+$01, Has98a, Has98b, HLN98] is based on blocking transformations from the continuum. In principle, it can be made exact by including infinitely many terms but in practical applications it has been restricted to the hypercube. The chirally improved operator [Gat01, GH00, GHL01] is an approximate solution to the Ginsparg-Wilson equation, too. Its construction is described in Sec 1.6.5. The approximate solutions can be a good compromise between chiral properties and the speed of numerical simulations.

Now we prove two properties of the spectrum of a Dirac operator satisfying the Ginsparg-Wilson Eq. (1.52) which will be useful in the course of this work.

1) The spectrum is confined to a circle around $(1/a, 0)$ with radius $1/a$.

   For an eigenvector $|\psi\rangle$ of $D$ with eigenvalue $\lambda$

$$(\lambda + \lambda^*)\gamma_5|\psi\rangle = (\gamma_5 D + D\gamma_5)|\psi\rangle = aD\gamma_5 D|\psi\rangle = a\lambda^*\lambda\gamma_5|\psi\rangle \tag{1.55}$$

   Here we have used the $\gamma_5$-hermiticity of $D$. From Eq. (1.55) follows

$$\frac{2}{a}\mathrm{Re}\,\lambda = |\lambda|^2 \tag{1.56}$$

   If we define $\lambda = x + iy$ for real $x$, $y$ we get the equation describing a circle, see Fig. 1.6.

$$\frac{2x}{a} = x^2 + y^2 \Rightarrow (x - \frac{1}{a})^2 + y^2 = a^{-2} \tag{1.57}$$

   In the continuum limit the circle gets larger. The imaginary axis in the vicinity of the origin and thus the physical spectrum is approached. The unphysical region of the doublers which is around $(2/a, 0)$ moves in this limit farther away and decouples from physical quantities.

2) $\langle\psi_i|\gamma_5|\psi_i\rangle = 0$ unless $\lambda$ is real.

   For an eigenvector $\psi_i$ of the Dirac operator, $D\psi_i = \lambda\psi_i$ we use the $\gamma_5$ hermiticity to get

$$\lambda\langle\psi|\gamma_5|\psi\rangle = \langle\psi|\gamma_5 D|\psi\rangle = \langle\psi|D^+\gamma_5|\psi\rangle = \lambda^*\langle\psi|\gamma_5|\psi\rangle \tag{1.58}$$

   Thus $\psi^+\gamma_5\psi = 0$ if $\mathrm{Im}\lambda \neq 0$.

A Ginsparg-Wilson Dirac operator $D$ describes a massless quark. To get the massive Dirac operator one has to add a mass and simultaneously rescale the circle [Nie99]

$$D_m = (1 - \frac{1}{2}am)D + m\ . \tag{1.59}$$

This keeps the second intersection of the circle with the real axis at 2.

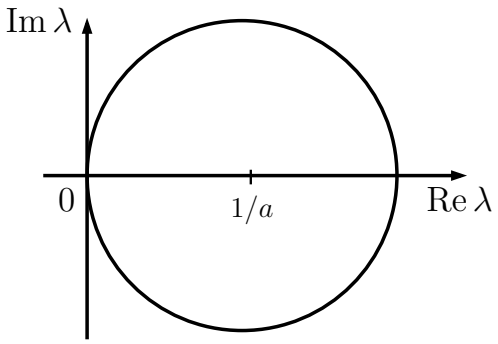


Figure 1.6: The spectrum of a Dirac operator satisfying the Ginsparg-Wilson equation Eq. (1.52) with $R = 1/2$ lies on a circle around $(1/a, 0)$ with radius $1/a$. As $a \to 0$ the spectrum approaches the continuum spectrum on the imaginary axis.

### 1.6.5 The chirally improved Dirac operator

The known exact solutions of the Ginsparg-Wilson equation are expensive to compute, and therefore the range of applicability is limited. An approximate solution can be a good compromise. Gattringer, Hip, and Lang [Gat01, GH00, GHL01] have developed such an approximate solution to the Ginsparg-Wilson equation which shall be called chirally improved Dirac operator subsequently.

The first step in the construction is to write down the most general Dirac operator on the lattice. This is done by allowing more general lattice discretizations of the derivative. The standard derivative term makes use of nearest neighbors only but certainly one can include also more remote points on the lattice such as next-to-nearest neighbors or diagonal terms etc. Each such term is characterized by the product of link variables which form the gauge transporter connecting the two points used in the derivative. The corresponding set of links can be viewed as a path on the lattice. The most general derivative on the lattice will then include all possible paths, each of them with some complex coefficient. In order to remove the doublers, in addition to the derivative terms coming with the Dirac matrices $\gamma_\mu$, we also have to include terms proportional to the unit matrix in Dirac space. To obtain the most general expression, we include all 16 elements $\Gamma_\alpha$ of the Clifford algebra, i.e. we also add tensor, pseudo-vector and pseudoscalar terms, see Appendix B. To summarize, the most general Dirac operator is a sum over all $\Gamma_\alpha$, each of them multiplied with all possible paths on the lattice and each path comes with its own coefficient.

The next step is to apply the symmetry transformations: translations, rotations, charge conjugation, parity, and $\gamma_5$-hermiticity defined in Eq. (1.34). Once these symmetries are implemented the coefficients of the paths in the Dirac operator are restricted. One finds that groups of paths which are related by symmetry

transformations have to come with the same coefficient, up to possible signs. The most general Dirac operator which obeys the symmetries can be written as:

$$
\begin{aligned}
D \equiv \mathbb{1}\Big[ & s_1 <> \; + s_2 \sum_{l_1} < l_1 > \; + s_3 \sum_{l_2 \neq l_1} < l_1, l_2 > \; + s_4 \sum_{l_1} < l_1, l_1 > \; ... \Big] \\
& + \sum_{\mu} \gamma_\mu \sum_{l_1 = \pm\mu} s(l_1) \Big[ \; v_1 < l_1 > \; + v_2 \sum_{l_2 \neq \pm\mu} [< l_1, l_2 > + < l_2, l_1 >] \\
& \qquad\qquad + \; v_3 < l_1, l_1 > \; ... \; \Big] \\
& + \sum_{\mu<\nu} \gamma_\mu \gamma_\nu \sum_{\substack{l_1 = \pm\mu \\ l_2 = \pm\nu}} s(l_1) \; s(l_2) \sum_{i,j=1}^{2} \epsilon_{ij} \Big[ \; t_1 < l_i, l_j > \; ... \; \Big] \\
& + \sum_{\mu<\nu<\rho} \gamma_\mu \gamma_\nu \gamma_\rho \sum_{\substack{l_1 = \pm\mu, l_2 = \pm\nu \\ l_3 = \pm\rho}} s(l_1) \; s(l_2) \; s(l_3) \sum_{i,j,k=1}^{3} \epsilon_{ijk} \Big[ \; a_1 < l_i, l_j, l_k > \; ... \; \Big] \\
& + \gamma_5 \sum_{\substack{l_1 = \pm 1, l_2 = \pm 2 \\ l_3 = \pm 3, l_4 = \pm 4}} s(l_1) \; s(l_2) \; s(l_3) \; s(l_4) \sum_{i,j,k,n=1}^{4} \epsilon_{ijkn} \Big[ \; p_1 < l_i, l_j, l_k, l_n > \; ... \; \Big] \; .
\end{aligned}
\tag{1.60}
$$

By $\epsilon$ we denote the totally anti-symmetric tensors with 2, 3, and 4 indices. We use the notation $< l_1, l_2 \, ... \, l_n >$ to denote a path of length $n$ and the $l_i \in \{-4, -3, -2, -1, 1, 2, 3, 4\}$ simply denote the directions of the subsequent links which build up the path. $s(l_i)$ is an abbreviation for $sign(l_i)$. With the particular choice for the generators of the Clifford algebra used in Eq. (1.60) (no additional factors of $i$), the coefficients $s_i, v_i, t_i, a_i, p_i$ are real. The expansion parameter for the Dirac operator in Eq. (1.60) is the length of the path since the coefficients in front of the paths decrease in size as the length of the corresponding path increases. A general argument for this behavior can be given and it has been confirmed numerically for the solution presented in [GHL01]. We remark that an equivalent form of $D$ presented in [H$^+$01] is the basis for a parameterization of the perfect Dirac operator.

The final step in the construction is to insert the general expression for $D$ into the Ginsparg-Wilson equation. On the left hand side of the Ginsparg-Wilson equation (1.51) some of the terms acquire minus signs, depending on the commutator of the corresponding $\Gamma_\alpha$ with $\gamma_5$. On the right hand side an actual multiplication of all the terms in $D$ has to be performed. However, using the above notion of a path, the multiplication on the right hand side can be formulated in an algebraic way and then can be evaluated using computer algebra. Once all multiplications are performed one can compare the left and right hand sides of the Ginsparg-Wilson equation. It is important to note that for an arbitrary gauge field different paths, which correspond to different gauge transporters, are linearly independent and can be viewed as elements of a basis. Thus for the two

sides of Eq. (1.51) to be equal, the coefficients in front of the same basis elements on the two sides have to agree. When comparing the terms on the two sides, the result is a set of coupled quadratic equations for the expansion coefficients $s_i, v_i, t_i, a_i, p_i$. This set of equations is equivalent to the Ginsparg-Wilson equation. After a suitable truncation of Eq. (1.60) to finitely many terms the system can be solved and the result is an approximation to a solution of Eq. (1.51). In addition it is possible to include a dependence on the inverse gauge coupling $\beta_1$ through an additional constraint for the coefficients. This step allows to work with less terms in the parameterization. This procedure is similar to the tuning of the mass-like shift which is used to optimize the localization of the overlap operator [HJL99]. An explicit list of the terms used in our parameterization of the Dirac operator and the values of the coefficients $s_i, v_i, t_i, a_i, p_i$ are given in Appendix B. After the truncation we are left with a Dirac operator which has entries on all points of the hypercube with an additional L-shaped term.

After a test of the 2-d chirally improved Dirac operator in the Schwinger model with dynamical quarks in [GH00] the construction was outlined for four dimensions in [Gat01]. A test of a Dirac operator based on this approximation was presented in [GHL01] and it was found that the approximation is particularly good in the physical part of the spectrum. Near the origin the deviation of the eigenvalues from the Ginsparg-Wilson circle is very small. As we are going to study the low lying modes of the Dirac operators in Chapter 2 we are interested in the spectrum near the origin. This makes the chirally improved Dirac operator very well suited for the physical questions analyzed here. Furthermore we will see in Chapter 3 that it reproduces the hadronic spectrum well.

## 1.7 The path integral on the lattice

After having defined the Lagrangian of the theory, we should now define the path integral in order to be able to compute matrix elements. The path integral in the continuum is given by a limiting process of the path integral defined on the lattice. We give a brief overview over the notation, a more detailed discussion can be found in a textbook [MM94] and the references therein.

The expectation value of some function $F(\bar{\psi}, \psi, U)$ depending on the quark and gauge fields is given by the following formal expression

$$\langle F \rangle = \frac{1}{Z} \int \prod_{x,\mu} \mathrm{d}U_\mu(x) \prod_{x,d,c} \mathrm{d}\bar{\psi}(x,d,c) \mathrm{d}\psi(x,d,c) F(\bar{\psi}, \psi, U) e^{-S_f[\bar{\psi},\psi,U] - S_g[U]} \tag{1.61}$$

where the product over $x, c, d$ runs over all sites of the lattice, the color and the Dirac indices. $Z$ is the partition function of the theory which is given by

$$Z = \int \prod_{x,\mu} \mathrm{d}U_\mu(x) \prod_{x,d,c} \mathrm{d}\bar{\psi}(x,d,c) \mathrm{d}\psi(x,d,c) e^{-S_f[\bar{\psi},\psi,U] - S_g[U]} \ . \tag{1.62}$$

with $\mathrm{d}U$ the Haar measure of the gauge group. The fermionic action is a bilinear form with the Grassmann valued variables $\bar{\psi}$ and $\psi$

$$S_f[\bar{\psi},\psi,U] = \sum_{\substack{x,d,c\\x',d',c'}} \bar{\psi}(x,d,c)D_m(x,d,c;x',d',c')\psi(x',d',c') \ , \tag{1.63}$$

with $D_m$ being the massive Dirac operator of the theory Eq. (1.59) which depends on the gauge fields. It is a standard result that one can integrate out the fermionic fields analytically. For the partition function one ends up with

$$Z = \int \prod_{x,\mu} \mathrm{d}U_\mu(x) \det D_m e^{-S_g[U]} \tag{1.64}$$

For a purely gluonic operator the expectation value is analogously given by

$$\langle \mathcal{O} \rangle = \frac{1}{Z} \int \prod_{x,\mu} \mathrm{d}U_\mu(x) \det D_m \mathcal{O}[U] e^{-S_g[U]} \ . \tag{1.65}$$

Obviously, operators containing fermionic fields have to be treated differently. For an operator which contains $n$ $\psi$-fields and the same number of $\bar{\psi}$-fields we have to use Wick's theorem to substitute these by propagators, i.e., the inverse of the Dirac operator. This can easily be computed using the *generating functional* of the theory. It is given by

$$\begin{aligned} W[J,\bar{J},U] = \frac{1}{Z} \int [\mathrm{d}U][\mathrm{d}\bar{\psi}][\mathrm{d}\psi] e^{-S_g[U]} \times \\ e^{\int \mathrm{d}^4x \mathrm{d}^4y \bar{\psi}(x) D_m(x;y) \psi(y)} e^{\int \mathrm{d}^4x \bar{\psi}(x) J(x)} e^{\int \mathrm{d}^4x \bar{J}(x) \psi(x)} \ . \end{aligned} \tag{1.66}$$

Here we have abbreviated the measure in the path integral by $[\cdots]$. The currents $J$ carry color and Dirac indices, the sums over which are implicit. From this expression, the expectation values of fermionic operators can be calculated performing functional derivatives with respect to $J$ and $\bar{J}$. After taking the derivative, the currents $J$ and $\bar{J}$ are set to zero and one gets

$$\langle \prod_{i=1}^{n} \{ \bar{\psi}_{a_i} \psi_{b_i} \} \rangle = \prod_{i=1}^{n} \left\{ \frac{\delta}{\delta J_{a_i}} \frac{\delta}{\delta \bar{J}_{b_i}} \right\} W[J,\bar{J}] \Big|_{\substack{J=0\\ \bar{J}=0}} \ . \tag{1.67}$$

In this formula multi-indices $a_i$ and $b_i$ combining the Dirac, color, and flavor index are used to simplify the notation. The functional derivatives with respect to $J$ and $\bar{J}$ anticommute which reflects the Grassmann nature of the fermionic fields. To bring the generating functional Eq. (1.66) in a useful form we complete

the square and get

$$
\begin{aligned}
&W[J,\bar{J},U] \\
&\quad = \frac{1}{Z}\int [\mathrm{d}U][\mathrm{d}\bar{\psi}][\mathrm{d}\psi] e^{-S_g[U]} \exp\left\{\int \mathrm{d}^4x \int \mathrm{d}^4y \bar{J}(x) D_m^{-1}(x,y) J(y)\right\} \times \\
&\qquad \exp\left\{-\int \mathrm{d}^4x \mathrm{d}^4y \left[\bar{\psi}(x) - \int \mathrm{d}^4x' \bar{J}(x') D_m^{-1}(x',x)\right] D_m(x,y) \times \right. \\
&\qquad\qquad \left. \left[\psi(y) - \int \mathrm{d}^4y' D_m^{-1}(y,y') J(y')\right]\right\} \qquad (1.68)
\end{aligned}
$$

Now one shifts the $\bar{\psi}$ and the $\psi$ integration by

$$
\begin{aligned}
\psi(y) - \int \mathrm{d}^4y' D_m^{-1}(y,y') J(y') &\longrightarrow \psi(y) \\
\bar{\psi}(x) - \int \mathrm{d}^4x' \bar{J}(x') D_m^{-1}(x',x) &\longrightarrow \bar{\psi}(x)
\end{aligned} \qquad (1.69)
$$

which leaves the measure unchanged. After integrating out the fermionic variables, one ends up with

$$
\begin{aligned}
W[J,\bar{J},U] = \frac{1}{Z}\int [\mathrm{d}U] \det D_m \, e^{-S_g[U]} \times \\
\exp\left(\int \mathrm{d}^4x \mathrm{d}^4y \bar{J}^c_\alpha(x) D_m^{-1}(x,\alpha,c;y,\alpha',c') J^{c'}_{\alpha'}(y)\right) \qquad (1.70)
\end{aligned}
$$

where we have again included the color and Dirac indices.

With this expression, we can transform the fermionic fields in the path integral (Eq. (1.67)) into a product of propagators, which depend on the gauge field only. There are no more fermion fields to integrate over. An example of the computation of such a $n$-point function is given in Sec. 3.1

## 1.8 Monte Carlo

It remains to compute the high dimensional integral over the gauge variables. In computer simulation of lattice QCD this is done by a Monte Carlo technique. We substitute the integral

$$
\langle f \rangle = \frac{1}{Z}\int \prod_{x,\mu} \mathrm{d}U_\mu(x) \det D_m \; f[U] e^{-S_g[U]} \qquad (1.71)
$$

by an average over gauge configurations. A gauge configuration $U_i$ gives the value of $U$ on each link. The gauge configurations are distributed according to the weight $[\det D_m \; \exp(-S_g[U])]$. A considerable simplification of the numerical

calculation is obtained by using the so-called *quenched approximation*, which is discussed below in Sec. 1.8.1. It consists of setting $\det D_m$ to a constant. It is immediately clear that the gauge fields — now distributed as $\exp(-S_g[U])$ — can be chosen without the knowledge of the Dirac operator.

A lattice calculation starts by generating an ensemble of $N$ gauge configurations $U_i$, $i = 1, \ldots, N$. The estimate of the path integral is then given by

$$\langle f \rangle_N = \frac{1}{N} \sum_{i=1}^{N} f[U_i] \ . \tag{1.72}$$

In the limit $N \to \infty$ this approaches the true average

$$\langle f \rangle_N \stackrel{N\to\infty}{\longrightarrow} \langle f \rangle \ . \tag{1.73}$$

For the discussion of the error analysis see Appendix C. There exist several algorithms to generate a sequence of gauge configurations with a probability distribution

$$P[U] = C \exp(-S_g[U]). \tag{1.74}$$

The normalization factor $C$ is chosen such that $\sum_U P[U] = 1$.

All these algorithms produce a Markov chain of subsequent configurations $U_i$ by an updating process. Here the key quantity is the transition probability $w(U' \leftarrow U)$ to get from a configuration $U$ to a configuration $U'$. The transition probability $w$ has to fulfill strong *ergodicity*

$$w(U' \leftarrow U) > 0 \quad \text{for all} \quad U,\ U' \tag{1.75}$$

which states that any configuration can be reached from any other configuration. Thus the Markov chain exhausts the whole configuration space. Furthermore, the transition probability has to be normalized

$$\sum_{U'} w(U' \leftarrow U) = 1 \ . \tag{1.76}$$

The key condition of an algorithm is the *detailed balance* which is a sufficient condition to generate the distribution Eq. (1.74)

$$w(U' \leftarrow U) P[U] = w(U \leftarrow U') P[U'] \ . \tag{1.77}$$

In this way a sequence of gauge configurations starting from a configuration $U_1$ is generated.

$$U_1 \to U_2 \to \cdots \to U_N \tag{1.78}$$

An arbitrarily chosen configuration $U_1$ has a very low weight. However, the algorithm is designed such that the configurations move to the region of higher importance. Therefore it is advisable to discard the first configurations.

An algorithm which has proven suitable to generate a sequence of gauge configurations is the Metropolis algorithm [MRR$^+$53]. A Metropolis step on one link consists of substituting this link variable by a new one. This is called an offer. This offer is accepted immediately if the new configuration has a higher Boltzmann weight $\exp(-S_g[U])$. If the Boltzmann factor is smaller, the new configuration is accepted with a probability equal to the ratio of Boltzmann factors of the new configuration to that of the old one. One Metropolis sweep consists of this step for all links of the lattice.

One sweep alone is not enough to generate an independent configuration. Therefore one has to iterate this sweep several times ($\mathcal{O}(1000)$) to remove the correlation between the two. In our simulations, we use a mixture of the Metropolis steps and over-relaxation steps [Cre87] to improve the decorrelation of the subsequent configurations.

### 1.8.1 The quenched approximation

Monte Carlo simulations are simplified drastically, if the fermion determinant $\det D_m$ is set to a constant. In expectation values this constant cancels as the same constant occurs in the normalization factor $Z$. To understand the implication of this approximation it is useful to note that the determinant is real. Using $D = \gamma_5 D^+ \gamma_5$ we get

$$\det D_m = \det(\gamma_5 D_m \gamma_5) = \det D_m^+ = (\det D_m)^* \tag{1.79}$$

As the QCD Lagrangian is diagonal in the quark flavor, each flavor adds an additional factor of $\det D_m$. So for mass degenerate quarks the contribution of this determinant is $(\det D)^{N_f}$ with $N_f$ the number of flavors.

If $N_f$ is odd, the determinant can fluctuate in sign. It cannot be included in the weight of the Monte-Carlo as this is to be interpreted as a probability distribution. This is the major obstacle of simulations with odd $N_f$.

At the moment dynamical computations are performed with an even number of degenerate quark flavors. Then the determinant can be included in the weight. If the series of gauge configurations has been generated including the determinant, the evaluation of the observables is exactly the same as in the quenched case. Quenching merely amounts to changing the weights with which configurations contribute. However, the numerical effort to generate these 'unquenched' configurations is several orders of magnitudes larger than in the quenched case. This has several reasons.

- The computation of the determinant of such a large matrix is nontrivial.
- The updating step of the Metropolis algorithm is local in the quenched approximation. We have to compare the weight of the old and the new

configuration. As the gauge action is a sum of local terms the weight is a product of local terms

$$e^{-\sum_p S_p[U]} = \prod_p e^{-S_p[U]} \ . \tag{1.80}$$

If we now offer a new link variable $U_\mu(x)$ only very few of the factors change and the new weight can be computed very quickly. For the fermion determinant this is not possible since it connects the link variables in a non-local way.

In physical terms, the quenched approximation amounts to the limit of infinite masses for the sea quarks; no virtual quark–anti-quark pairs can be generated. This is plausible, as the determinant of $D_m$ is dominated by the diagonal elements if $m \to \infty$. However, in many simulations this approximation has given good results. Furthermore, the sea quark masses of current simulations are quite large, e.g. of the order of 50 MeV and their contribution is, thus, quite small. However their effect will certainly get larger with smaller quark masses. In general the error introduced by the quenched approximation is estimated to be of the order of $10\% \ldots 20\%$.

# Chapter 2

# Chiral symmetry breaking

As discussed in the introduction, chiral symmetry breaking is a key feature of the theory of strong interactions. Whereas in early theories it had to be introduced by hand, it emerges quite naturally in QCD. Even though the Lagrangian is chirally invariant, the full interacting theory is not. This allows the creation of a chiral condensate $\langle\bar{\psi}\psi\rangle$, which should vanish in a chirally invariant theory. Via the Banks-Casher relation the emergence of the chiral condensate is linked to the density of eigenvalues $\rho(\lambda)$ of the Dirac operator at $\lambda = 0$. A promising explanation of its creation is given by the interaction of instantons, i.e., classical solutions of the equations of motion for the gauge fields. This is the subject of Sec. 2.1. It is interesting to search for traces of instantons in the corresponding, low lying eigenmodes of the Dirac operator. In particular, we consider two of the major properties of instantons. The first is that they are localized objects, the second is their definite chirality. In the course of Section 2.2 we first examine observables which quantify the localization of the eigenmodes. Later on we look into observables which connect localization and chirality.

In the second part of this chapter, Sec.2.3, the behavior of these observables is analyzed for increasing temperature $T$. It is generally believed that for growing $T$ a phase transition occurs in QCD from the chirally broken phase to a phase where chiral symmetry is restored. Lattice studies further indicate that this coincides with the deconfinement phase transition. The purpose of large experimental programs at RHIC and LHC is to collect information about these phase transitions. Our aim is to study localization and chirality in the two phases. This can be used to sharpen the ideas from models based on the classical solutions called *calorons* in the finite temperature region. Finally, a summary of the findings of this section is given in Sec. 2.4.

## 2.1 The mechanism of chiral symmetry breaking

We are going to study chiral symmetry breaking by looking at the eigenvectors and eigenvalues of the Dirac operator, especially for eigenvalues close to the origin. There we define the density of eigenvalues $\rho(\lambda)$ such that $\rho(\lambda)\Delta\lambda$ gives the number of eigenvalues in the interval $(\lambda, \lambda+\Delta\lambda]$. The zero modes themselves do not contribute to this density. Spontaneous breaking of chiral symmetry is manifest in the emergence of a non-zero chiral condensate $\langle\bar{\psi}\psi\rangle$. The *Banks-Casher* relation [BC80] states that the density of eigenvalues *near* the origin $\lambda = 0$ is proportional to the chiral condensate.

$$\langle\bar{\psi}\psi\rangle = -\frac{\pi}{V}\rho(0) \tag{2.1}$$

Here $V$ is the volume of the finite box in which the theory is put. This truncation is necessary to define a finite density of eigenvalues. But $\rho(0)/V$ should become constant as $V \to \infty$.

### 2.1.1 Instantons

In order to understand the emergence of a finite chiral condensate some facts about instantons are collected in this section. For more detail see, e.g., [SS98]. An instanton is a solution of the equations of motion for pure Yang-Mills theory [tH76]

$$D_\mu F_{\mu\nu} = 0 \tag{2.2}$$

with the covariant derivative $D_\mu = \partial_\mu + A_\mu$. The dual field strength tensor $\tilde{F}_{\mu\nu}$ is defined by

$$\tilde{F}_{\mu\nu} = \frac{1}{2}\epsilon_{\mu\nu\alpha\beta}F_{\alpha\beta} \tag{2.3}$$

with $\epsilon$ the totally anti-symmetric tensor of rank four. The solutions of Eq. (2.2) are either selfdual, i.e. $F_{\mu\nu} = \tilde{F}_{\mu\nu}$, or anti-selfdual $F_{\mu\nu} = -\tilde{F}_{\mu\nu}$. The selfdual solutions are called instantons, the anti-selfdual solutions anti-instantons. The specific solutions can be given in a specific gauge [BPST75, tH76] using the 't Hooft symbol:

$$\eta_{a\mu\nu} = \begin{cases} \epsilon_{a\mu\nu} & \mu,\nu = 1,2,3 \\ \delta_{a\mu} & \nu = 4 \\ -\delta_{a\nu} & \mu = 4 \end{cases} \tag{2.4}$$

Then one can write the gauge potential $A^a_\mu(x)$ of the instanton with center at $x_\mu = 0$ as

$$A^a_\mu(x) = \frac{2\eta_{a\mu\nu}x_\nu}{x^2+\rho^2} \tag{2.5}$$

with $\rho$ the radius of the instanton. The square of the field strength of this object takes the following form

$$(F^a_{\mu\nu}(x))^2 = \frac{192\rho^4}{(x^2+\rho^2)^4} \ . \tag{2.6}$$

From this expression we see that an instanton is a well localized object. The size is determined by the parameter $\rho$.

The interesting physics comes via the influence of the instantons on fermions. For a single (anti)-instanton gauge field, the Dirac operator has a zero mode

$$D\psi = 0 \ . \tag{2.7}$$

Chiral invariance of the QCD-Lagrangian means that the Dirac operator anti-commutes with $\gamma_5$

$$D\gamma_5 + \gamma_5 D = 0 \ , \tag{2.8}$$

which implies that $D$ and $\gamma_5$ have simultaneous eigenvectors. As $\gamma_5^2 = 1$ the eigenvalues of $\gamma_5$ can be $\pm 1$. The instantons have $\gamma_5$-eigenvalue $-1$, the anti-instantons $+1$. This is sometimes expressed by calling the (anti)-instantons right (left) handed. It is useful to define projectors $P_\pm$ on the left and right handed components

$$P_\pm = \frac{1}{2}(1 \pm \gamma_5) \ . \tag{2.9}$$

The instanton picture of chiral symmetry breaking explains the formation of a non-zero density of *near-zero* eigenvalues by the interaction of instantons and anti-instantons. The rough picture is as follows.

A gauge field that consists of an instanton and an anti-instanton, which are well separated compared to their radii, creates two zero modes in the Dirac operator. If the distance is reduced slowly, the instanton and the anti-instanton start to overlap. The corresponding eigenvalues acquire a small imaginary part. (In Figure 2.1 this process is depicted for a Ginsparg-Wilson operator.) As the imaginary part gets larger, the overlap becomes stronger. For whole ensembles of interacting instantons and anti-instantons, a density of eigenvalues near the origin is created. Via the Banks-Casher formula this amounts to the creation of a chiral condensate. However, the (anti)-instantons getting closer, they will eventually lose their identity, i.e., the interaction destroys their property of being classical solutions. Thus, it is a priori not clear whether the concept of interacting instantons is useful. This is going to be clarified by our simulations.

## 2.2 A lattice study of chiral symmetry breaking

According to the instanton model the near-zero modes of the Dirac operator should be dominated by instantons. This implies that they should contain localized, chiral structures. In order to verify these two predictions, we compute the

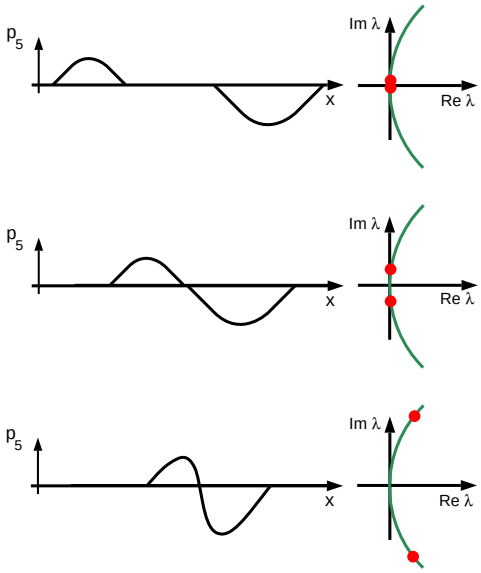


Figure 2.1: The creation of near-zero modes by the interaction of instantons. The circles on the right represent the spectrum of the Ginsparg-Wilson Dirac operator. On the left the chiral density $p_5$ of Eq. (2.11) is sketched which gives a picture of the excitation; a positive bump is associated with an anti-instanton, a negative with an instanton.

eigenvalues and eigenvectors of the Dirac operator closest to the origin on several ensembles of gauge configurations of different lattice spacings and sizes.

The difficulties that arise in studying instanton effects on the lattice come from two sources. First, we generally do not deal with single instantons. Strictly speaking multi-(anti)-instanton configurations are not well defined. Nevertheless, models based on these are successful. As long as the instantons are well separated, we can assume that the multi-instanton solution is just a superposition of single instantons. Because we do not want to use any pattern matching procedures, we look at observables which are well defined on any configuration. The findings are then to be compared to the predictions from instanton models.

The second problem comes from the existence of quantum fluctuations. The instanton being a classically defined object is by definition smooth. But a configuration in a realistic Monte-Carlo simulation is quite rough. In the past so-called cooling techniques have been employed to smooth the gauge fields. These all suffer from the fact that no unique definition for a cooling procedure can be given. Especially a stopping criterion for the iteration is missing. In many of these procedures, eventually, all instanton–anti-instanton pairs have annihilated. As we use the Dirac operator as a filter for the gauge fields, we are only sensitive to the part of the fluctuations that affect the fermions. These are in general less severe than the actual gauge field fluctuations. We study the dependence on the fluctuations by considering different values of the gauge coupling.

| | $\beta_1 = 8.10$ | $\beta_1 = 8.30$ | $\beta_1 = 8.45$ |
|---|---|---|---|
| $8^4$ | 800 | 800 | 800 |
| $12^4$ | 400 | 400 | 400 |
| $16^4$ | 200 | 200 | 200 |

Table 2.1: The statistics of our Lüscher-Weisz gauge configurations.

In this section we use several observables that are sensitive to two predictions made by in the instanton model. These are the localization and the chirality of the associated fermion states. Some of those like the inverse participation ratio which is introduced in Section 2.2.3 give a measure for the localization of the modes. Others as the local chirality variable in Section 2.2.4 are sensitive to the interplay between localization and chirality. The results presented in the following are published in Refs. [GGR$^+$01b, G$^+$02b].

This section is organized as follows. First the technical details of our computations is given in Section 2.2.1. Then the density of eigenvalues near the origin is studied in Section 2.2.2. This density is linked to the chiral condensate by the Banks-Casher formula Eq. (2.1) and establishes the link between the near-zero modes and chiral symmetry breaking. In Section 2.2.3 the inverse participation ratio $I$ is introduced. This gives a measure for the localization of the whole eigenvectors. The relation to a similar chiral observable $I_5$ gives a first hint on the chiral character of the localized modes. In Section 2.2.4 a local chirality variable is employed to study the chiral properties of the regions of high density directly.

### 2.2.1 Technical details

We use quenched SU(3) gauge configurations generated with the Lüscher-Weisz gauge action (see Sec. 1.4.2) at three different values of the gauge coupling, $\beta_1 = 8.10$, $\beta_1 = 8.30$, and $\beta_1 = 8.45$ on $8^4$, $12^4$ and $16^4$ lattices. This corresponds to three different values of the lattice spacing $a = 0.125$ fm, 0.105 fm and 0.095 fm, respectively. The gauge updates consist of a mix of Metropolis and over-relaxation steps [Cre87]. An overview of the statistics is given in Table 2.1.

We investigate problems related to chiral symmetry. Therefore, we employ the chirally improved Dirac operator described in Section 1.6.5. To study the dependence on the magnitude of the eigenvalue, we computed the 50 lowest eigenvalues and -vectors with respect to their modulus for the $8^4$ and $12^4$ lattices; we restrict ourselves to 30 modes on the $16^4$ lattices. These eigenvalues and eigenvectors are computed using the implicitly restarted Arnoldi method [LSY98, Sor92]. Whereas the generation of the gauge configuration was done on workstations, the eigenvectors and eigenvalues were computed on the SR8000-F1 at the Leibniz Rechenzentrum in Munich.

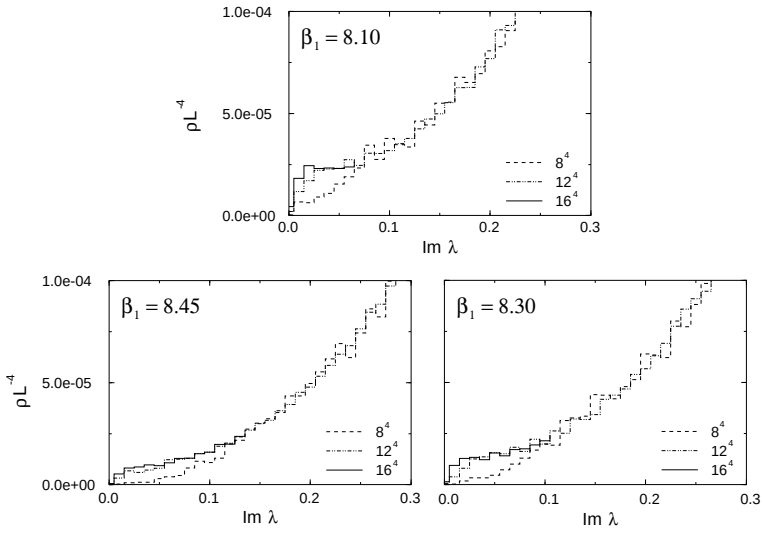


Figure 2.2: The density of eigenvalues as a function of $\mathrm{Im}\,\lambda$ divided by the volume for the three different values of $\beta_1$. We observe the universal behavior at larger eigenvalues. The drop at the origin diminishes as the volume grows.

### 2.2.2 Density of eigenvalues

The first object of the study is the density of eigenvalues $\rho(\lambda)$ near the origin. The interpretation of the lattice results has to include some modifications with respect to the continuum definitions. The identification of the zero modes is made by property 2) from Section 1.6.4. A mode is identified as a zero mode if $\psi^+\gamma_5\psi$ differs significantly from zero. Then it has a real eigenvalue and the corresponding eigenmode is for the chirally improved operator identified with the zero modes of the exact solution.

The spectrum of our Dirac operator is approximately on a circle and not on a line as in the continuum limit $a \to 0$. Therefore the definition of the density has to be changed. We bin according to the imaginary part of the eigenvalue and count the number of eigenvalues in each bin. As the real parts are small in the region we are interested in, this gives a good approximation of the spectral density. Furthermore, the density cannot extent right to the origin. This can be understood by universal arguments from random matrix theory. One finds that the microscopic gap at the origin becomes smaller for larger lattices. The behavior of the density at the origin has been extensively studied in [GMGW98, BBMS$^+$98, OV98, BB$^+$98, EHKN99, DHK99, GHR$^+$99].

In Figure 2.2 the result of our computation is shown. We plot only the region with $\mathrm{Im}\,\lambda > 0$, because the function is symmetric with respect to $\lambda \to \lambda^*$. The densities are scaled by $V^{-1}$ to get the combination in the Banks-Casher formula. In this way we obtain a universal curve for all volumes. Only at the origin

the three curves deviate from each other. This is the announced behavior; the expectation that the gap near the origin gets smaller with increasing volume is confirmed by the data. It will vanish in the limit $V \to \infty$. Up to this finite size effect the density remains non-zero all the way to the origin. According to the Banks-Casher formula a chiral condensate is build up.

### 2.2.3 Localization

Now we look into the localization properties of the near-zero modes. For an instanton configuration in the continuum the Dirac operator has an exact zero mode $\psi$, which is localized in space and time around the center of the instanton. In order to quantify the localization, consider the gauge invariant scalar density $p(x)$ and the pseudoscalar density $p_5(x)$

$$p(x) = \sum_{c,d} \psi(x,d,c)^* \psi(x,d,c) \equiv \psi^+(x)\psi(x) \ , \tag{2.10}$$

$$p_5(x) = \sum_{d,d',c} \psi(x,d',c)^* (\gamma_5)_{d',d} \psi(x,d,c) \equiv \psi^+(x)\gamma_5\psi(x) \ . \tag{2.11}$$

where $\psi(x,d,c)$ is the eigenvector of the lattice Dirac operator. We take the eigenvectors as normalized such that

$$\sum_x p(x) = 1 \ . \tag{2.12}$$

For an eigenvector $\psi$ of $D$, $\gamma_5\psi$ is also an eigenvector with $\gamma_5\psi = \pm\psi$, see discussion after Eq. (2.8). The sign depends on the configuration being an instanton or an anti-instanton. Thus, scalar and the pseudoscalar density are equal for a single anti-instanton configuration, whereas they have opposite sign for an instanton.

$$p_5(x) = \begin{cases} -p(x) & \text{for instantons} \\ +p(x) & \text{for anti-instantons} \end{cases} \tag{2.13}$$

These densities show a clear localization at the point of an isolated smooth instanton put on the lattice by hand [FLS$^+$85, GGL$^+$01]. As an alternative approach one can use cooling techniques to identify the instantons independently. It was found that the localization of the eigenvectors is concentrated at the same region where the cooling procedure finds an instanton, see, e.g., [CGHN94].

To quantify the localization further the *inverse participation ratio* $I$ has been introduced

$$I = V \sum_x p(x)^2 \ . \tag{2.14}$$

It is widely used in condensed matter physics. Let us consider some examples to understand the behavior of this observable. (Keep in mind that $p(x) \geq 0$!)

- The density has support only on one lattice point $x'$. Using the normalization condition Eq. (2.12) this states

$$p(x) = \delta_{xx'} \ . \tag{2.15}$$

  So, $p(x)^2 = \delta_{xx'}$ and if we sum this over all $x$ we get 1. By definition (2.14), the inverse participation ratio is $I = V$ in this case.

- If the density is maximally spread on all sites, the density is

$$p(x) = \frac{1}{V} \ . \tag{2.16}$$

  Here $p(x)^2 = 1/V^2$ for all $x$ and the inverse participation ratio gives 1.

- For $N$ non-overlapping objects with a volume $V_0$ each and $p(x) = c$ within the volume and $p(x) = 0$ outside we get $c = 1/NV_0$. Thus

$$I = V \sum_{i=1}^{N} \frac{1}{N^2 V_0^2} = \frac{V}{NV_0^2} = \frac{1}{\rho V_0} \ , \tag{2.17}$$

  where $\rho = NV_0/V$ is the density of the objects. Thus for a constant density, the inverse participation ratio should be independent of the volume $V$. Again, the smaller the objects, the higher is the localization.

To summarize: $I$ is large if the scalar density is localized. It decreases to 1 the more the density is spread out. It is thus an appropriate measure for the localization of an eigenmode.

From the instanton picture we expect that near-zero modes are dominated by weakly interacting instantons. They have a high localization and the inverse participation ratio should be large. Modes further away from the origin are dominated by configurations where the instantons and anti-instantons have a larger overlap. In other words they start to annihilate and lose their identity. Thus the localization is expected to be weaker for modes with larger imaginary part than for those with a smaller one.

In Figure 2.3 we show the result of the simulation. The inverse participation ratio is plotted versus the imaginary part of the corresponding eigenvalue $\mathrm{Im}\,\lambda$. The real modes have are left out. As the distribution is symmetric with respect to $\mathrm{Im}\,\lambda = 0$, we show the curve only for positive imaginary part. The data is from a $16^4$ lattice at three values of $\beta_1$.

The three curves have their maximum near the origin and decrease for larger values of $\mathrm{Im}\,\lambda$ as expected. Moreover, we can observe that the localization near the origin is largest for the smallest value of $\beta_1$, i.e. $\beta_1 = 8.10$. In Figure 2.2 we have seen that for this $\beta_1$ the chiral condensate is larger than for the larger values of $\beta_1$. It remains to be understood whether this is simply due to a larger

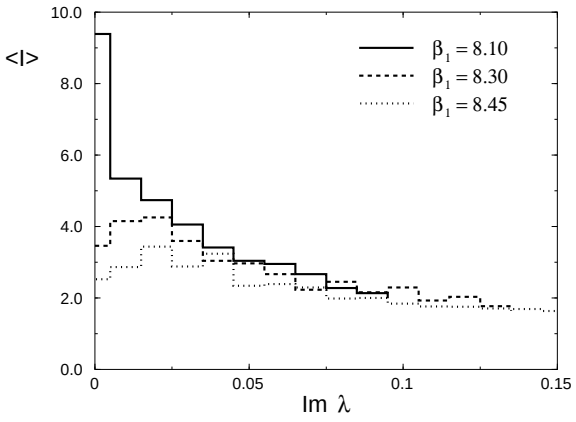


Figure 2.3: The average inverse participation ratio $\langle I \rangle$ of the near-zero modes as a function of $\lambda$. The lattice size is $16^4$. The real modes are left out.

number of localized states or the states themselves are more localized. Therefore, the probability distribution of $I$ is shown in Fig. 2.4 for those eigenvectors with $0 < |\mathrm{Im}\,\lambda| \leq 0.05$. In this $|\mathrm{Im}\,\lambda|$ range the curves in Fig. 2.3 depend on $\beta_1$ significantly. The curves are normalized such that their integral over $I$ is 1. The distribution for $\beta_1 = 8.10$ exhibits a maximum which is shifted to larger values of $I$ compared to the curves for larger $\beta_1$. This shows that the modes themselves are more localized for smaller values of $\beta_1$.

A second signature deduced from the instanton model is the chirality of the low lying eigenmodes. To quantify this, we consider the pseudoscalar density $p_5(x) = \psi^+(x)\gamma_5\psi(x)$ which is defined in Eq. (2.11). This density should have a negative sign near an instanton peak and a positive sign near an anti-instanton peak.

Analogously to the inverse participation ratio of Eq. (2.14), the pseudoscalar inverse participation ratio is defined by

$$I_5 = V \sum_x p_5(x)^2 \,. \tag{2.18}$$

This is a measure for the localization of the pseudoscalar density $p_5(x)$ in the same way as $I$ is for $p(x)$. For a single (anti)-instanton, $I_5$ is equal to the inverse participation ratio $I$, because $p(x) = |p_5(x)|$ for these configurations, see Eq. (2.13). According to the definitions Eqs. (2.10) and (2.11)

$$|p_5(x)| \leq p(x) \tag{2.19}$$

where we have used the definition of $\gamma_5$ from Eq. (A.4). For the inverse participation ratios this translates to

$$I_5 \leq I \,. \tag{2.20}$$

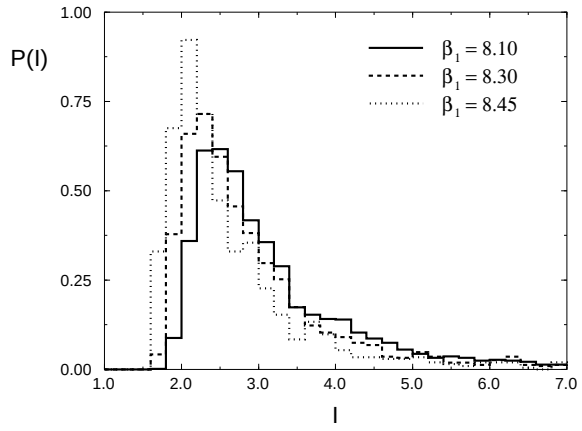


Figure 2.4: The distribution of the inverse participation ratio for modes with $0 < |\mathrm{Im}\,\lambda| \leq 0.05$. The lattice size is $16^4$.

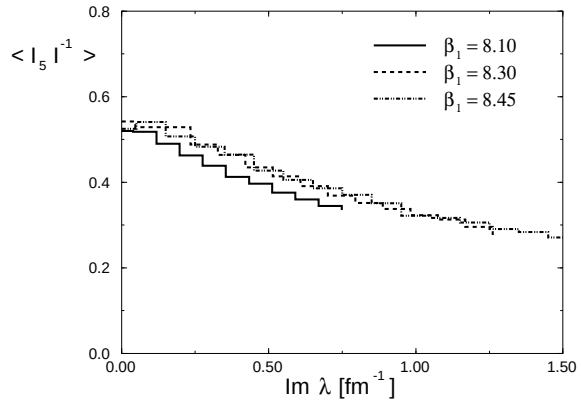


Figure 2.5: The ratio of the pseudoscalar density to the scalar density $I_5/I$ as a function of $\mathrm{Im}\,\lambda$. The data is shown in physical units on the $16^4$ lattices.

If we consider an ensemble of instantons and anti-instantons which are well separated, $p(x)$ and $|p_5(x)|$ are much the same over the whole volume and thus $I \approx I_5$. As these (anti)-instantons start to overlap, $p_5$ undergoes several changes of sign in places where $p(x)$ is far from zero; $I_5$ will be significantly smaller than $I$. For modes close to the origin, where we expect well defined (anti)-instantons, the ratio $I_5/I$ should be close to 1 and it should decrease for larger imaginary parts of the eigenvalue.

The result for this observable is shown in Fig. 2.5 as a function of $\mathrm{Im}\,\lambda$. The expected decrease of the ratio $\langle I_5/I \rangle$ as $|\mathrm{Im}\,\lambda|$ grows is observed. This supports the instanton model as it combines the two properties of instantons: the localization and the chirality of the excitations. The dependence on $|\mathrm{Im}\,\lambda|$ is rather similar for all three values of the gauge coupling $\beta_1$.

### 2.2.4 Local chirality

In the previous subsection, we have analyzed global observables to measure the localization and chirality of the low lying eigenmodes of the Dirac operator. Now we employ a local observable to test the coincidence of high density and chirality. It was proposed by Horváth et al. in [HIMT02] and induced a series of studies [DH02, HLN$^+$02, EH02, B$^+$02]. The scalar and pseudoscalar densities $p(x)$ and $p_5(x)$ are defined with a 1 and a $\gamma_5$ in Dirac space. Now the densities with positive and negative chirality $p_+(x)$ and $p_-(x)$ are formed with the projectors on positive and negative chirality

$$P_\pm = \frac{1}{2}(1 \pm \gamma_5) \ . \tag{2.21}$$

Using these projectors, we get the densities $p_\pm(x)$ as

$$p_\pm(x) = \sum_{d,d',c} \psi(x,d,c)^* (P_\pm)_{d,d'} \psi(x,d',c) \ . \tag{2.22}$$

We already discussed that for a classical instanton the corresponding eigenmode has negative chirality and $p(x) = -p_5(x)$; for an anti-instanton $p(x) = p_5(x)$. Thus for an instanton $p_+(x) = 0$ whereas for an anti-instanton $p_-(x) = 0$. The ratio $p_+(x)/p_-(x)$ is consequently expected to be zero for an instanton. For an anti-instanton this ratio should be $\infty$ everywhere. Horváth et al. now proposed to map this ratio onto the interval $[-1,1]$ using the arctangent. They defined the local chirality variable $X(x)$ as

$$X(x) = \frac{4}{\pi} \arctan\left(\sqrt{\frac{p_+(x)}{p_-(x)}}\right) - 1 \ . \tag{2.23}$$

For a single (anti)-instanton this variable $X$ should be $\pm 1$. The instanton model thus predicts a double peak structure with peaks near $\pm 1$ for the distribution of $X$.

Using this variable, the chirality of the sites with the highest scalar density is probed. For the near-zero modes the procedure is as follows. One chooses cuts on the scalar density $p(x)$ such that on average a certain percentage of the sites has larger $p(x)$. $X(x)$ is computed for each configuration on the sites with $p(x)$ larger than this cut. We compute the distribution of $X$ for different intervals of $|\mathrm{Im}\,\lambda|$. In order to compare this distribution for the different bins, we normalize it such that the integral is equal to 1.

We binned $|\mathrm{Im}\,\lambda|$ in steps of 0.01. For each of these bins the distribution of $X(x)$ is computed for the 1%, 6.25% and 12.5% of the sites with the highest $p(x)$. Because quantum fluctuations have a larger impact on sites with a lower density, the signal is expected to be stronger for a smaller percentage of the sites. On the other hand, the packing fraction of most instanton models is considerably larger than 1% (see, e.g., [DPW96]). In order to get a significant check of the instanton

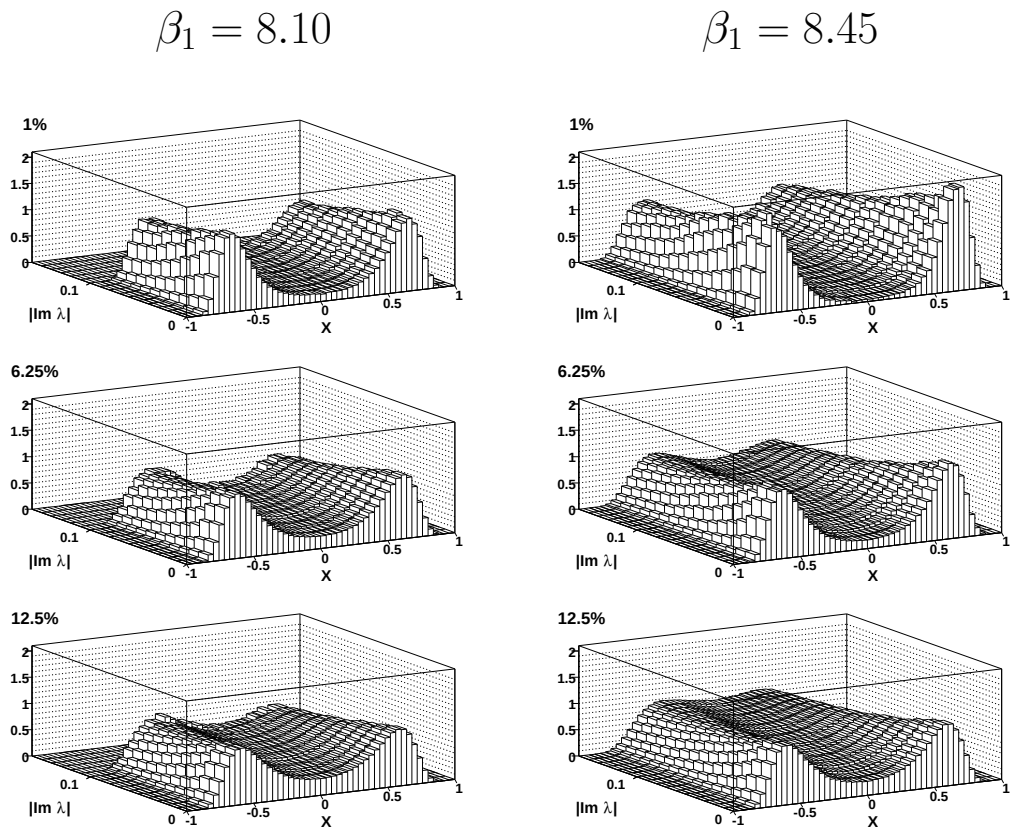


Figure 2.6: The local chirality for the near-zero modes. The lattice size is $16^4$ with $\beta_1 = 8.10$ on the left and $\beta_1 = 8.45$ on the right. The distribution is binned in $|\mathrm{Im}\,\lambda|$ and normalized to 1 for each $|\mathrm{Im}\,\lambda|$ bin individually. The three plots correspond to three different cuts in the number of points considered in the analysis. The 1% of all lattice points with the largest $p(x)$ are considered in the top plot. For the middle plot this cut is 6.25% and 12.5% for the lower plot.

predictions, it is thus necessary that the result remains valid for a larger fraction of the volume.

We use this procedure to compute the $X$ distributions for $\beta_1 = 8.10$ and $\beta_1 = 8.45$, which are shown in Fig. 2.6. In the top plot on average 1% of the sites with the largest $p(x)$ are used. For the modes closest to the origin, we see a clear double peak structure as predicted by the instanton model. The exactly real modes are left out. As $|\mathrm{Im}\,\lambda|$ grows, these peaks become less pronounced but are still clearly visible. The middle and the lower plot show the results for 6.25% and 12.5% of the points considered. Again, the peaks are well defined close to $|\mathrm{Im}\,\lambda| = 0$ and the double peak structure stays intact for the modes farther up in the spectrum. In other words the chiral characteristics of the modes is best for near-zero modes. The larger the imaginary part of the eigenvalue, i.e., the more

the mode turns into a bulk mode, the more it loses its chiral properties.

In Fig. 2.6 on the right, the distribution is shown for $\beta_1 = 8.45$. The gross features are the same as for $\beta_1 = 8.10$. Because we computed the same number of eigenmodes for both values $\beta_1$ but the density close to the origin is larger for larger $\beta_1$ (see Fig. 2.2), the $|\mathrm{Im}\,\lambda|$ bins now extend to $|\mathrm{Im}\,\lambda| = 0.15$ instead of $|\mathrm{Im}\,\lambda| = 0.10$ for $\beta_1 = 8.10$. If we compare the results for the two values of $\beta_1$, we observe that the double peak structure is more pronounced for the larger $\beta_1 = 8.45$ than for $\beta_1 = 8.10$. This can be understood as due to the stronger suppression of quantum fluctuations for larger values of $\beta_1$.

### 2.2.5 Conclusion

In this section, we have confronted the predictions of the instanton model for the low lying eigenmodes of the Dirac operator with a realistic lattice simulation. In particular, we have studied their localization, the chirality and the interplay of these two properties. First, we have shown that the density of eigenvalues is non-vanishing near the origin up to a microscopic gap which can be understood in random matrix theory.

Using the inverse participation ratio we have studied the localization of the eigenmodes. We found the localization to be largest for the smallest values of $|\mathrm{Im}\,\lambda|$, whereas it decreases for larger values. The probability distribution of $I$ has shown that it gets more likely to find a localized state for smaller $\beta_1$. The ratio between $I_5$ and the inverse participation ratio $I$ has proven to be quite stable under quantum fluctuations. Its deviation from 1 measures the deviation from pure, separated instanton states. We found that the larger $|\mathrm{Im}\,\lambda|$ the smaller this is ratio, again in agreement with the ideas from the instanton picture.

Finally, we considered the local chirality variable $X(x)$ which measures the chirality on a particular site. We showed that density and chirality are correlated. The chirality again has proven to be strongest in the vicinity of the origin. On the other hand, even for fractions of the lattice of the order of the usual instanton packing fraction, the peaks of the density turned out to be chiral.

To summarize, all predictions made by the instanton model could be reproduced by our Monte-Carlo simulation. However, we do not claim that these observables can provide any positive evidence for the validity of instanton model. The relevant excitations could in principle be of completely different origin. It will be a topic of future studies to find quantities that are more sensitive to the specific properties of instantons.

## 2.3 Topological excitations at finite temperature

Up to now we have studied QCD at zero temperature. If the temperature is increased, QCD is believed to lose two of its major characteristics. Chiral symmetry is restored and the theory no longer confines. Both phenomena are intrinsically non-perturbative and subject of intensive lattice studies. These suggest that both phase transitions happen at the same critical temperature $T_c$. In the preceding section we have studied the mechanism of chiral symmetry breaking below $T_c$. One of the purposes of this section is to look at the same observables while crossing the phase boundary. We present here results that are already published in Refs. [GGR$^+$01a]. For a study of the topological susceptibility across the phase transition see Ref. [GHS02b].

### 2.3.1 Finite temperature field theory

In the continuum the partition function for a quantum field theory at finite temperature is given by

$$Z = \int [\mathcal{D}U][\mathrm{d}\bar{\psi}][\mathrm{d}\psi] \exp(-\int_0^{\beta_T} \mathrm{d}t \int \mathrm{d}^3x \, \mathcal{L}[\bar{\psi}, \psi, U]) \tag{2.24}$$

with $\beta_T$ the parameter that is connected to the temperature $T$ by

$$\beta_T = \frac{1}{T} \, . \tag{2.25}$$

The Boltzmann constant $k_B$ is set to 1. The subscript $T$ is introduced to avoid confusing this $\beta$ with the various parameters of the gauge action. Thus formally one converts a quantum field theory to a thermal quantum field theory by restricting the time integral to the finite extent $[0, \beta_T]$ and using periodic boundary conditions for the bosonic fields and anti-periodic boundary conditions for the fermionic fields.[1]

[1] For a single bosonic field $\phi$ this is is easily understood taking into account that the transition amplitude (with $H$ the Hamiltonian of the theory) is given by

$$\langle \phi(\mathbf{x_1}, t_1) | \phi(\mathbf{x_2}, t_2) \rangle = \langle \phi_1 | e^{-H(t_1 - t_2)} | \phi_2 \rangle = N \int [\mathrm{d}\phi] e^{-S} \tag{2.26}$$

with $S = \int_{t_2}^{t_1} \mathrm{d}t \int \mathrm{d}^3x \mathcal{L}$ the action and $\mathcal{L}$ the corresponding Lagrangian. The path integral is defined in this case over paths with $\phi(\mathbf{x_1}, t_1) = \phi_1$ and $\phi(\mathbf{x_2}, t_2) = \phi_2$. The partition function is, thus, given by the following path integral

$$Z = \mathrm{tr}\, e^{-\beta H} = \int \mathrm{d}\phi \langle \phi | e^{-\beta H} | \phi \rangle = N \int [\mathrm{d}\phi] e^{-S} \tag{2.27}$$

if one identifies $\beta = t_1 - t_2$. Thus, the (bosonic) fields have to obey periodic boundary conditions $\phi(\mathbf{x}, \beta) = \phi(\mathbf{x}, 0)$, see, e.g., [Das97] for further information.

$$\begin{aligned} A_\mu(\mathbf{x}, t=0) &= A_\mu(\mathbf{x}t = \beta_T) \\ \bar{\psi}(\mathbf{x}, t=0) &= -\bar{\psi}(\mathbf{x}, t=\beta_T) \\ \psi(\mathbf{x}, t=0) &= -\psi(\mathbf{x}, t=\beta_T) \end{aligned} \tag{2.28}$$

On the lattice the temperature is thus given by the time extent of the lattice $L_t$

$$\frac{1}{T} = \beta_T = \frac{1}{L_t\, a} \ . \tag{2.29}$$

The continuum limit of such a theory on the lattice is then given by keeping the product $L_t a$ fixed while taking $a$ to zero.

To study the chiral and the deconfinement phase transitions we need appropriate order parameters. For the chiral phase transition the non-vanishing value of the chiral condensate indicates the breaking of chiral symmetry

$$\langle \bar{\psi}\psi \rangle \neq 0 \ . \tag{2.30}$$

For the deconfinement phase transition this is the expectation value of the Polyakov loop $L_{\mathbf{x}}$ [Pol78, SY82]. On the lattice for a quenched theory it is the product of the link variables along a path in the time direction.

$$L_{\mathbf{x}} = \mathrm{tr} \left\{ \prod_{x_1=4}^{L_t} U(\mathbf{x}, x_4)_{\mu=4} \right\} \tag{2.31}$$

A remarkable property of the SU($N$) gauge actions is an additional Z($N$) symmetry which is dynamically broken above the deconfinement phase transition. Z($N$) is the center of the SU($N$) group. The center $\mathcal{C}$ of a group $\mathcal{G}$ is the subgroup of elements which commute with all elements of the $\mathcal{G}$.

$$\mathcal{C} = \{ z \in \mathcal{G} | zgz^{-1} = g \text{ for all } g \in \mathcal{G} \} \tag{2.32}$$

To be specific for the group SU(3) the center Z(3) is represented by

$$\{ \mathbf{1}_3, \mathbf{1}_3 \exp(-\frac{2i}{3}\pi), \mathbf{1}_3 \exp(\frac{2i}{3}\pi) \} \ . \tag{2.33}$$

The Z(3) transformation of the link variables $U_\mu$ is defined on all time-like links originating from a common timelike hyperplane. For a fixed $x_4$ we have

$$U(\mathbf{x}, x_4)_{\mu=4} \longrightarrow z U(\mathbf{x}, x_4)_{\mu=4} \ , \quad z \in \mathrm{Z}(3) \ . \tag{2.34}$$

The breaking of this symmetry is manifest in the expectation value of the Polyakov loop $L_{\mathbf{x}}$. Obviously, it transforms under $z \in Z(3)$ as

$$L_{\mathbf{x}} \longrightarrow \frac{\mathrm{tr}\, z}{3} L_{\mathbf{x}} \ . \tag{2.35}$$

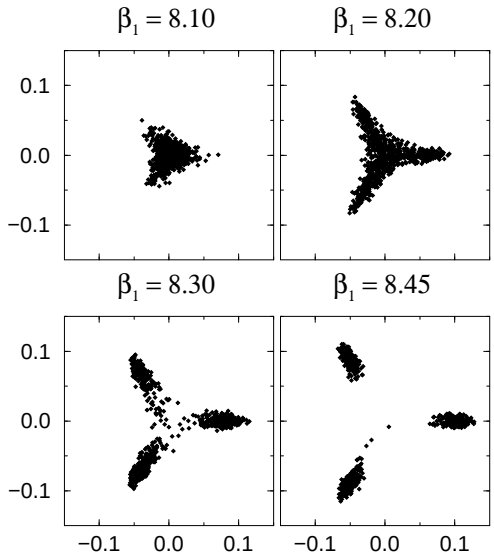


Figure 2.7: The Polyakov loop in the complex plane. The $x$-axis is the real part the $y$-axis the imaginary part of the Polyakov loop. Each point is $L$ on one of 800 configurations on a $6 \times 16^3$ lattice. For $\beta_1 = 8.10$ the system is well below $T_c$. The other plots show the emerging of the three disjoint Z(3) sectors.

Therefore it is clear that a non-zero value of

$$\langle L \rangle = \langle \frac{1}{V_3} \sum_{\mathbf{x}} L_{\mathbf{x}} \rangle \tag{2.36}$$

indicates the breaking of the Z(3) symmetry. However, the expectation value of the Polyakov loop is zero in the confining phase in the quenched approximation only. The fermion part of the action explicitly breaks the Z(3) symmetry. In the presence of dynamical quarks, thus, the Polyakov loop has a non-vanishing value in both phases.

To get an idea of how the Polyakov loop behaves consider Fig. 2.7. There the Polyakov loop for four values of the gauge coupling is plotted. Each of the points represents its value on one of 800 gauge configurations on a $6 \times 16^3$ lattice. The values of $\beta_1$ of 8.10, 8.20, 8.30, and 8.45 correspond for this lattice size to a temperature of 263 MeV, 286 MeV, 313 MeV, and 346 MeV, respectively. The critical temperature $T_c$ is about 300 MeV. Below $T_c$, in the confined phase, the Polyakov loop scatters around the origin. Approaching the critical temperature leads to the formation of three different branches, which are still connected by a finite density at the origin. Above the phase transition at $\beta_1 = 8.30$ the three Z(3) sectors split. The density at the origin decreases sharply. At the highest temperature the density at the origin is almost zero and we have three well separated clusters.

| | $\beta_1 = 8.10$ | $\beta_1 = 8.20$ | $\beta_1 = 8.30$ | $\beta_1 = 8.45$ |
|---|---|---|---|---|
| $a$ | 0.125(1) fm | 0.115(1) fm | 0.105(1) fm | 0.095(1) fm |
| $6 \times 12^3$ | 1200 | — | — | 1200 |
| $6 \times 16^3$ | 800 | 800 | 800 | 800 |
| $6 \times 20^3$ | 400 | — | — | 400 |

Table 2.2: The statistics for our gauge field ensembles together with the lattice spacing $a$.

While purely gluonic observables like the Polyakov loop show the Z(3) symmetry in their spectrum, fermionic observables may behave differently in the three sectors. This is due to the fact that the fermionic action is not invariant under the Z(3) symmetry transformation defined in Eq. (2.34). In the following, we refer to the *real sector* for configurations with a Polyakov loop in the right sector with an almost vanishing imaginary part. The combined sectors with phases $\approx \pm 2\pi/3$ are called the *complex sector*.

### 2.3.2 Technical details

The results are obtained on an ensemble of quenched gauge configurations generated with the Lüscher-Weisz gauge action that is discussed in Section 1.4.2. We use lattices with $6 \times 12^3$, $6 \times 16^3$ and $6 \times 20^3$ sites and simulate at four different values of the gauge coupling parameter $\beta_1 = 8.10$, 8.20, 8.30, and 8.45 such that half of these ensembles are below the critical temperature and half above. A detailed overview of the statistics can be found in Table 2.2. For the fermions we use the chirally improved Dirac operator, see Section 1.6.5 for details.

As in Section 2.2 the eigenvalues $\lambda$ and eigenvectors $\psi$ of the Dirac operator $D\psi = \lambda\psi$ are obtained with the implicitly restarted Arnoldi algorithm. For each gauge configuration we compute the 50 eigenvalues closest to the origin with respect to their modulus. One has to keep in mind that for the different volumina the Dirac operator has a different density of eigenvalues in lattice units. For a fixed $\beta_1$, i.e. fixed lattice spacing, a larger volume means a larger density of eigenvalues near the origin. In the chirally symmetric phase for $\beta_1 = 8.10$ the largest eigenvalue has an imaginary part of approximately 0.3 on the $6 \times 12^3$ lattice while it reaches only $\approx 0.14$ on the $6 \times 20^3$ lattice. As some of the observables are sensitive to this cut-off, we will cut the data at a common physical value, i.e., by $|\mathrm{Im}\,\lambda| < 0.14$ in these cases.

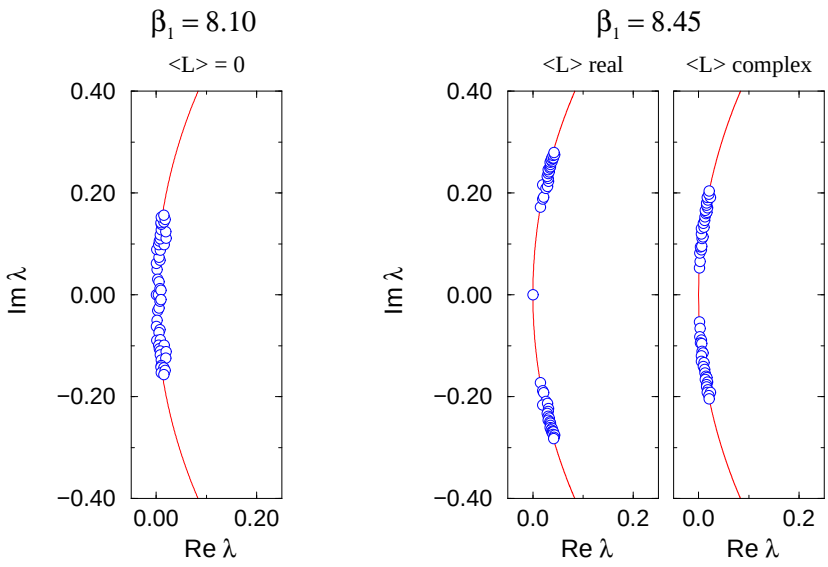


Figure 2.8: Examples for spectra of the Dirac operator. We show the 50 eigenvalues closest to the origin, represented by circles. All spectra are for $6 \times 20^3$ lattices. On the left hand side we plot the eigenvalues $\lambda$ in the complex plane for $\beta_1 = 8.10$ (chirally broken phase). The two plots on the right hand side show spectra at $\beta_1 = 8.45$ (chirally symmetric phase, no gap) for a gauge configuration with the Polyakov loop in the real sector (large gap) as well as for a configuration with complex Polyakov loop (small gap). The full curve in the plots indicates the Ginsparg-Wilson circle.

### 2.3.3 The spectrum of the Dirac operator

The Banks-Casher formula Eq. (2.1) relates the density of eigenvalues near the origin to the chiral condensate. Below the critical temperature $T_c$ we are in the chirally broken phase, so the spectrum should show a non-vanishing density of eigenvalues $\rho(\lambda)$ reaching to the origin. Above the phase transition a gap is expected such that the density vanishes in a certain interval around the origin $\lambda = 0$.

In Fig. 2.8 examples of such spectra are shown. On the left we see the spectrum on a configuration below the critical temperature. There is no gap at the origin. According to the Banks-Casher relation this implies a non-vanishing chiral condensate. On the right, two spectra in the deconfined phase are shown. The central plot results from a configuration with a Polyakov loop in the real sector. The very right plot is a spectrum in the complex sector. In both plots the formation of a gap is clearly visible. These are typical spectra in the sense that the gap in the real sector is about twice as big as in the complex sector.

To get a more quantitative picture of the change of the spectrum at the phase transition we compute the density of eigenvalues below and above $T_c$ for the real

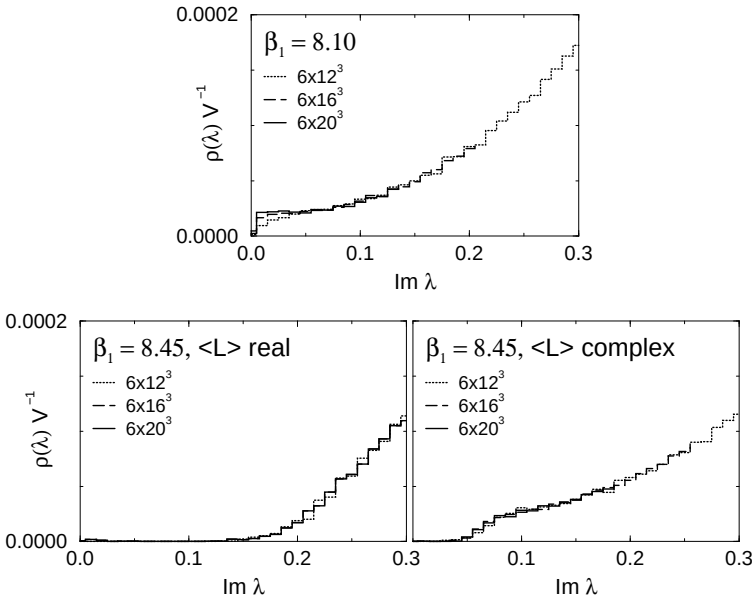


Figure 2.9: Histogram plots for the spectral density $\rho(\lambda)$ normalized with the inverse volume $V^{-1}$ as a function of Im $\lambda$.

and the complex sector. The result for three different lattice sizes is shown in Fig. 2.9. The density is scaled by the volume to get the relevant combination for the Banks-Casher formula. In the top plot, we display the spectral density below the critical temperature. It exhibits a non-vanishing density all the way to the origin. The microscopical gap right at the origin can be understood in random matrix theory and is discussed in Section 2.2.2. It is a finite size effect that vanishes for $V_3 \to \infty$. The two plots for $\beta_1 = 8.45$ show a result above the phase transition. The curves again coincide for the different volumina. The density drops to zero already at non-vanishing values of Im $\lambda$. Thus the chiral condensate is zero. For one of the samples ($6 \times 16^3$) we get a small signal quite close to the origin. This is a fluctuation which has no physical consequences. It does not show up for the larger lattices and will become insignificant for larger volumes and higher statistics.

### 2.3.4 Localization: Qualitative Discussion

In Section 2.2 we have studied the localization properties of the near-zero modes. We found the eigenmodes closer to the origin to be more localized and chiral as those further away from the origin. This is in agreement with the instanton model which describes chiral symmetry breaking by the interaction of localized, chiral excitations called instantons. These are classical solutions of the field equations at zero temperature. Similar solutions — the *calorons* — exist for finite temperature, too. These are string like objects in time direction with corresponding localization

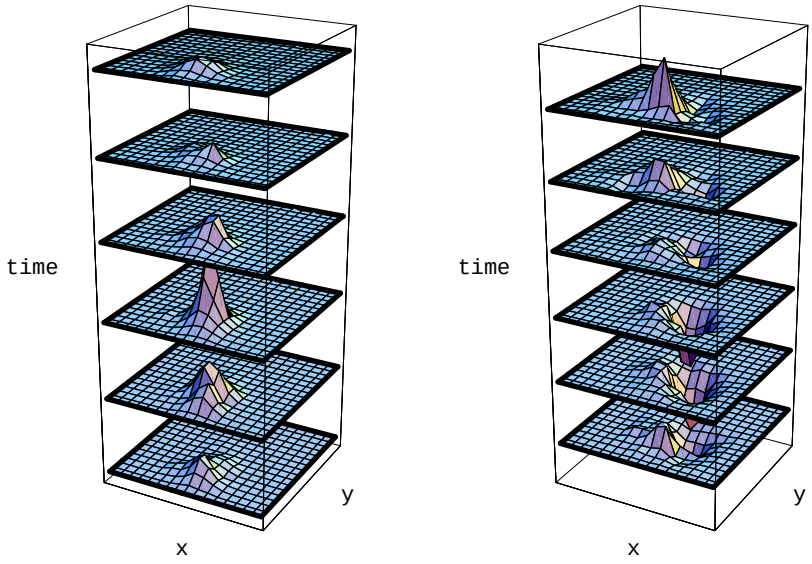


Figure 2.10: The 6 $x$-$y$ time-slices of the pseudoscalar density $p_5(x)$ for a zero mode (left plot) and a configuration with an interacting caloron anti-caloron pair, a so-called topological molecule (right plot). The data are from the $\beta_1 = 8.45$ sample on the $6 \times 16^3$ lattice.

properties. However, the transition between instantons and calorons is continuous as small instantons and calorons hardly feel the effect of the limited time extend. Therefore, as we do not want to speculate on the particular form, we will use the term *topological excitations* in the following. We will study the dependence of the localization properties of the eigenvectors of the Dirac operator, in order to understand the rôle of localized modes in the creation and vanishing of the chiral condensate.

In the previous section we used the scalar density $p(x) = \psi^+(x)\psi(x)$ and the pseudoscalar density $p_5(x) = \psi^+(x)\gamma_5\psi(x)$, see Eqs. (2.10) and (2.11), as measures for the localization and the chirality of the eigenvectors of the Dirac operator. To get a visual impression of their behavior for an interacting caloron anti-caloron pair we have taken one of our configurations and plotted in Fig. 2.10 these densities at the 6 time slices for a fixed $x$-$y$–plane of the $6 \times 16^3$ lattice. In the caloron picture the interaction of such a pair generates a near-zero mode of the Dirac operator. A similar behavior of the eigenvectors was observed for the staggered Dirac operator in [GRS$^+$01].

### 2.3.5 Localization: Quantitative results

To get a more precise picture of the localization properties of the eigenvectors, we again use the inverse participation ratio (IPR) $I$ of Eq. (2.14) and the pseudoscalar inverse participation ratio (PIPR) $I_5$ defined in Eq. (2.18). These give

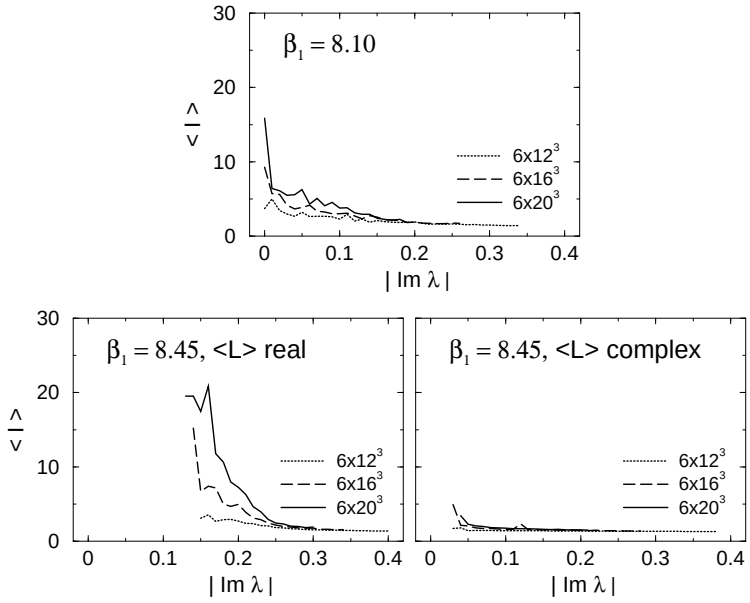


Figure 2.11: The inverse participation ratio as a function of |Im $\lambda$|.

global measures of the localization of an eigenvector. Larger IPR means larger localization of the eigenvector. From the PIPR one gets information about the chiral properties of the localized objects. For a classical instanton $I$ and $I_5$ are equal. The smaller $I_5$ is as compared to $I$, the less the localization is correlated with chirality. But this is not very conclusive. Therefore, we will subsequently use the local chirality variable $X(x)$ defined in Eq. (2.23) to study this correlation in a more precise way.

In Fig. 2.11 the inverse participation ratio is plotted as a function of the imaginary part of the eigenvalue |Im $\lambda$|. In the upper plot the result below the phase transition is shown. We get similar results as for the zero temperature ensemble, see Fig. 2.3. The most localized states are near |Im $\lambda$| = 0. As has been discussed previously in Section 2.2.3, this can be understood as a consequence of a fluid of topological excitations. An isolated excitation generates a zero mode of the Dirac operator. This is shifted to finite imaginary part as several of them start to interact.

In the lower plots the function is shown in the chirally symmetric phase at $\beta_1 = 8.45$. For the real sector on the left there are no eigenvalues up to |Im $\lambda$| $\approx 0.14$. Thus, we are above the phase transition where the chiral condensate vanishes. But despite this fact the picture is similar to the chirally broken phase at $\beta_1 = 8.10$. Above the gap we see, again, that the most localized states are at small values of |Im $\lambda$|. The localization decreases for larger imaginary parts of the eigenvalue. On the other hand, this behavior is much less visible in the complex sector. This has been expected. The classical solutions show a much weaker

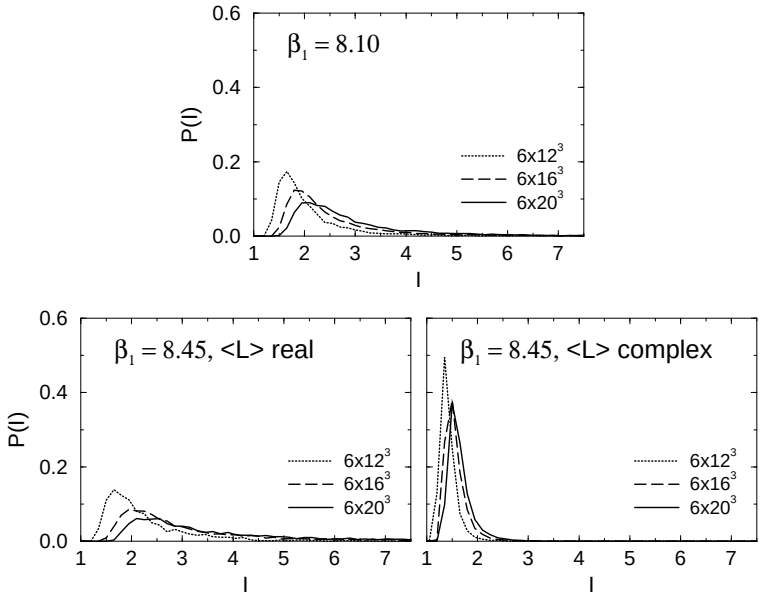


Figure 2.12: Distribution of the inverse participation ratio below (top plot) and above (bottom plots) the phase transition. In the high temperature phase, the picture differs significantly for the complex and the real sector.

localization in this sector, too, see the appendix of [GGR+01a].

The probability distribution for the IPR is plotted in Fig. 2.12 below the phase transition (top) and in the two sectors of the deconfined phase (bottom). In each of these cases we see a tendency towards stronger localization for larger volumes of the lattice. This is consistent with predictions made in models of topological excitations like the instanton model. As in the previous discussion of the IPR as a function of $|\mathrm{Im}\,\lambda|$, the result for the chirally broken phase and the real sector of the chirally symmetric phase hardly differ. However, there is a large difference to the complex sector. There, the distribution is peaked at small values of the inverse participation ratio. This is consistent with the picture of weakly localized objects in this region.

To further study the dependence of topological excitations on the temperature — that is on $\beta_1$ for fixed lattice geometry — we look at the number of eigenvectors which have an inverse participation ratio larger than some constant $c$. This number will be called $N(c)$. Analogously we define $N_5(c)$ for the pseudoscalar inverse participation ratio. The zero modes are excluded from this analysis.

We have already discussed that the chiral condensate is built up by topological excitations which slightly overlap. By doing so, they create small imaginary eigenvalues of the Dirac operator. Via the Banks-Casher relation Eq. (2.1) the density of these eigenvalues is responsible for the chiral condensate. As the chiral condensate vanishes at the phase transition, we expect the number of localized

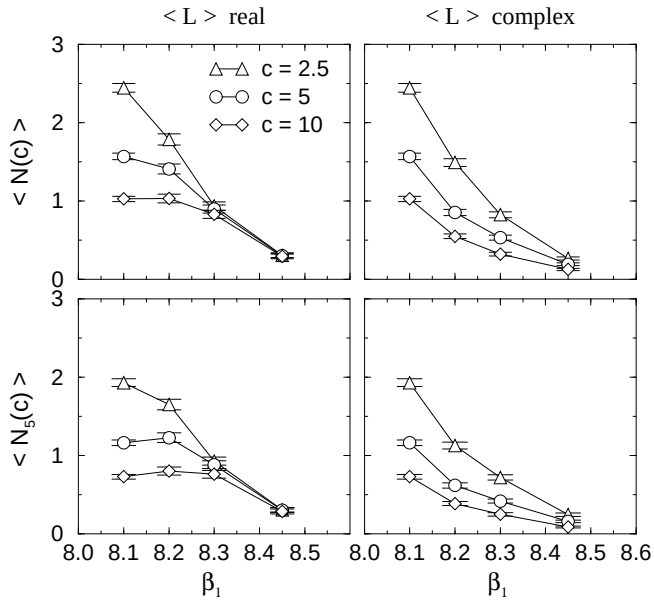


Figure 2.13: Average of $N(c)$ and $N_5(c)$ the numbers of eigenvector with $I > c$ and $I_5 > c$ respectively, as a function of $\beta_1$. Zero modes are omitted in the evaluation of $N(c)$ and $N_5(c)$. We display our results from $6 \times 16^3$ lattices for three values of the cut $c$.

modes to drop as $\beta_1$ is increased.

The result for three different cuts $c = 2.5$, 5, and 10 is shown in Fig. 2.13 on the $6 \times 16^3$ lattice for the four values of $\beta_1$. We observe a decline in the real as well in the complex sector with growing $\beta_1$. The functional form of $N$ and $N_5$ versus $\beta_1$ is similar. This supports the picture of topological objects that decrease in density but keep their chirality.

### 2.3.6 Local chirality

To verify the last findings, we now have a look at the local chirality variable $X(x)$ of Eq. (2.23), which we already used at zero temperature in Section 2.2.4. It maps the ratio of the density of positive chirality to the density of negative chirality on to the interval $[-1, 1]$. A double peak structure in the distribution of $X$ is the signal for the chirality of the eigenvectors. This variable is evaluated on the sites with a high scalar density. In this way the correlation between high density and chirality is probed. The cuts on the density are chosen such that on average 1%, 6.25% and 12.5% of all sites are used in the analysis.

To start, the distribution of the local chirality variable for the zero modes is presented in Fig. 2.14. It is computed on 55 gauge configurations at $\beta_1 = 8.10$ on $6 \times 20^3$ lattices. The $\beta_1 = 8.45$ sample consists of 55 configurations, too. This

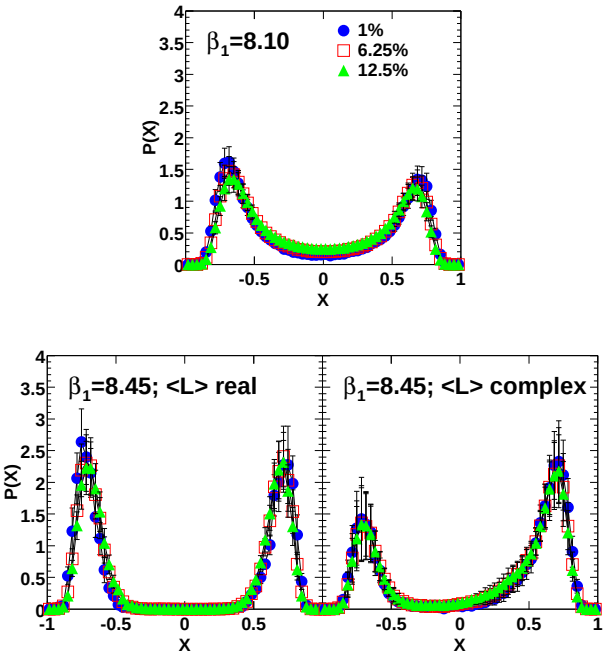


Figure 2.14: Local chirality for the zero modes. We present data for both sides of the phase transition. For the chirally symmetric phase, we distinguish between the real and the complex sector of the Polyakov loop. We use different values for the cut-off on the percentage of supporting lattice points: 1%, represented by filled circles, 6.25%, open squares and 12.5%, filled triangles. The data are computed on the $6 \times 20^3$ lattice.

statistics has to be split into the complex and the real sector with an approximate $2:1$ ratio. The curves are normalized such that the integral is equal to 1. The apparent asymmetry in the complex sector can be attributed to the low statistics.

As we can observe a clear double peak structure, the zero modes are predominantly chiral. The curves do not depend much on the percentage of lattice points included in the analysis. The local chirality in the chirally broken phase seems to be weaker than above the phase transition. This can be explained by the stronger ultraviolet fluctuations for lower values of $\beta_1$.

Let us now turn to the near-zero modes. The dependence of the distribution of the local chirality on the magnitude of the imaginary part as well on the percentage of lattice points included is shown in Fig. 2.15 on the left. The data is from the $6 \times 20^3$ lattice with $\beta_1 = 8.10$. The top plot shows the modes with $|\mathrm{Im}\,\lambda| < c_1$, where $c_1 = 0.018$ is chosen such that 20% of our eigenvectors contribute to this bin. In the middle plot we show the distribution in the next bin $c_1 \leq |\mathrm{Im}\,\lambda| < c_2$, which contains the result for 40% of the modes for $c_2 = 0.057$. The last 40% of the eigenvectors lead to the lower plot. Again, in each of the plots there are three curves that originate from three different cuts on the scalar

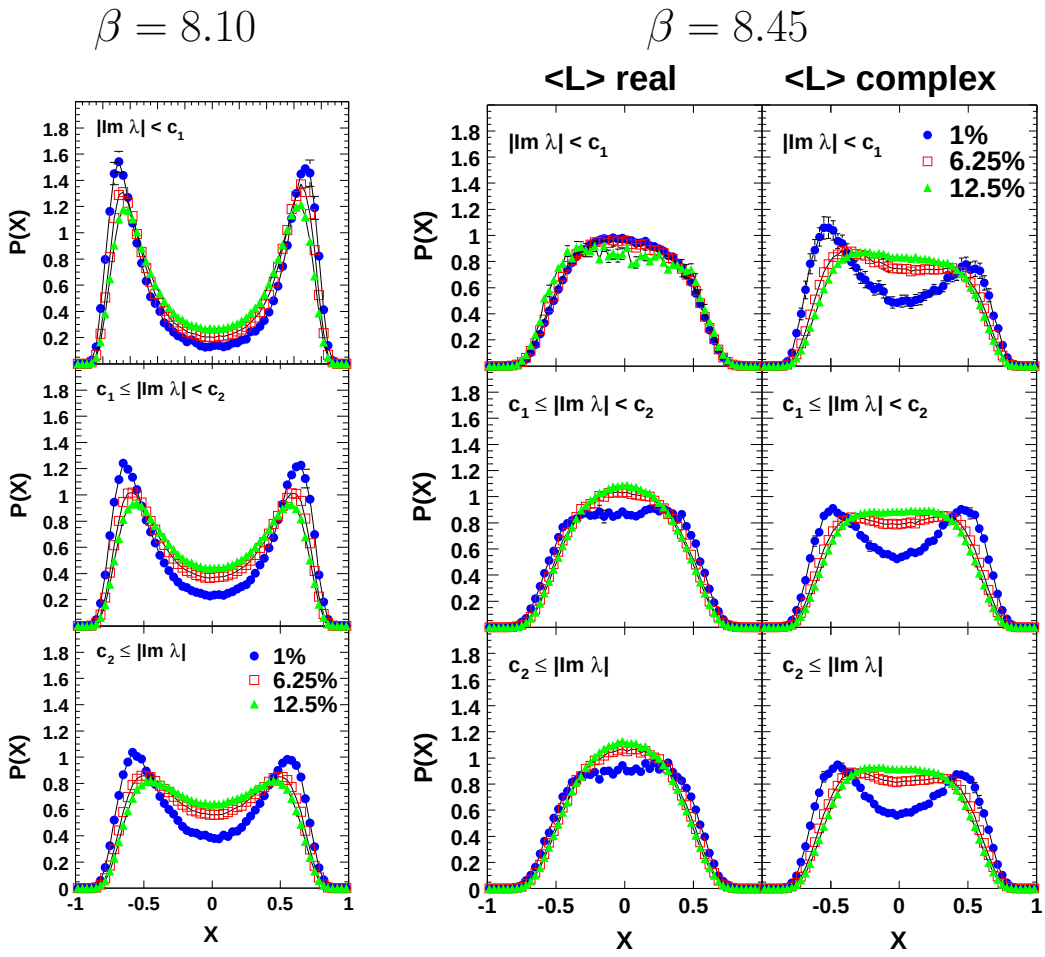


Figure 2.15: Local chirality for non-zero modes in the chirally symmetric phase on the left and in the broken phase on the right. The lattice size is $6 \times 20^3$ in both cases. For $\beta_1 = 8.45$, we divide our data with respect to the sector of the Polyakov loop. The left column contains the results for real $\langle L \rangle$, the right column shows data for complex $\langle L \rangle$. We bin the eigenvectors with respect to the imaginary parts of the corresponding eigenvalues such that the first bin ($|\text{Im } \lambda| < c_1$, top plot) shows the very near-zero modes (closest to the edge for $\beta_1 = 8.45$), while the other two bins ($c_1 \leq |\text{Im } \lambda| < c_2$, middle plot and $c_2 \leq |\text{Im } \lambda|$, bottom plot) show the local chirality for eigenvectors with eigenvalues higher up in the spectrum. The choice of the thresholds $c_i$ is discussed in the text and different for the three columns.

density $p(x)$. We see that even if the signal for the local chirality is strongest for the near-zero modes and becomes weaker as $|\mathrm{Im}\,\lambda|$ grows, the local chirality stays intact for the eigenvectors with larger $|\mathrm{Im}\,\lambda|$. Furthermore, the result for the near-zero modes closest to the origin is almost indistinguishable from the one for the zero modes. The curves hardly depend on the $p(x)$ cut for the modes closest to the origin, whereas the dependence is larger for the eigenvectors higher up in the spectrum. All this supports the assumption of a smooth transition from the zero mode physics to the near-zero modes. Hence, the picture of a fluid of topological objects — calorons and anti-calorons — that lose their identity the more they overlap and simultaneously generate a higher $|\mathrm{Im}\,\lambda|$, is made plausible by these observations. For $|\mathrm{Im}\,\lambda| > c_2$ the highest peaks still carry chirality but as the density gets smaller, quantum fluctuations get more and more important.

In Fig. 2.15 on the right the same plots are shown for the chirally symmetric phase at $\beta_1 = 8.45$, while the sector with real Polyakov loop can be found on the left. The partitioning of the eigenvectors in three bins of 20%, 40%, and 40% with respect to $|\mathrm{Im}\,\lambda|$ yields $c_1 = 0.207$ and $c_2 = 0.230$. These values differ from the chirally broken phase due to the creation of the gap around $|\mathrm{Im}\,\lambda| = 0$ which makes the chiral condensate vanish. In the complex sector this gap is significantly smaller and, thus, $c_1 = 0.081$ and $c_2 = 0.112$.

In the real sector the local chirality has vanished entirely, regardless of the eigenvector's imaginary part. The topological excitations do not exist in this phase, as the chiral condensate has vanished, too.

In the complex sector only 1% of the lattice points show a local chirality. There is no dip visible in the graphs with a higher percentage of the sites encountered. This means that there, too, are no extended objects with a chiral character.

## 2.4 Summary

We investigated the mechanism of chiral symmetry breaking and its restoration in QCD. Via the Banks-Casher relation, the density of eigenvalues of the Dirac operator near the origin gives the chiral condensate. If this density doesn't vanish, chiral symmetry is broken. One explanation for the emergence of a non-zero density is given by the interaction of instantons. Thus, we wanted to verify, whether instantons really play a pivotal rôle in the low lying spectrum of the Dirac operator. As a single instanton is a localized object with a definite chirality, we examined observables that are sensitive to localization and chirality. The main results are:

- The density of eigenvalues extends to the origin below the critical temperature $T_c$. Above the phase transition, we observe a gap in the spectral density — chiral symmetry is restored.

- We looked at the inverse participation ratio $I$ as a measure for localization.

In the low temperature phase, the localization is largest for the eigenvalues with the smallest imaginary part. For larger imaginary part the localization gets smaller.

- In the high temperature phase, the eigenvalues with the smallest imaginary parts are those directly above the edge of the gap in the spectrum. The corresponding eigenvectors exhibit a strong localization as well, which gets smaller the further the eigenvalue is away from this edge.

- Using the local chirality variable $X$, we looked into the correlation between localization and chirality, which is predicted by the instanton model. We found a clear correlation in the chirally broken phase which is relatively stable for larger imaginary parts of the eigenvector. Above the phase transition, the chirality of the excitations is still observable at the very edge of the gap. But it is diluted by quantum fluctuations of the bulk modes.

All these observations agree with a dominant rôle of topological excitations like the instanton or caloron. Below the phase transition these excitations are responsible for the breaking of chiral symmetry. Above $T_c$ they still can be detected in the low lying eigenmodes but they are no longer sufficiently abundant and chiral symmetry is restored.

# Chapter 3

# Hadron Spectrum

The masses of hadrons are a subject of intensive studies in lattice QCD. This is for two reasons. On the one hand, they can be computed to high accuracy directly on the lattice without the need of renormalization. In particular the ratios of different particle masses can be predicted with low theoretical uncertainty. On the other hand, the masses of a large number of particles are known experimentally with an almost negligible error. Hence, this field offers a perfect ground for the comparison of theoretical predictions with experimental data.

This chapter is organized as follows. In Section 3.1 we present the technique used to extract the masses from two-point functions of interpolating fields. Subsequently, their computation on the lattice is described in Section 3.2. To get a good overlap between the physical particle and the interpolating fields, we use the Jacobi smearing method, which is the subject of Sec. 3.2.3. In Section 3.3 we present first results for the hadron spectrum obtained with the chirally improved Dirac operator. Additional information together with a comparison to the parameterized Fixed Point operator can be found in [G$^+$02a].

## 3.1 Lattice calculation of hadron masses

Lattice QCD a priori doesn't know anything about a spectrum of bound particles. Therefore, we need operators which have an overlap with the hadron in question to filter out the relevant information. We compute the energy of a hadron $H(\mathbf{p})$ with momentum $\mathbf{p}$ from the dependence on the time separation $t$ of two-point functions of the following form

$$\langle M_1(\mathbf{p},t) M_2(\mathbf{p},0)\rangle \tag{3.1}$$

where $M_1(\mathbf{p},t)$ and $M_2(\mathbf{p},t)$ are the *interpolating fields* for the hadron sink and source on time-slice $t$, respectively. These are required to have a non-vanishing overlap with the particle state $H(\mathbf{p})$ in question, i.e.

$$\langle 0|M_1(\mathbf{p},t)|H(\mathbf{p},t)\rangle \neq 0 \qquad \text{and} \qquad \langle H(\mathbf{p},t)|M_2(\mathbf{p},t)|0\rangle \neq 0\,. \tag{3.2}$$

This implies that they must have the same quantum numbers as the particle in question, i.e. flavor structure, spin, and parity. For the $\pi^+$ (a pseudoscalar meson) this might be, e.g.,

$$\begin{aligned} M_1(\mathbf{p},t) &= \sum_{\mathbf{x}} e^{-i\mathbf{x}\mathbf{p}} \bar{d}^c_\alpha(\mathbf{x},t)(\gamma_5)_{\alpha,\alpha'} u^c_{\alpha'}(\mathbf{x},t) \\ M_2(\mathbf{p},t) &= \sum_{\mathbf{x}} e^{i\mathbf{x}\mathbf{p}} \bar{u}^c_\alpha(\mathbf{x},t)(\gamma_5)_{\alpha,\alpha'} d^c_{\alpha'}(\mathbf{x},t) \end{aligned} \tag{3.3}$$

where $\mathbf{x}$ denotes the space index, $\alpha$ and $\alpha'$ are the Dirac indices and $c$ the color indices. Repeated indices are summed over. $u$ is the $u$-quark field and $d$ the $d$-quark field located on time-slice $t$.

The idea is to evaluate the dependence of the two-point function Eq. (3.1) on the time separation $t$. The time evolution operator in Euclidean space-time is $\exp(-tH)$ with $H$ the Hamilton operator of the theory. Using it together with the periodic boundary conditions, Eq. (3.1) becomes

$$\langle M_1(\mathbf{p},t) M_2(\mathbf{p},0)\rangle = \langle M_1 e^{-tH} M_2 e^{-(T-t)H}\rangle \tag{3.4}$$

with $T$ the time extend of the lattice. Now we use the eigenstates $|i\rangle$ of the Hamilton operator that form a complete orthonormal set:

$$H|i\rangle = E_i|i\rangle \qquad\qquad 1 = \sum_i |i\rangle\langle i| \tag{3.5}$$

The eigenvalues $E_i$ are the energies of the states. If they are ordered such that $E_0 \leq E_1 \leq E_2 \leq \ldots$, Eq. (3.4) becomes

$$\begin{aligned} \sum_i \langle i|M_1 e^{-tH} M_2 e^{-(T-t)H}|i\rangle &= \sum_{i,j} \langle i|M_1 e^{-tH}|j\rangle\langle j|M_2 e^{-(T-t)H}|i\rangle \\ &= \sum_{i,j} e^{-tE_j-(T-t)E_i} \langle i|M_1|j\rangle\langle j|M_2|i\rangle \ . \end{aligned} \tag{3.6}$$

We are mainly interested in the energy of the lowest state $E_0$ which has a non-vanishing overlap with $M$. In the region where $0 \ll t \ll T$ the contributions of higher states are exponentially suppressed. If the overlap of the interpolating field with the hadron is sufficiently large, the sum (3.6) is dominated by terms with either $i$ the vacuum and $j$ a particle state or vice versa.

$$\begin{aligned} \langle M_1(\mathbf{p},t) M_2(\mathbf{p},0)\rangle \overset{0\ll t\ll T}{=} & e^{-tE_H}\langle 0|M_1|H(\mathbf{p})\rangle\langle H(\mathbf{p})|M_2|0\rangle \\ & + e^{-(T-t)E_{H'}}\langle H'(\mathbf{p})|M_1|0\rangle\langle 0|M_2|H'(\mathbf{p})\rangle + \ldots \end{aligned} \tag{3.7}$$

Here the vacuum energy is set to zero. The omitted terms in the series are suppressed by $\exp(-\Delta E t)$ with $\Delta E$ the energy difference between the ground state and the excited state. We are left with two contributions. The first describes

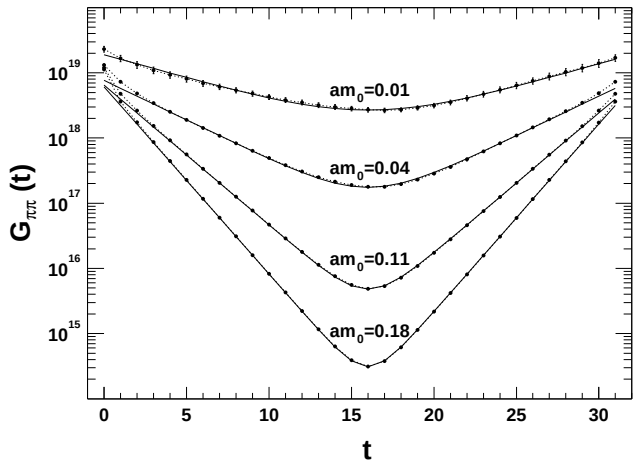


Figure 3.1: The two-point function for the pion $G_{\pi\pi}(t) = \langle \pi(t)\bar{\pi}(0)\rangle$ as a function of $t$ for four different bare quark masses. The pion source is at 0, the sink at $t$. The larger the quark mass, the heavier the pion and the steeper the curves. The dotted lines connect the points with equal quark mass to guide the eyes. The solid lines are the result of a cosh fit to the data in the region $t \in [6, 19]$. For small separations ($t$ small or large) the points deviate from the single cosh behavior. The data is taken from the $\beta_1 = 8.70$, $16^3 \times 32$ sample (see below).

a particle traveling forward in time direction from the source to the sink. In the second one, the particle travels around the torus backward in time to the sink. For mesons we can choose $M_2 = M_1^+$ such that the two have equal energy and we get

$$\langle M_1(\mathbf{p}, t) M_2(\mathbf{p}, 0)\rangle = 2e^{-\frac{1}{2}ET} |\langle 0|M|H(\mathbf{p}, t)\rangle|^2 \cosh(-(t - \frac{T}{2})E) + \dots \qquad (3.8)$$

with $E$ the energy of the meson $H(\mathbf{p})$. For states with zero spatial momentum $\mathbf{p} = 0$ the energy of the particle is equal to its mass $m$.

A realistic simulation for the pseudoscalar meson (pion) leads to two-point functions as shown in Fig. 3.1. The source is at $t_0 = 0$ and the position of the sink varies from $t = 0$ to $t = 31$. We can clearly see the cosh behavior in the center of the plot, where source and sink are well separated. The solid curves are fits of Eq. (3.8) to the data in the range $t \in [6, 25]$. If the separation of the sink and the source is small, we can see a deviation from the leading cosh. This is due to the contributions of excited states with the same quantum numbers as the pion. It is easy to show that the next contribution in Eq. (3.8) is another $\cosh[-(t - \frac{T}{2})m']$ with positive prefactor ($m'$ is the mass of the excited state).

## 3.2 Computation of fermionic matrix elements on the lattice

### 3.2.1 Mesons

In the previous section we described how to extract the masses of hadrons from two-point correlation functions of interpolating fields

$$\langle M(\mathbf{p},t)\bar{M}(\mathbf{p},0)\rangle \ . \tag{3.9}$$

The interpolating fields have in the case of the mesons the following generic form

$$M(\mathbf{p},t) = \sum_{\mathbf{x}} e^{-i\mathbf{x}\mathbf{p}}\Gamma_{\alpha\alpha'}F_{ff'}\bar{\psi}^{f,c}_{\alpha}(\mathbf{x},t)\psi^{f',c}_{\alpha'}(\mathbf{x},t) \tag{3.10}$$

$$\bar{M}(t,\mathbf{p}) = \sum_{\mathbf{x}} e^{i\mathbf{x}\mathbf{p}}\tilde{\Gamma}_{\alpha\alpha'}F^{+}_{ff'}\bar{\psi}^{f,c}_{\alpha}(\mathbf{x},t)\psi^{f',c}_{\alpha'}(\mathbf{x},t) \ . \tag{3.11}$$

We are mainly interested in the positively charged pseudoscalar and vector mesons which are identified in the light quark region with the $\pi^+$ and the $\rho^+$. For both of them the flavor structure is given by

$$F = \begin{pmatrix} 0 & 1 \\ 0 & 0 \end{pmatrix} \ . \tag{3.12}$$

We take $\Gamma = \tilde{\Gamma} = \gamma_5$ for the pion, the corresponding interpolating field will be abbreviated $P$ or $\pi$. The $\rho$ is a vector meson and the three vector components are generated by $\Gamma = \tilde{\Gamma} = \gamma_i$ with $i = 2, 3, 4$. Note that for these two

$$M^{+}(\mathbf{p},t) = \bar{M}(\mathbf{p},t) \ . \tag{3.13}$$

The task that remains is, thus, the computation of correlators of the following type

$$\langle \bar{\psi}^{f_1,\,c_1}_{\alpha_1}(x)\psi^{f_2,\,c_2}_{\alpha_2}(x)\bar{\psi}^{f_3,\,c_3}_{\alpha_3}(y)\psi^{f_4,\,c_4}_{\alpha_4}(y)\rangle \tag{3.14}$$

with $f_i$ the flavor, $c_i$ the color and $\alpha_i$ the Dirac indices.

Using the general formula Eq. (1.67) we can evaluate the $n$-point function of Eq. (3.14), again introducing multi-indices $a, \ldots, d$ that collect the color, Dirac, and flavor index.

$$\begin{aligned} &\left\langle \bar{\psi}_a(w)\psi_b(x)\bar{\psi}_c(y)\psi_d(z)\right\rangle \\ =&\left\langle \frac{\delta}{\delta J_a(w)}\frac{\delta}{\delta \bar{J}_b(x)}\frac{\delta}{\delta J_c(y)}\frac{\delta}{\delta \bar{J}_d(z)} e^{-\int \mathrm{d}^4x\mathrm{d}^4y \bar{J}D^{-1}(x,y)J(y)}\right\rangle_G\Big|_{\substack{J=0\\ \bar{J}=0}} \\ =&\left\langle D^{-1}_{d,c}(z;y)D^{-1}_{b,a}(x;w) - D^{-1}_{d,a}(z;w)D^{-1}_{b,c}(x;y)\right\rangle_G \end{aligned} \tag{3.15}$$

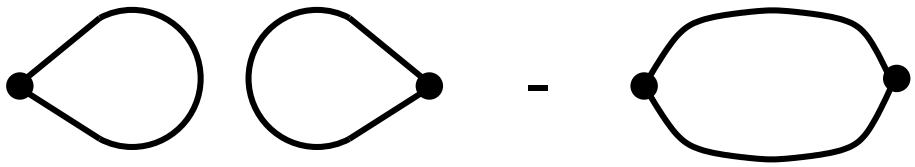

Figure 3.2: Graphical representation of the two contributions to the pion propagator. The points symbolize the pion source and sink. The lines stand for the full quark propagators.

From Eq. (3.15) we get the general meson two-point function

$$\begin{aligned}
&\Big\langle M(\mathbf{p},t)\bar{M}(\mathbf{p},0)\Big\rangle \\
&=\sum_{\mathbf{x},\mathbf{y}} e^{-i\mathbf{p}(x-y)}\mathrm{tr}\, F\mathrm{tr}\, F^{+}\Big\{\Big\langle \mathrm{tr}_{\,D,C}\left[D^{-1}(\mathbf{x},0;\mathbf{x},0)\Gamma\right]\mathrm{tr}_{\,D,C}\left[D^{-1}(\mathbf{y},t;\mathbf{y},t)\tilde{\Gamma}\right]\Big\rangle_{G} \\
&\quad -\mathrm{tr}\,(FF^{+})\Big\langle \mathrm{tr}_{\,D,C}\left[\Gamma D^{-1}(\mathbf{x},t;\mathbf{y},0)\tilde{\Gamma}D^{-1}(\mathbf{y},0;\mathbf{x},t)\right]\Big\rangle_{G}\Big\}
\end{aligned} \tag{3.16}$$

with $\mathrm{tr}_{\,D,C}$ denoting the trace over the Dirac and color indices. In this formula, we have two contributions visualized in Fig 3.2. On the left, the propagators are contracted with themselves. Such contributions are very difficult to evaluate. However, for the flavor non-diagonal mesons like the $\pi^+$ and the $\rho^+$, these contributions vanish as $\mathrm{tr}\, F = 0$. We are left with the contribution on the right.

To simplify the numerical computation of Eq. (3.16), we use the $\gamma_5$-hermiticity Eq. (1.34) of the Dirac operator which reads with all indices included

$$D^{-1}(x,\mu,c;y,\nu,c') = (\gamma_5)_{\nu,\nu'}D^{-1}(y,\mu',c';x,\nu',c)^{*}(\gamma_5)_{\mu',\mu}\ . \tag{3.17}$$

Using this one can transform the connected contribution to Eq. (3.16) into

$$\begin{aligned}
&\langle M(\mathbf{p},t)\bar{M}(\mathbf{p},0)\rangle \\
&=-\sum_{\mathbf{x},\mathbf{y}} e^{-i\mathbf{p}(\mathbf{x}-\mathbf{y})}\mathrm{tr}\,(FF^{+})\Big\langle \mathrm{tr}_{\,D,C}\left[\Gamma D^{-1}(\mathbf{x},t;\mathbf{y},0)\tilde{\Gamma}\gamma_5 D^{-1}(\mathbf{x},t;\mathbf{y},0)^{+}\gamma_5\right]\Big\rangle_{G}\ .
\end{aligned} \tag{3.18}$$

In this expression, the inverse of the Dirac operator occurs only with the arguments $(\mathbf{x},t;\mathbf{y},0)$. Thus, we need the projections of the propagator onto quark fields on the time-slices 0 and $t$. We label the source and the sink by the position of the quark and introduce the notation $S^{(\mathbf{x},t,\alpha,c)}(y,t,\beta,d)$ for a quark field centered at $\mathbf{x}$ on time-slice $t$ with Dirac and color indices $\alpha$ and $c$ respectively. These denote a vector which has itself a space-time, Dirac, and color index. It has

support only on time-slice $t$. Hence, we are interested in the following product

$$\sum_{\substack{\mathbf{y},\beta,d \\ \mathbf{y}',\beta',d'}} S^{(\mathbf{x},t,\alpha,c)}(\mathbf{y},t,\beta,d)^* D^{-1}(\mathbf{y},t,\beta,d;\mathbf{y}',0,\beta',d') S^{(\mathbf{x}',0,\alpha',c')}(\mathbf{y}',0,\beta',d') \quad (3.19)$$

The input of our calculation are twelve vectors each containing a source located at, e.g., $\mathbf{x} = \mathbf{0}$ and one combination of the Dirac and color label. For these we solve the following system of linear equations for $T^{(\mathbf{x},0,\alpha,c)}$

$$\sum_{\mathbf{y}',t,\beta',c'} D(\mathbf{y},0,\beta,d;\mathbf{y}',t,\beta',d') T^{(\mathbf{x},0,\alpha,c)}(\mathbf{y}',t,\beta',d') = S^{(\mathbf{x},0,\alpha,c)}(y,0,\beta,d) \quad (3.20)$$

We have to fold the result of this inversion $T^{(\mathbf{x},0,\alpha,c)}$ with the sink on time-slice $t$ and obtain in this way the desired component of the propagator.

### 3.2.2 Baryons

Baryons, e.g., the proton, have three valence quarks and half integer spin. For the proton we take the following interpolating fields for the source $B$ and the sink $\bar{B}$ with spatial momentum $\mathbf{p}$ on time-slice $t$ [G+96b]

$$B_\alpha(\mathbf{p},t) = \sum_{\mathbf{x}} \mathrm{e}^{\mathrm{i}\mathbf{p}\cdot\mathbf{x}} \epsilon_{ijk} u^i_\alpha(\mathbf{x},t) u^j_\beta(\mathbf{x},t) \hat{C}_{\beta\gamma} d^k_\gamma(\mathbf{x},t) \quad (3.21)$$

$$\bar{B}_\alpha(\mathbf{p},t) = \sum_{\mathbf{x}} \mathrm{e}^{-\mathrm{i}\mathbf{p}\cdot\mathbf{x}} \epsilon_{ijk} \bar{d}^i_\beta(\mathbf{x},t) \hat{C}_{\beta\gamma} \bar{u}^j_\gamma(\mathbf{x},t) \bar{u}^k_\alpha(\mathbf{x},t) \quad (3.22)$$

with $\hat{C} = C\gamma_5$ or $\hat{C} = C\gamma_5 \cdot \frac{1}{2}(1+\gamma_4)$ and $C$ the charge conjugation matrix defined in Eq. (A.9). $u$ and $d$ denote the quark fields of the respective flavors.

We can now compute the baryon two-point function in an analogous manner as for the mesons. As the source consists of quark fields only and the anti-quark fields are in the sink, we do not need the transposition trick Eq. (3.17). One gets straightforwardly

$$\begin{aligned}
&\langle B(\mathbf{p},t)\bar{B}(\mathbf{p},0)\rangle = \\
&\quad \sum_{\mathbf{x}} \sum_{\mathbf{y}} e^{-(\mathbf{x}-\mathbf{y})\cdot\mathbf{p}} \epsilon_{cde}\epsilon_{fgh} \hat{C}_{\beta\gamma}\hat{C}_{\rho\tau} \frac{1}{2}[1+\gamma_4]_{\delta\alpha} \times \\
&\qquad \Big\langle D^{-1}(\mathbf{x},t;\mathbf{y},0)_{\alpha,c;\delta,f} D^{-1}(\mathbf{x},t;\mathbf{y},0)_{\beta,d;\tau,h} D^{-1}(\mathbf{x},t;\mathbf{y},0)_{\gamma,e;\rho,g} \\
&\qquad -D^{-1}(\mathbf{x},t;\mathbf{y},0)_{\alpha,c;\tau,h} D^{-1}(\mathbf{x},t;\mathbf{y},0)_{\beta,d;\delta,f} D^{-1}(\mathbf{x},t;\mathbf{y},0)_{\gamma,e;\rho,g} \Big\rangle_G
\end{aligned} \quad (3.23)$$

where $\langle\cdots\rangle_G$ denotes, again, the average over the gauge fields. One of the sums over the volume is trivial due to the translation invariance of the theory. The resulting two-point function is not symmetric with respect to $t \to T - t$, see Fig. 3.3 for the nucleon. The mass of the nucleon can be extracted from the left branch. The right branch corresponds to the parity partner of the nucleon, the $N^*$.

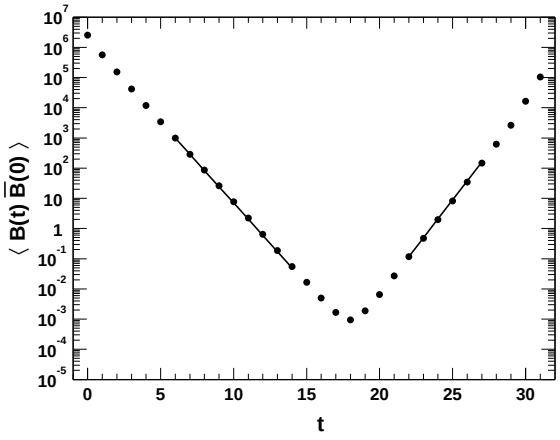


Figure 3.3: The two-point function for the nucleon. The slope of the left branch gives the nucleon mass whereas we extract the mass of its parity partner from the right branch ($\beta_1 = 8.35$ on $16^3 \times 32$, $m_0 = 0.18$).

### 3.2.3 Smearing of the quark fields

To get a good overlap with the physical hadron, it is not advisable to use point-like quark sources

$$S_p^{(x',t',\alpha',c')}(\mathbf{x},t,\alpha,c) = \delta_{t,t'}\delta_{\mathbf{x},\mathbf{x}'}\delta_{\alpha,\alpha'}\delta_{c,c'} \ . \tag{3.24}$$

Because physical hadrons are not point-like themselves, the suppression of excited states is weak for a point source. A prescription to generate extended quark fields has to respect the gauge invariance of the theory. Basically, there are two possibilities to achieve this:

- **Gauge fixing**
  The gauge is fixed by some concrete prescription, e.g., to Coulomb gauge. This is a modification of the gauge fields, but the final observables do not depend on it. As the gauge freedom is removed from the theory, gauge transformations are no issue any longer. With a fixed gauge, frequently, simple Gaussians are used to describe the smeared fields.

  $$S^{(x',t',\alpha',c')}(\mathbf{x},t,\alpha,c) = \delta_{t,t'}e^{-|\mathbf{x}-\mathbf{x}'|^2/2\sigma^2}\delta_{\alpha,\alpha'}\delta_{c,c'} \tag{3.25}$$

  The width $\sigma$ is chosen such that it fits well into the physical hadron.

- **Smearing**
  Another possibility [UKQCD93, AGJ$^+$94, B$^+$97] is to define a kernel $H$

that generates from a localized point-source $S_p$ as in Eq. (3.24) a smeared quark field with the correct gauge transformation properties. This requires the kernel to incorporate information about the gauge field $U$.

$$S^{(x',t',\alpha',c')}(\mathbf{x},t,\alpha,c) = \sum_{\tilde{\mathbf{x}},\tilde{\alpha},\tilde{c}} H(\mathbf{x},\alpha,c;\tilde{\mathbf{x}},\tilde{\alpha},\tilde{c};t,U) S_p^{(\mathbf{x}',t,\alpha',c')}(\tilde{\mathbf{x}},t,\tilde{\alpha},\tilde{c}) \tag{3.26}$$

We decided to use smearing, in particular the Jacobi method described in Ref. [B$^+$97]. One defines a kernel $K$ which is diagonal in spin space and depends on space-time and color only through the gauge fields.

$$K(\mathbf{x}',\alpha',c';\mathbf{x},\alpha,c) = \delta_{\alpha',\alpha} \sum_{\mu=2}^{4} \left[ U_\mu(\mathbf{x}',t)_{c',c}\ \delta_{\mathbf{x}'-\hat{\mu},\mathbf{x}} + U_\mu^+(\mathbf{x}'-\hat{\mu},t)_{c',c}\ \delta_{\mathbf{x}'-\hat{\mu},\mathbf{x}} \right] \tag{3.27}$$

The smeared source $S$ on a time-slice $t$ centered at $\mathbf{x}$ is constructed iteratively by applying $\kappa K$ on the vector.

$$S^{(t,\mathbf{x},\alpha,c)} = \left( \sum_{n=0}^{N} \kappa^n K^n \right) S_p^{(t,\mathbf{x},\alpha,c)} \tag{3.28}$$

The parameter $\kappa$ controls the strength of the smearing in each step. The iteration starts from a point source $S_p^{(\mathbf{x},t,\alpha,c)}$. As $K$ only connects nearest neighbor sites, the source is broadened a bit in each iteration step. The parameter $\kappa$ is chosen such that the series does not converge. The size of the source is controlled by the number of iterations $N$ and measured by $r$, which is defined as

$$r^2 = \frac{\sum_{\mathbf{y}} \mathbf{y}^2 S^{(\mathbf{x},t,\beta,d)}(\mathbf{y},t,\alpha,c)^* S^{(\mathbf{x},t,\beta,d)}(\mathbf{y},t,\alpha,c)}{\sum_{\mathbf{y}} S^{(\mathbf{x},t,\beta,d)}(\mathbf{y},t,\alpha,c)^* S^{(\mathbf{x},t,\beta,d)}(\mathbf{y},t,\alpha,c)} \ . \tag{3.29}$$

We set $\kappa = 0.21$ as in [B$^+$97] and adjust $N$ such that $ar \approx 0.35\,\mathrm{fm}$ (compare with the proton charge radius of $\approx 0.85$ fm).

It is easy to see that $H$ is hermitian. Thus, folding with the smeared sink amounts to smearing each time-slice of the propagator $T$ from Eq. (3.20) by the same procedure as the source.

### 3.2.4 The inversion

In our applications we are interested in the physical quantities as a function of the quark mass. The major reason is that, due to limited computer resources, we cannot simulate at the physical value of the pion mass (which determines the appropriate value of the bare quark mass parameter). This has several reasons. First, the numerical cost to solve the linear system of equations

$$D_m t \equiv [(1 - \frac{1}{2}am)D + m]t = s \Longleftrightarrow [D + \tilde{m}]t = \tilde{s} \tag{3.30}$$

with $s$ the quark source and $\tilde{m} = m/(1 - am/2)$, grows with the smallest eigenvalue of $D_m$. For exact Ginsparg-Wilson operators this is given by $\tilde{m}$. For approximate solutions, the eigenvalues can fluctuate to the left of the Ginsparg-Wilson circle and therefore limit the smallest accessible $m$ (such that all eigenvalues have a positive real part). Furthermore, for light quark masses, the finite lattice size effects get more severe. Therefore, one computes the observable at several values of $m$ and tries to extrapolate to the *chiral limit* $am \to 0$. The way in which to perform this limit has to be decided upon for each observable individually.

The solution of the linear system of equations (3.30) is a numerically expensive task. For a $16^3 \times 32$ lattice $(D + \tilde{m})$ is a $N \times N$ matrix with $N = 16^3 \cdot 32 \cdot 4 \cdot 3 = 1572864$. However, the numerical effort of the inversion is determined by the structure of the matrix. Wilson fermions have only nearest neighbor coupling, so the matrix is sparse and the numerical effort is relatively low. Because there is no ultra-local solution to the Ginsparg-Wilson equation [Hor99], the numerical cost is significantly larger for chiral fermions (however, locality ensures that the entries decrease exponentially with growing distance). A compromise between these two extremes is the chirally improved operator. It has support on the whole hypercube and an additional L-shaped term. There is no entry with distance larger than $\sqrt{5}a$.

We use a Krylov space method for the inversion, namely the Bi-Conjugate Gradient stabilized algorithm [vdV92], which is commonly abbreviated *Bi-CG-stab*. To solve the linear system of equations (3.30) for a set of quark masses simultaneously, the so-called multi-mass solvers are employed [FNG$^+$95, Jeg96]. These rely on the fact that all Krylov space solvers are based on multiplications of the matrix $(D+\tilde{m})$ on a specific test vector $v_i$. It costs almost no extra computer time to compute $(D + \tilde{m})v_i$ for several masses as it amounts only to adding $mv_i$ to the result. The extra cost is only in some extra scalar products and in extra memory. But as the largest portion of computer time is used in the matrix on vector multiplications, this extra cost is negligible.

## 3.3 Hadron spectroscopy with the chirally improved Dirac operator

In this section, first results of the chirally improved Dirac operator, which can be compared with experimental data, are presented. We compute the masses of the light mesons, i.e., the pseudoscalar (pion) and the vector (rho) meson for different lattice sizes and meson momenta. The pion mass is of special interest. Due to the Gell-Mann–Oakes–Renner relation Eq. (1.31) it should go to zero as the quark mass vanishes. This is a crucial test for the chiral properties of a Dirac operator. We analyze the logarithmic corrections that arise in quenched QCD, too. Furthermore, we present results for the nucleon mass and the dispersion

| | $\beta_1 = 7.90$ | | $\beta_1 = 8.35$ | | $\beta_1 = 8.70$ | |
|---|---|---|---|---|---|---|
| $a$ [fm] | 0.148 | | 0.102 | | 0.078 | |
| | $N$ | $L$ [fm] | $N$ | $L$ [fm] | $N$ | $L$ [fm] |
| $8^3 \times 24$ | 200 | 1.2 | — | 0.8 | — | 0.6 |
| $12^3 \times 24$ | 100 | 1.8 | 100 | 1.2 | — | 0.9 |
| $16^3 \times 32$ | 100 | 2.4 | 100 | 1.6 | 100 | 1.2 |

Table 3.1: Overview of the number of configurations $N$ used for the hadron spectroscopy. The lattice spacing $a$ as computed from Eq. (1.27) and the resulting spatial extend $L$ are listed, too.

relations of the various particles. After that we study the scaling behavior of the chirally improved operator by comparing the hadron masses for different lattice spacings but constant physical volume. For a similar analysis with the parameterized fixed point operator see Ref. [Hau02].

### 3.3.1 Technical details

We use gauge configurations generated with the Lüscher-Weisz action (Sec. 1.4.2) at three different values of the gauge coupling $\beta_1 = 7.90$, 8.35 and 8.70 on $8^3 \times 24$, $12^3 \times 24$ and $16^3 \times 32$ lattices. An overview of the collected statistics is given in Table 3.1. The lattice sizes are chosen such that the diagonal elements correspond to constant physical volume in order to study discretization effects. The columns correspond to constant lattice spacing but different spatial extend which allows to study finite size effects.

We use the chirally improved Dirac operator as described in Sec. 1.6.5 with the coefficients for the different gauge couplings given in Appendix B. To study the dependence on the quark mass parameter, we compute a set of columns of the propagator $D_m^{-1}$ with several values for $m$. This can be done easily with the multi mass algorithm (Sec. 3.2.4).

In the next section we discuss the results of our calculations. The numerical values are collected in Tables 3.2 to 3.7 at the end of the chapter.

### 3.3.2 Results

#### The mass of the pseudoscalar meson

We use the interpolating fields Eq. (3.3) to extract the mass of the pseudoscalar meson. These lead to the pseudoscalar-pseudoscalar two-point function $G_{PP}$. In the region of light quarks, this particle is identified with the pion. Unfortunately, this correlator has systematic problems for light quark masses. We get not only

contributions from the two quarks traveling directly from the source to the sink. There are additional contributions from quarks going around the spatial periodic boundary conditions in a topologically non-trivial way. As a rule of thumb, on a finite lattice with spatial extend $L/a$ and a pion mass $am_{\rm PS}$, the product $Lm_{\rm PS}$ should not be smaller than 4. This is the reason why we haven't done simulations for all combinations of $\beta_1$ and the lattice size; the physical size of the particle has to fit inside the box, too.

Furthermore, we get contributions from the chiral logarithms that are believed to arise in quenched QCD. Contrary to the linear behavior of $m_{\rm PS}^2$ as a function of $m_q$ predicted by the Gell-Mann–Oakes–Renner relation Eq. (1.31), there is an additional logarithmic term in the quenched theory [Mor87, Sha90, BG92]

$$m_{\rm PS}^2 = 2Am_q \left[1 - \delta \left(\ln \frac{2Am_q}{\Lambda^2} + 1\right)\right] + 4Bm_q^2 \; . \tag{3.31}$$

There have been several attempts in the last years to determine the parameter $\delta$ [JLQCD97, QCDSF00, BDET00, DDH$^+$02b, DDH$^+$02a, CH02, CP-PACS02, Hau02, D$^+$02b]. The results scatter in the range between 0.05 and 0.48. The first results with Wilson or Kogut-Susskind quarks were in the region of 0.1, whereas the results with quarks of better chirality led to higher values in the region of 0.2. We present our result for $\delta$ below.

A third source of trouble are finite volume effects due to zero modes of the Dirac operator. They don't contribute in full QCD due to the vanishing fermion determinant. However, the contribution of these modes can be removed [B$^+$00, GHR01, D$^+$02a] from the pseudoscalar-pseudoscalar two-point function $G_{PP}$ (with $\Gamma = \gamma_5$) by subtracting the scalar-scalar two-point function $G_{SS}$ with $\Gamma = \mathbf{1}$ in Eq. (3.18)

$$G_{PP-SS} = G_{PP} - G_{SS} \; . \tag{3.32}$$

The effect of this is easily understood in the spectral decomposition of the propagator in which Eq. (3.18) becomes for $\Gamma = \gamma_5$

$$\langle \pi(t)\bar{\pi}(0)\rangle = \Big\langle \sum_{\lambda,\lambda'} \frac{\bar{\psi}_\lambda^+(t)\psi_{\lambda'}(t)\bar{\psi}_{\lambda'}^+(0)\psi_\lambda(0)}{(-i\lambda+m)(i\lambda'+m)} \Big\rangle \tag{3.33}$$

with $\psi_\lambda$ the eigenvector of the Dirac operator with eigenvalue $i\lambda$. One uses the fact that the zero modes are eigenvectors of $\gamma_5$ with eigenvalue $\pm$ 1. For $\lambda' = 0$ its contribution to Eq. (3.33) can be rewritten as

$$\Big\langle \sum_{\lambda} \frac{\bar{\psi}_\lambda^+(t)\gamma_5\psi_{\lambda'}(t)\bar{\psi}_{\lambda'}^+(0)\gamma_5\psi_\lambda(0)}{(-i\lambda+m)(i\lambda'+m)} \Big\rangle \; , \tag{3.34}$$

which in turn is equal to its contribution to the scalar-scalar correlation function ($\Gamma = \mathbf{1}$)

$$\langle S(t)\bar{S}(0)\rangle = \Big\langle \sum_{\lambda,\lambda'} \frac{\bar{\psi}_\lambda^+(t)\gamma_5\psi_{\lambda'}(t)\bar{\psi}_{\lambda'}^+(0)\gamma_5\psi_\lambda(0)}{(-i\lambda+m)(i\lambda'+m)} \Big\rangle \; . \tag{3.35}$$

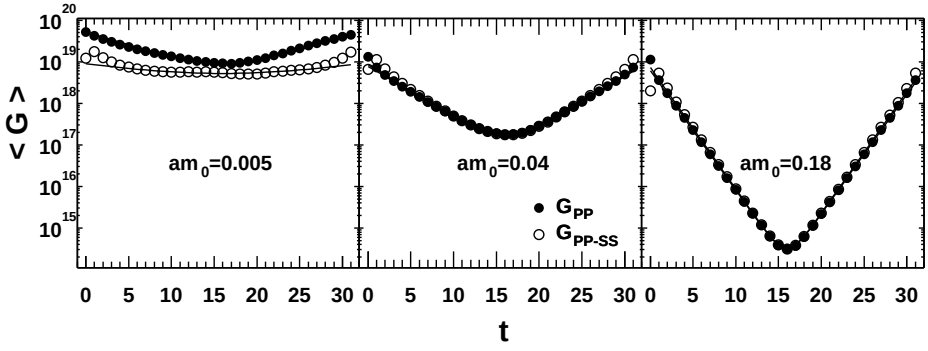


Figure 3.4: The two-point function for the pion ($\Gamma = \gamma_5$, full dots) and the subtracted $G_{PP-SS}$ (open dots) of Eq. (3.32) for three different values of the quark mass parameter $am_0$. It is taken from the $\beta_1 = 8.70$ , $16^3 \times 32$ sample. The solid lines are the result of the cosh fit.

In this way, the effects of the zero modes can be removed at the cost of an additional heavy particle visible in the short time behavior of the propagator. However, as we use an approximate solution to the Ginsparg-Wilson equation, the eigenvalues of $\gamma_5$ are not $\pm 1$ but rather $\approx \pm 0.85$. The cancelation is not perfect. We attempt the subtraction and see an improvement in the chiral limit. We remark that the subtraction is possible only for small quark masses. For heavy quarks, the mass of the scalar and the pseudoscalar particle get closer and the separation of the two becomes very difficult.

As an example for the propagators, we plot in Fig. 3.4 the $G_{PP}$ and $G_{PP-SS}$ two-point functions on a $16^3 \times 32$ lattice with $\beta_1 = 8.70$. The quark mass increases from left to right. The effect of the of the subtraction is largest for the smallest quark mass. As the scalar particle is heavier, we see a larger deviation from the cosh fit for the subtracted two-point function than for the unsubtracted one.

The square of the extracted masses for $\beta_1 = 8.70$ and $\beta_1 = 7.90$ is shown in Fig. 3.5. We observe that for $\beta_1 = 8.70$ the $PP - SS$ two-point function really extrapolates linearly to 0 whereas $PP$ bends up. Because the lattice volume is larger for $\beta_1 = 7.90$ than for 8.70 (about a factor of 2 for each side), the effect subtraction is less pronounced.

Let us finally remark that we can simulate at values of $m_{\rm PS}/m_{\rm V}$ down to 0.3 without facing the problem of exceptional configurations ($m_{\rm V}$ is the mass of the vector meson). This means that the spectrum of the Dirac operator is well enough

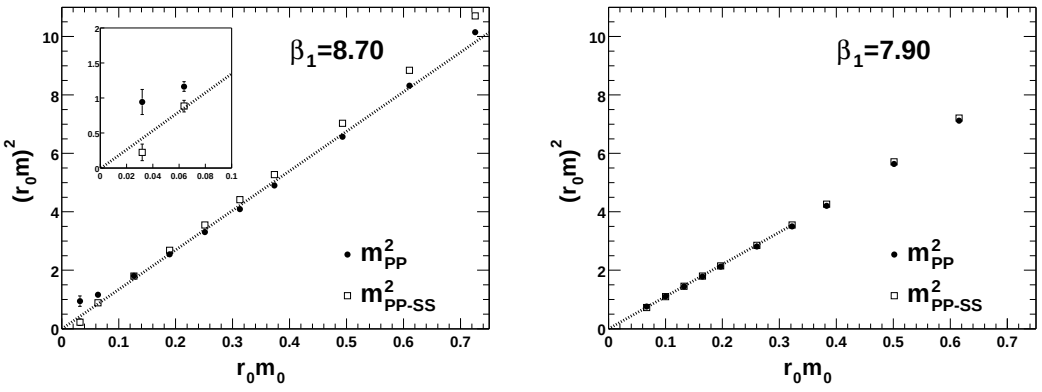


Figure 3.5: The extracted masses for the $G_{PP}$ and $G_{PP-SS}$ for $\beta_1 = 8.70$ (left) and $\beta_1 = 7.90$ (right). For the smaller volume (left) the $PP$ correlator bends up for $r_0 m_0 \to 0$. The line is a result for the fit to a mixed data set which consists of the the $PP - SS$ mass as long as it is smaller and $r_0 m < 0.4$. Its intercept is compatible with 0 within the errorbar.

ordered at the origin such that we do not get zero or negative eigenvalues. For the Wilson operator there is a significant amount of exceptional configurations even at $m_{\rm PS}/m_{\rm V} = 0.4$.

### The quenched chiral logarithm

The coefficient $\delta$ of the quenched chiral logarithm in Eq. (3.31) is of special interest. Chiral perturbation theory predicts a value of $\approx 0.2$ and a confirmation from the lattice would strengthen the believe in this theory. We want to extract $\delta$ from the dependence of the mass of the pseudo-scalar meson on the quark mass. However, on the lattice there are several sources of systematic errors in particular in the region of small quark masses. We have to use a proper definition of, both, the quark mass and the pion mass such that they vanish in the same point as predicted by Eq. (3.31).

As we only have an approximate solution of the Ginsparg-Wilson equation, we have an additive renormalization of the bare quark mass. Therefore, we use the bare axial-vector Ward identity (AWI) quark mass $m^{\rm AWI}$ in the following. It is defined by

$$2m^{\rm AWI} = \frac{\langle P^-(0)\partial_t A_t^+(\mathbf{p}=0,t)\rangle}{\langle P^-(0)P^+(\mathbf{p}=0,t)\rangle} \tag{3.36}$$

with $P$ the pseudo-scalar density and $A_t$ the time component of the axial-vector current. The + and the − give the relevant flavor combinations, e.g., $P^\pm = P^u \pm iP^d$. The plateaus in $t$ are very flat for this ratio and the resulting errorbars

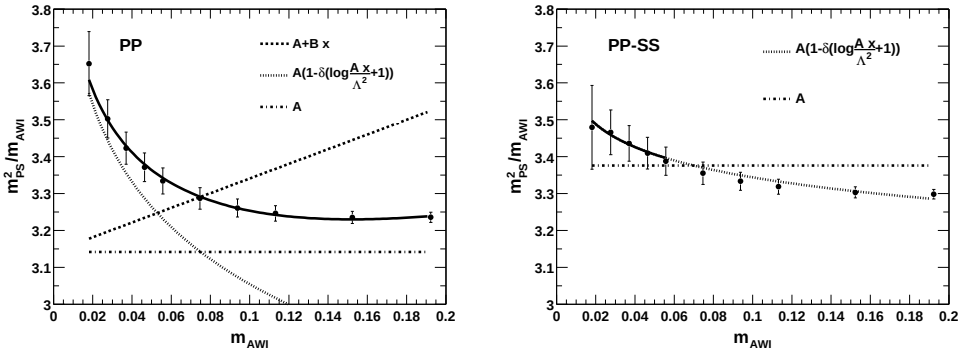


Figure 3.6: The mass of the pseudoscalar meson divided by quark mass $m^{\mathrm{AWI}}$ as a function of $m^{\mathrm{AWI}}$ for $\beta_1 = 7.90$ on the $16^3 \times 32$ lattice. The left plot is $m_{\mathrm{PS}}$ from the $PP$ correlator, the right plot is form the $PP-SS$ correlator alone. The solid curve correspond to fits to the data plotted. For the $PP$ data Eq. (3.31) was fitted to the full set, for the $PP - SS$ data we fitted to the smallest quark masses with $B \equiv 0$.

are small. It is, thus, a very convenient definition of the quark mass. However, for the physical quantity, this quark mass has to be renormalized. But we can redefine the constants $A$ and $B$ in Eq. (3.31) such, that the renormalization constants cancel.

We already discussed that the chiral limit of the $m_{\mathrm{PS}}$ is spoiled by the effect of the zero modes. In order to remove them, one can either try to mix the $PP$ with the $PP - SS$ data or stick to the smallest quark masses and use the $PP - SS$ data alone. However, one has to keep in mind, that this is not the only finite size effect in the region of light quarks and, thus, we should treat differences due to the subtraction as an estimate for possible other systematic errors.

The results of the two procedures are shown in Fig. 3.6. For the $PP$ data we fitted Eq. (3.31) to the data and plotted the curve together with the individual contributions ($\delta = 0.10$, $A = 3.1$, $B = 2.0$), see Fig. 3.6. We observe that the large logarithm is to a large extend compensated by the quadratic term. The logarithmic and the quadratic term seem unnaturally big in the regions where they are expected to be relevant (for small and large masses, respectively). The situation is different for the $PP - SS$ data set. There we fitted in the range $m^{\mathrm{AWI}} < 0.06$ and obtained $\delta \approx 0.03$. However, the curve describes the data quite well for larger quark masses. The discrepancy between the two results should be taken as a warning. The finite size effect changes the result drastically, even though the subtraction of the zero modes is not perfect as the eigenvalue of $\gamma_5$ is not $\pm 1$. Other finite size effects, e.g., from the size of the wave function or non-trivial winding of the quarks around the torus are not considered, yet.

Another method to extract the $\delta$ parameter is to look at the mass of the pseudoscalar meson $m_{\mathrm{PS}}$ with quarks of different masses $m_1$ and $m_2$. Quenched chiral perturbation theory predicts for this mass

$$\begin{aligned} m_{\mathrm{PS},12}^2 =& A(m_1+m_2)\Big\{1-\delta\big[\ln\frac{2m_1A}{\Lambda_\chi^2}+\frac{m_2}{m_2-m_1}\ln\frac{m_2}{m_1}\big] \\ &+\frac{\alpha_X}{A}\big[m_1\ln\frac{2m_1A}{\Lambda_\chi^2}+m_2\ln\frac{2m_2A}{\Lambda_\chi^2}+\frac{m_1m_2}{m_2-m_1}\ln\frac{m_2}{m_1}\big]\Big\} \\ &+B(m_1+m_2)^2+\mathcal{O}(m^3,\delta^2) \end{aligned} \tag{3.37}$$

with $A$, $B$, $\delta$ and $\alpha_X$ a priori unknown constants. The arbitrary scale $\Lambda_\chi$ is of the order 1 GeV. For $m_1 = m_2$ and $\alpha_X = 0$ this expression reduces to Eq. (3.31). In order to remove the constants $A$, $B$ and $\Lambda_\chi$ the following cross ratio $y$ was proposed [CP-PACS02]:

$$y = \frac{2m_1}{m_1+m_2}\frac{m_{\mathrm{PS},12}^2}{m_{\mathrm{PS},11}^2}\frac{2m_2}{m_1+m_2}\frac{m_{\mathrm{PS},12}^2}{m_{\mathrm{PS},22}^2}\ . \tag{3.38}$$

For small $\delta$, $\alpha_X$ and small quark masses this is expected to behave like

$$y = 1+\delta x+\alpha_X z+\mathcal{O}(m^2,\delta^2) \tag{3.39}$$

with

$$x = 2+\frac{m_1+m_2}{m_1-m_2}\ln\left(\frac{m_2}{m_1}\right) \tag{3.40}$$

$$z = \frac{1}{A}\left(\frac{2m_1m_2}{m_2-m_1}\ln\frac{m_2}{m_1}-m_1-m_2\right) \tag{3.41}$$

as long as the quark masses are not too small such that the logarithms in the square brackets in Eq. (3.37) are not large. As $z$ is of higher order in the quark mass, the leading behavior of $y$ should be linear in $x$ with slope $\delta$. For $m_1 = m_2$ we get $x = 0$. Large ratios of $m_1/m_2$ lead to values of $x$ further away from zero.

It remains to decide, which pseudoscalar mass to use. Even though the physical volume is large, the subtraction makes a difference ($\mathcal{O}(5\%)$) for the small quark masses. We follow the two preceding investigations and use the $PP$ masses. The resulting plot is shown in Fig. 3.7. We find a linear behavior and extract $\delta \approx 0.18(3)$, which is compatible with Hauswirth's extraction [Hau02]. Further questions arise: How can we judge the quality of the extraction this kind of plot? What is the effect of finite size effects? In which range should we use Eq. (3.37)?

To clarify these questions, we have plotted $m_{\mathrm{PS}}^2/(m_1^{\mathrm{AWI}}+m_2^{\mathrm{AWI}})$ as a function of $(m_1^{\mathrm{AWI}}+m_2^{\mathrm{AWI}})$ for the complete non-diagonal data set at $\beta_1 = 7.9$ in Fig. 3.8. The first observation is that up to $(m_1^{\mathrm{AWI}}+m_2^{\mathrm{AWI}}) \approx 0.1$ all data points lie on one curve; the deviations for larger quark masses are below one standard

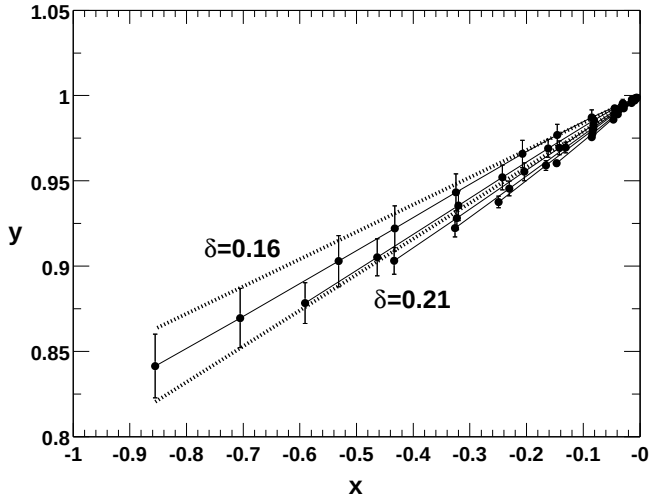


Figure 3.7: The $xy$-plot for $\beta_1 = 7.90$ on the $16^3 \times 32$ lattice. The points are connected with solid lines for the smaller quark mass fixed; the longer this line the smaller is this fixed mass. The dotted lines correspond to $1 + \delta x$ for two values of $\delta$.

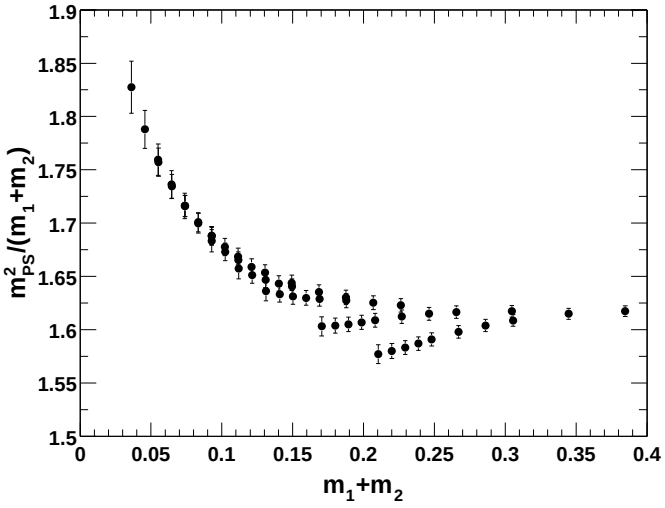


Figure 3.8: The mass of the pseudoscalar meson divided by the sum of the valence quark masses as a function of this sum for $\beta_1 = 7.90$ on the $16^3 \times 32$ lattice. The values lie on a common line up to $m_1 + m_2 \approx 0.15$.

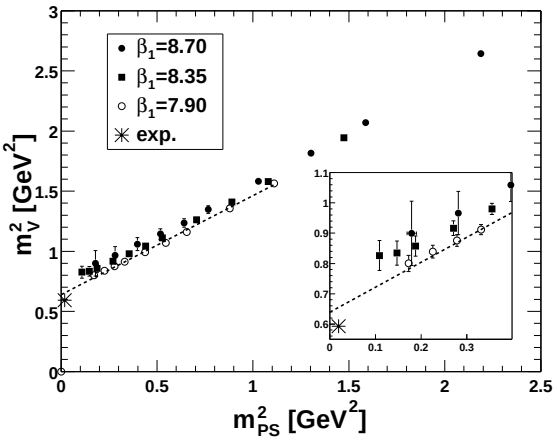


Figure 3.9: $m_{\mathrm{V}}^2$ as a function of $m_{\mathrm{PS}}^2$ for the three values of $\beta_1$ on the $16^3 \times 32$ lattices. $a$ is set by the Sommer parameter $r_0$. The dotted line corresponds to a fit to the $\beta_1 = 7.90$ data.

deviation. Thus it seems questionable that there is additional information in the non-diagonal data compared to the mass degenerate case. Furthermore, the conclusion for the diagonal case, i.e. that the $\delta$ is mainly a finite size effect, holds for the non-diagonal mesons too; even though the lines in the $xy$-plot are straight.

All these values for $\delta$ aren't meant to be the final answer. We have listed them to visualize the large systematic uncertainties in the extraction for $\delta$. We see that the effect of the subtraction of the zero modes is large even in our largest volume. Hence, it seems not possible to control the systematic errors, in particular those from the effect of the zero modes and other finite size effects.

### The mass of the vector meson

The lightest meson, which can be compared with the particle data book, is the vector meson that is identified with the $\rho$ in the limit of light quarks. It is generated by $\Gamma = \gamma_i$ with $i = 1, 2, 3$. We extract the mass of each of the components on jackknife subensembles, then average over the three components and calculate the jackknife error for it. The result is given in Fig. 3.9, where the scale is set by the Sommer parameter $r_0 = 0.5$ fm calculated from the interpolating function Eq. (1.27). The square of the vector mesons mass is plotted as a function of $m_{\mathrm{PS}}^2$ for the three values of $\beta_1$ on the $16^3 \times 32$ lattices. Each data set shows little deviation from a straight line and the three sets coincide sufficiently well. A fitted linear function through all points of the $\beta_1 = 7.90$ sample extrapolates these values to 830 MeV. This is 8% larger than the value in the particle data book of 770 MeV. However one has to keep in mind the various uncertainties. On top

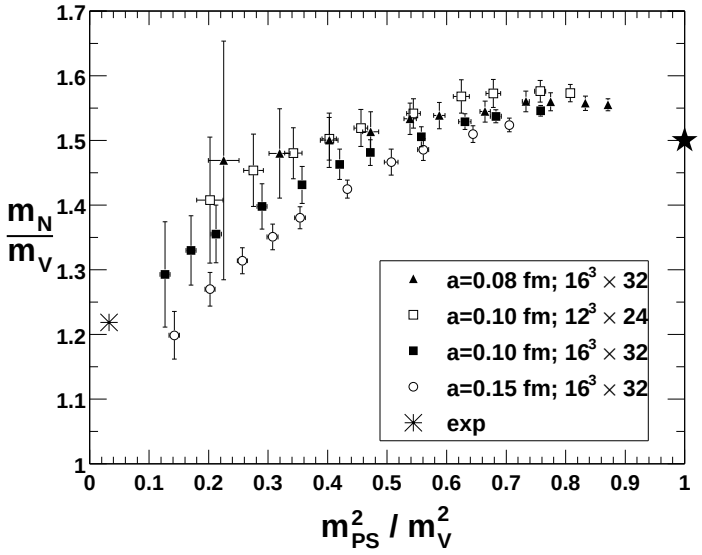


Figure 3.10: The APE plot for the three values of $\beta_1$. The experimental value is plotted as a burst, the heavy quark limit is given by the star.

of the statistical error we use the quenched approximation without a continuum extrapolation and there is certainly an error in the value of $r_0 = 0.5$ fm. This in mind, the result is sufficiently accurate.

### The proton and its parity partner

The dependence of the nucleon mass $m_N$ on the pseudoscalar meson mass is often presented in a so-called APE plot. There, the ratio of the nucleon mass to the vector meson mass is plotted as a function of $(m_{\rm PS}/m_{\rm V})^2$. In this way the lattice constant cancels and it is easy to compare the results for different $\beta_1$. If the same ratio is plotted against $(m_{\rm PS}/m_{\rm V})$ it is called an Edinburgh plot.

We show the APE plot for the nucleon mass $m_N$ in Fig. 3.10. The ratio $m_N/m_V$ is given for the three different values of $\beta_1$ on the large lattices together with the results on $12^2 \times 24$ at $\beta = 8.35$. The experimental value is marked with the burst at $(m_\pi/m_\rho)^2 = 0.033$ and $m_p/m_\rho = 1.22$. The other known point is in the heavy quark limit, where the masses of the particles are given entirely by the quark masses. The mesons have two and the baryons three valence quarks which leads to $m_{\rm PS}/m_{\rm V} = 1$ and $m_N/m_{\rm V} = 1.5$. The three values of $\beta_1$ suffer from different problems, in particular at small pion masses. The small $\beta_1$ has $a = 0.15$ fm. Thus there might be larger discretization effects; we will turn to this question in Sec. 3.3.3. On the other hand, the ensemble with $\beta_1 = 8.70$

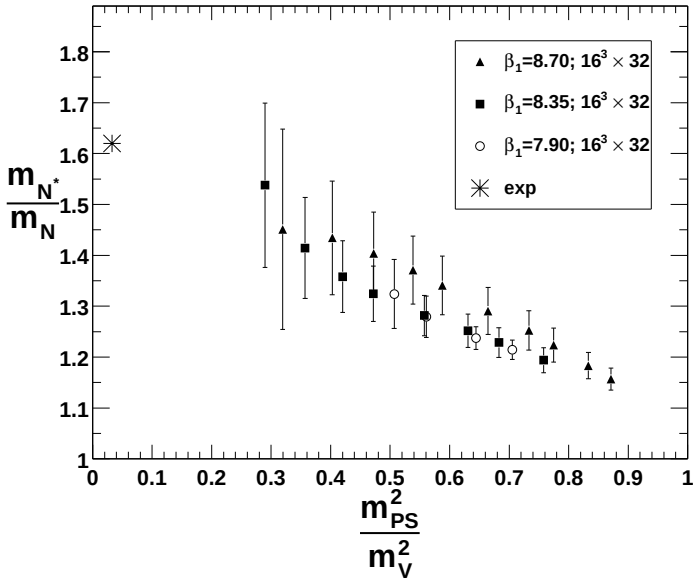


Figure 3.11: The ratio of the $N^*$ mass to the proton mass as a function of $(m_{\rm PS}/m_{\rm V})^2$. The experimental value of 1.62 is given by the burst. The data has been extracted on the larger lattices for all values of $\beta_1$.

has a relatively small lattice. The particle hardly fits into the box and the wave function is heavily distorted. Smaller volume leads to larger $m_N/m_V$. This can be seen by comparing the $12^3 \times 32$ and the $16^3 \times 32$ lattices at $\beta_1 = 8.35$.

It is interesting to look at the mass of the parity partner of the proton, the $N^*$. Whereas the nucleon mass is given by the exponential decay for $t \ll T$, the mass of the $N^*$ is given by the slope in the region $T > t \gg 0$, see Fig. 3.3. We have extracted the $N^*$ mass on the large lattices and plotted its ratio to the nucleon mass in Fig. 3.11. The result if given down to $(m_{\rm PS}/m_{\rm V})^2 = 0.3$ as the errors became too large for smaller values of this ratio. Nevertheless, it is encouraging as the finer lattices show a linear behavior that extrapolates well to the experimental point.

### Dispersion relations

The relativistic energy momentum relation in the continuum reads with the speed of light $c = 1$, the energy $E$ and the rest mass of the particle $m$

$$m^2 = E^2 - \mathbf{p}^2 \ . \tag{3.42}$$

A priori, it isn't clear that this is valid on the lattice too. However, the more continuum properties are realized at finite lattice spacing, the easier is the continuum limit. The various Dirac operators perform very differently in this respect,

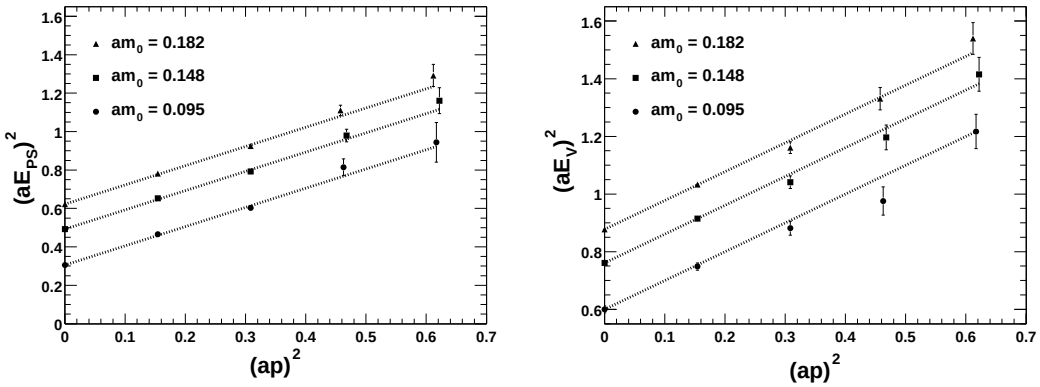


Figure 3.12: The dispersion relation for the $\pi$ on the left and the $\rho$ on the right for three different values of the quark mass parameter. The lines are the continuum relation Eq. (3.42) starting at $\mathbf{p} = 0$. The data is from the $16^3 \times 32$ sample with $\beta_1 = 7.90$.

see [GH00] for a comprehensive analysis in two dimensions. Whereas the Perfect Action is constructed such that Eq. (3.42) is fulfilled for all momenta in the Brillouin zone, the overlap operator starting from the Wilson action shows a very poor result. We now look at the dispersion relations for the nucleon, the pseudoscalar and the vector meson for the chirally improved operator. On a lattice with lattice size $L$ the momentum can take discrete values

$$p_\mu = \frac{2\pi}{L} n_\mu \,; \qquad n_\mu \in \left\{ -\frac{L}{2} + 1, \ldots, \frac{L}{2} \right\} \,. \tag{3.43}$$

We use all combinations of momenta with $|\mathbf{p}| \leq 4\pi/L$. The energies are averaged over the different directions where possible.

The dispersion relations for the pseudoscalar and the vector meson are shown for $\beta_1 = 7.90$ and three different values of the quark mass parameter $am_0$ in Fig. 3.12. Within the errorbars we have a good agreement with the continuum relations indicated by the straight lines.

Another measure for the quality of the dispersion relation is the following quantity, which should be 1 for perfect agreement with the continuum result and is sometimes called speed of light $c$

$$c = \frac{E^2 - m^2}{p^2} \,. \tag{3.44}$$

It is plotted for three bare quark masses and momentum $|a\mathbf{p}| = 2\pi/L$ for $\beta_1 = 7.90$ on the $16^3 \times 32$ lattices in Fig. 3.13. There is no statistically significant deviation from the continuum dispersion relation.

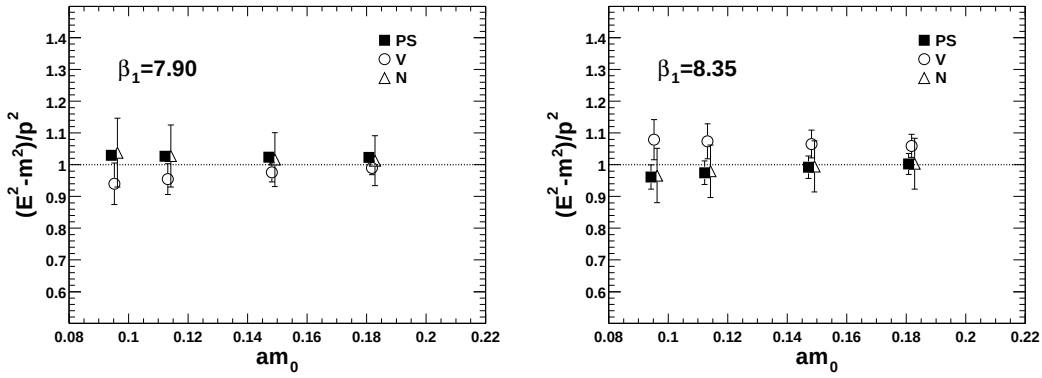


Figure 3.13: The speed of light for the nucleon, pseudoscalar and vector meson. The results are slightly displaced. The parameters are $\beta_1 = 7.90$ and 8.35 on $16^3 \times 32$ with $|a\mathbf{p}| = 2\pi/L$.

### 3.3.3 Scaling properties

We have already seen that the proton and the vector meson mass show relatively small dependence on $\beta_1$, i.e., the lattice spacing. To disentangle finite size and discretization effects it is standard to look at the following kind of plot: The mass of a hadron is computed at fixed $m_{\mathrm{PS}}/m_{\mathrm{V}}$ ratio for which we took 0.7. This value is plotted for fixed physical volume ($L \approx 1.2$ fm) but different lattice spacing as a function of $a^2/r_0^2$. A constant behavior is interpreted as good scaling properties of the action. That this is the case for the chirally improved operator is demonstrated in Fig. 3.14.

### 3.3.4 Summary

We presented first results for the hadron spectrum computed with the chirally improved Dirac operator. We looked into the dependence of the mass of the pseudoscalar meson squared on the quark mass. The chiral properties of the Dirac operator turned out to be good; we are able to simulate at $m_{\mathrm{PS}}/m_{\mathrm{V}} \approx 0.3$ without facing exceptional configurations. We discussed the difficulties of the extraction of the coefficient $\delta$ of the quenched chiral logarithm. Furthermore, we looked into the mass of the vector meson and the nucleon. We showed that the vector meson mass in the chiral limit agrees sufficiently well with the experimental value of the $\rho$ mass. The proton mass, too, had the expected dependence on the pion mass (APE plot). The results for the $N^*$ are promising. Moreover, the dispersion relations for the various particles agree well with the continuum result. The hadron masses scale well. These findings hint on a good behavior

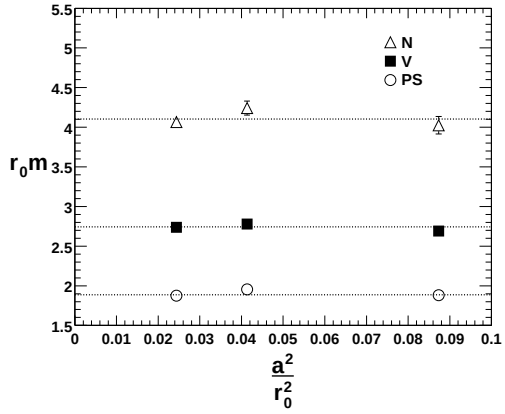


Figure 3.14: The nucleon, pseudoscalar and vector meson mass for $m_{\mathrm{PS}}/m_{\mathrm{V}} = 0.7$ and constant physical volume as a function of $a^2/r_0^2$. The values are constant within statistical error which suggests good scaling behavior of the action.

in the continuum limit. We can, thus, summarize that the chirally improved operator has proven to have good properties for the computation of hadronic observables at small quark masses. Hence it can be used for further studies, e.g., of the internal structure of individual hadrons.

| $am_0$ | $am_{\rm PS}$ | $am_{\rm PPSS}$ | $am_V$ | $am_N$ | $m_{\rm PS}/m_{\rm V}$ |
|---|---|---|---|---|---|
| 0.020 | 0.257(3) | 0.251(4) | 0.65(2) | 0.82(2) | 0.39(1) |
| 0.030 | 0.311(2) | 0.310(3) | 0.67(1) | 0.87(1) | 0.46(1) |
| 0.039 | 0.356(2) | 0.357(3) | 0.684(9) | 0.92(1) | 0.519(9) |
| 0.049 | 0.395(2) | 0.398(2) | 0.699(8) | 0.96(1) | 0.564(8) |
| 0.058 | 0.431(2) | 0.435(2) | 0.714(7) | 1.00(1) | 0.603(7) |
| 0.077 | 0.495(2) | 0.501(2) | 0.745(5) | 1.07(1) | 0.664(6) |
| 0.095 | 0.553(2) | 0.559(2) | 0.774(8) | 1.14(1) | 0.714(7) |
| 0.113 | 0.606(2) | 0.613(2) | 0.807(6) | 1.21(1) | 0.751(6) |
| 0.148 | 0.702(2) | 0.709(2) | 0.872(4) | 1.32(1) | 0.805(4) |
| 0.182 | 0.789(2) | 0.796(2) | 0.937(3) | 1.43(1) | 0.842(3) |

Table 3.2: Hadron masses for $\beta_1 = 7.90$ on the $16^3 \times 32$ lattice.

| $am_0$ | $am_{\rm PS}$ | $am_{\rm PPSS}$ | $am_V$ | $am_N$ | $m_{\rm PS}/m_{\rm V}$ |
|---|---|---|---|---|---|
| 0.020 | 0.254(5) | 0.248(6) | 0.68(2) | 0.79(4) | 0.38(1) |
| 0.030 | 0.310(3) | 0.307(4) | 0.69(2) | 0.86(2) | 0.450(9) |
| 0.039 | 0.355(2) | 0.354(3) | 0.70(1) | 0.91(2) | 0.506(8) |
| 0.049 | 0.395(2) | 0.395(3) | 0.71(1) | 0.95(1) | 0.555(9) |
| 0.058 | 0.431(2) | 0.433(2) | 0.73(1) | 0.99(1) | 0.594(8) |
| 0.077 | 0.496(2) | 0.500(2) | 0.76(1) | 1.06(1) | 0.657(8) |
| 0.095 | 0.554(2) | 0.559(2) | 0.79(1) | 1.13(1) | 0.70(1) |
| 0.113 | 0.607(2) | 0.613(2) | 0.819(9) | 1.190(9) | 0.740(8) |
| 0.148 | 0.703(2) | 0.711(2) | 0.880(5) | 1.307(9) | 0.798(3) |
| 0.182 | 0.789(2) | 0.798(2) | 0.943(4) | 1.418(9) | 0.837(3) |

Table 3.3: Hadron masses for $\beta_1 = 7.90$ on the $12^3 \times 24$ lattice.

| $am_0$ | $am_{\rm PS}$ | $am_{\rm PPSS}$ | $am_V$ | $am_N$ | $m_{\rm PS}/m_{\rm V}$ |
|---|---|---|---|---|---|
| 0.020 | 0.29(3) | 0.20(2) | 0.60(3) | 1.0(5) | 0.48(7) |
| 0.030 | 0.32(2) | 0.28(1) | 0.65(2) | 0.91(9) | 0.50(3) |
| 0.039 | 0.36(1) | 0.34(1) | 0.68(2) | 0.98(6) | 0.54(3) |
| 0.049 | 0.40(1) | 0.385(9) | 0.70(2) | 1.03(4) | 0.58(2) |
| 0.058 | 0.44(1) | 0.425(9) | 0.72(2) | 1.07(4) | 0.61(2) |
| 0.077 | 0.498(8) | 0.497(8) | 0.75(1) | 1.14(3) | 0.66(2) |
| 0.095 | 0.556(7) | 0.559(7) | 0.80(1) | 1.21(3) | 0.70(2) |
| 0.113 | 0.609(6) | 0.614(6) | 0.83(1) | 1.27(2) | 0.74(1) |
| 0.148 | 0.705(5) | 0.714(5) | 0.881(8) | 1.39(2) | 0.801(8) |
| 0.182 | 0.793(4) | 0.803(5) | 0.945(6) | 1.49(1) | 0.839(5) |

Table 3.4: Hadron masses for $\beta_1 = 7.90$ on the $8^3 \times 24$ lattice.

| $am_0$ | $am_{\rm PS}$ | $am_{\rm PPSS}$ | $am_V$ | $am_N$ | $m_{\rm PS}/m_{\rm V}$ |
|---|---|---|---|---|---|
| 0.010 | 0.171(5) | 0.156(6) | 0.47(1) | 0.60(5) | 0.36(1) |
| 0.015 | 0.199(4) | 0.193(5) | 0.47(1) | 0.63(2) | 0.420(9) |
| 0.020 | 0.224(4) | 0.223(5) | 0.479(9) | 0.66(2) | 0.468(7) |
| 0.030 | 0.269(3) | 0.275(4) | 0.496(6) | 0.71(1) | 0.544(5) |
| 0.039 | 0.309(3) | 0.317(3) | 0.513(5) | 0.75(1) | 0.602(3) |
| 0.049 | 0.344(2) | 0.355(3) | 0.529(4) | 0.78(1) | 0.650(4) |
| 0.058 | 0.376(2) | 0.389(2) | 0.546(3) | 0.820(9) | 0.689(4) |
| 0.077 | 0.435(2) | 0.449(2) | 0.581(3) | 0.888(8) | 0.748(3) |
| 0.095 | 0.488(1) | 0.503(2) | 0.615(5) | 0.951(8) | 0.795(7) |
| 0.113 | 0.538(1) | 0.552(2) | 0.651(5) | 1.012(7) | 0.827(6) |
| 0.148 | 0.628(1) | 0.642(2) | 0.722(4) | 1.127(8) | 0.871(5) |
| 0.182 | 0.711(1) | 0.724(2) | 0.791(4) | 1.237(9) | 0.899(4) |

Table 3.5: Hadron masses for $\beta_1 = 8.35$ on the $16^3 \times 32$ lattice.

| $am_0$ | $am_{\rm PS}$ | $am_{\rm PPSS}$ | $am_V$ | $am_N$ | $m_{\rm PS}/m_{\rm V}$ |
|---|---|---|---|---|---|
| 0.010 | 0.18(2) | 0.15(2) | 0.48(2) | 0.6(1) | 0.37(4) |
| 0.020 | 0.22(1) | 0.22(1) | 0.49(1) | 0.67(3) | 0.46(2) |
| 0.030 | 0.269(8) | 0.275(9) | 0.51(1) | 0.74(3) | 0.53(1) |
| 0.039 | 0.308(7) | 0.319(7) | 0.52(1) | 0.77(1) | 0.59(1) |
| 0.049 | 0.344(6) | 0.358(5) | 0.54(1) | 0.81(1) | 0.639(8) |
| 0.058 | 0.376(6) | 0.392(5) | 0.55(1) | 0.84(1) | 0.679(8) |
| 0.077 | 0.435(5) | 0.453(4) | 0.59(1) | 0.91(1) | 0.741(7) |
| 0.095 | 0.488(4) | 0.508(3) | 0.62(1) | 0.97(1) | 0.793(9) |
| 0.113 | 0.538(4) | 0.557(3) | 0.65(1) | 1.02(1) | 0.826(8) |
| 0.148 | 0.628(4) | 0.647(3) | 0.720(8) | 1.14(1) | 0.872(6) |
| 0.182 | 0.711(3) | 0.729(3) | 0.789(7) | 1.24(1) | 0.900(5) |

Table 3.6: Hadron masses for $\beta_1 = 8.35$ on the $12^3 \times 24$ lattice.

| $am_0$ | $am_{\rm PS}$ | $am_{\rm PPSS}$ | $am_V$ | $am_N$ | $m_{\rm PS}/m_{\rm V}$ |
|---|---|---|---|---|---|
| 0.010 | 0.167(5) | 0.149(6) | 0.37(2) | 0.52(4) | 0.47(3) |
| 0.020 | 0.210(3) | 0.213(4) | 0.39(1) | 0.55(2) | 0.56(2) |
| 0.030 | 0.249(2) | 0.260(3) | 0.41(1) | 0.60(1) | 0.63(1) |
| 0.039 | 0.284(2) | 0.299(3) | 0.423(8) | 0.63(1) | 0.69(1) |
| 0.049 | 0.317(2) | 0.333(2) | 0.440(6) | 0.67(1) | 0.734(7) |
| 0.058 | 0.346(2) | 0.364(2) | 0.459(5) | 0.70(1) | 0.767(6) |
| 0.077 | 0.401(2) | 0.419(2) | 0.498(4) | 0.76(1) | 0.815(5) |
| 0.095 | 0.451(2) | 0.469(2) | 0.533(5) | 0.83(1) | 0.856(3) |
| 0.113 | 0.498(2) | 0.515(2) | 0.569(4) | 0.88(1) | 0.880(3) |
| 0.148 | 0.585(2) | 0.600(1) | 0.643(3) | 1.00(1) | 0.913(2) |
| 0.182 | 0.665(2) | 0.679(1) | 0.714(3) | 1.11(1) | 0.933(1) |

Table 3.7: Hadron masses for $\beta_1 = 8.70$ on the $16^3 \times 32$ lattice.

# Chapter 4

# Hadron Structure

The explanation of the various high energy experiments, e.g., high energy lepton-nucleon or proton-proton scattering, is a major success of QCD. From these experiments so-called structure functions can be extracted. In the parton picture of QCD the structure functions are convolutions of perturbatively calculable Wilson coefficients with parton distribution functions. The parton distributions encode the information about the hadron structure. They are universal which means that the same parton distributions can be extracted from a variety of high energy processes. This is the statement of factorization theorems. However, the parton distributions are not predictable in perturbation theory. This is where lattice QCD comes into play. The moments of parton distribution functions are related to forward matrix elements of two-fermion operators inside the hadron. These matrix elements are calculable on the lattice.

For the nucleon these matrix elements have been examined in great detail, e.g. [G$^+$96b]. We extend these investigations into two directions. Firstly, we compute moments of structure functions inside the $\Lambda$ hyperon. Secondly, we look into certain matrix elements which contribute to corrections to the standard (leading-twist) parton picture. These are four-fermion (higher-twist) matrix elements inside the proton. In contrast to the calculations presented in the preceding chapters, we use clover improved Wilson fermions for the first project and Wilson fermions for the second one. We apply the quenched approximation in both investigations.

This chapter is organized as follows. In Section 4.1, the definitions of the structure functions are introduced along with the formulae which connect experimental data to the matrix elements calculable on the lattice. The technique used to compute the matrix elements is described in Sec. 4.2. In Section 4.3, we look into the structure of the $\Lambda$ hyperon. After that, in Sec. 4.4, four-fermi operators inside the proton are in the focus of our interest.

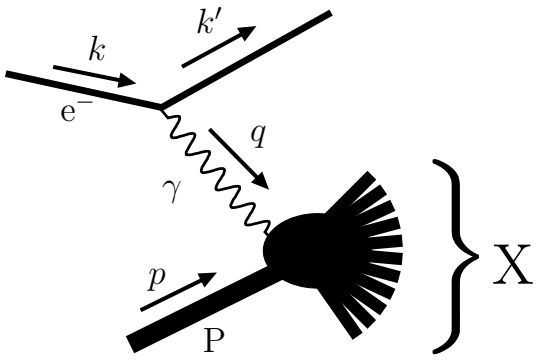


Figure 4.1: In DIS a lepton (here an electron) with momentum $k$ scatters off a proton P with momentum $p$ by exchanging a photon $\gamma$. The photon's momentum $q$ is deeply virtual $Q^2 \equiv -q^2 \gg 1$ GeV$^2$. The proton is destroyed, the remnants are summarized by $X$. They are not detected. The outgoing electron has momentum $k'$.

## 4.1 Structure Functions

In deep inelastic lepton nucleon scattering (DIS) a lepton scatters off a nucleon, see Fig. 4.1. In the final state only the lepton is detected. The nucleon is destroyed and it is summed over all final states. In this section we give the formulae in Minkowski space and return to Euclidean space-time afterwards. More information can be found in textbooks, e.g. [ESW96]. In the standard convention $p$ is the proton momentum, $k$ and $k'$ are the momenta of the incoming and the outgoing lepton, respectively. We can assume single photon exchange. Then the exchanged photon has momentum $q^\mu = k^\mu - k'^\mu$. Furthermore, it is standard to define the following invariants:

$$Q^2 = -q^2 \qquad\qquad x = \frac{Q^2}{2p \cdot q} \tag{4.1}$$

$$\nu = p \cdot q \qquad\qquad y = \frac{p \cdot q}{k \cdot p} \tag{4.2}$$

The DIS cross section is parameterized in the target rest frame, i.e., $p^\mu = (m_p, 0, 0, 0)$ with the energy $E$ of the incoming lepton, using the proton mass $m_p^2 = p^2$ and the electromagnetic fine-structure constant $\alpha_{\text{em}}$

$$\begin{aligned}\frac{\mathrm{d}^2\sigma}{\mathrm{d}x\,\mathrm{d}y} =& \frac{8\pi m_p \alpha_{\text{em}} E}{Q^4}\left[\left(\frac{1+(1+y)^2}{2}\right) 2xF_1(x,Q^2)\right. \\ &\left. +(1-y)(F_2(x,Q^2) - 2xF_1(x,Q^2)) - \frac{m_p xy}{2E}F_2(x,Q^2)\right] .\end{aligned} \tag{4.3}$$

The structure functions $F_1(x, Q^2)$ and $F_2(x, Q^2)$ depend on the two invariant scalars $x$ and $Q^2$. The description of their $Q^2$ dependence is one of the major

successes of perturbative QCD.

### 4.1.1 Unpolarized Scattering: Leading twist

In the *deep inelastic limit* $Q^2 \to \infty$ with $x$ fixed, the so-called *leading twist* contribution $F_2^{\rm lt}(x, Q^2)$ dominates (the precise meaning of this will be given below):

$$F_2(x, Q^2) = F_2^{\rm lt}(x, Q^2) + \mathcal{O}(\frac{m_p^2}{Q^2}) \tag{4.4}$$

The leading twist structure function depends only logarithmically on $Q^2$. A factorization theorem expresses this as a convolution of Wilson coefficient functions $C_{2,q}(x, \alpha_s(Q^2))$ and $C_{2,g}(x, \alpha_s(Q^2))$ ($\alpha_s = g^2/(4\pi)$ is the strong coupling constant) and *parton distribution functions* $q_i(x, Q^2)$ and $g(x, Q^2)$ for the quarks and the gluons respectively.

$$\begin{aligned} F_2^{\rm lt}(x, Q^2) = x \sum_{q \in u,d,s,\ldots} e_q^2 \int_x^1 \frac{{\rm d}\xi}{\xi} \Big\{ \big[q_i(\xi, Q^2) + \bar{q}_i(\xi, Q^2)\big] C_{2,q}(\frac{x}{\xi}, \alpha(Q^2)) + \\ \frac{1}{N_f} g(\xi, Q^2) C_{2,g}(\frac{x}{\xi}, \alpha(Q^2)) \Big\} \end{aligned} \tag{4.5}$$

with $e_q$ the electric charge of a quark with flavor $q$. $N_f$ is the number of active flavors. We have identified the factorization and renormalization scales with $Q^2$. In leading order, the parton distribution functions can be interpreted probabilistically (up to the normalization). $q(x)$ gives the probability of finding a quark of flavor $q$ with momentum $xp$ inside the proton of momentum $p$.

The Wilson coefficients can be found in the perturbative next-to-next-to-leading order (NNLO) approximation in [vNZ91, ZvN92]. The $Q^2$ dependence of the parton distribution functions is governed by the *splitting functions* $P_{q_i,q_i'}$. It is given by the evolution equation

$$\frac{\partial}{\partial \ln Q^2} q_i(Q^2) = \frac{\alpha_s(Q^2)}{2\pi} \sum_j \int_x^1 \frac{{\rm d}\xi}{\xi} P_{q_i,q_j}(\frac{x}{\xi}, \alpha_s(Q^2)) q_j(\xi, Q^2) \ . \tag{4.6}$$

This is a coupled integro-differential equation. So the parton distribution for flavor $i$ at scale $Q_1$ depends on all other distributions at the scale a $Q_2$; they mix under evolution. The leading twist parton distributions have been extracted from experiment. Some recent results can be found in [GRV98, MRST01, P$^+$02].

In order to connect the parton distributions to matrix elements calculable on the lattice, it is useful to define the following moments

$$\langle x^{n-1} \rangle^f \equiv \int_0^1 {\rm d}x \, x^{n-1} q^f(x) \, . \tag{4.7}$$

The first moment ($n = 1$) gives the number of quarks of flavor $f$ in the hadron, whereas the second moment $\langle x \rangle^f$ gives their average momentum fraction. The distributions are normalized in the proton such that

$$\int_0^1 \mathrm{d}x \, [q(x) - \bar{q}(x)] = \begin{cases} 1 & \text{for} \quad q = d \\ 2 & \text{for} \quad q = u \end{cases} . \tag{4.8}$$

In the framework of the operator product expansion (OPE), these moments are given by forward matrix elements of two-quark operators $\mathcal{O}$ which in Minkowski space read

$$\mathcal{O}^f_{\mu_1 \cdots \mu_n} = \left( \frac{\mathrm{i}}{2} \right)^{n-1} \bar{\psi}^f \gamma_{\mu_1} \overleftrightarrow{D}_{\mu_2} \cdots \overleftrightarrow{D}_{\mu_n} \psi^f - \text{traces} . \tag{4.9}$$

The $\psi^f$ is the up (down) quark field for $f = u, d$. $\overleftrightarrow{D}_\mu$ denote the covariant derivatives acting in both directions:

$$\overleftrightarrow{D}_\mu = \overrightarrow{D}_\mu - \overleftarrow{D}_\mu . \tag{4.10}$$

We consider the operators of Eq. (4.9) symmetrized in the indices $\mathcal{O}^f_{\{\mu_1 \cdots \mu_n\}}$, which is indicated by $\{\cdots\}$. These have twist two. The twist of an operator with mass dimension $d$ and spin $n$ is defined as $d - n$. The fermion fields have mass dimension 3/2, the covariant derivative 1. Symmetrization of the indices couples the individual spins to maximal total spin. The spin of the fermions is 1/2, the derivatives carry spin 1. So the mass dimension of $\mathcal{O}^f_{\{\mu_1 \cdots \mu_n\}}$ is $(n + 2)$ and the spin is $n$. This leads to a twist of two. The (even) twist gives the order $(t/2 - 1)$ at which an operator contributes in the expansion of $F_2(x, Q^2)$ in $m_p^2/Q^2$.

We want to consider matrix elements between nucleon states of equal spatial momenta $\mathbf{p}$. For the unpolarized scattering we sum over the spin $\mathbf{s}$. To separate the Lorentz structure from the non-perturbative information the following *reduced matrix elements* $v_n^{(f)}$ are defined by [G+96b]

$$\frac{1}{2} \sum_{\mathbf{s}} \langle \mathbf{p}, \mathbf{s} | \mathcal{O}^f_{\{\mu_1 \cdots \mu_n\}} | \mathbf{p}, \mathbf{s} \rangle = 2 v_n^{(f)} [p_{\mu_1} \cdots p_{\mu_n} - \text{traces}] . \tag{4.11}$$

The normalization of the proton states and the spin $s$ are chosen such that

$$\langle \mathbf{p}', \mathbf{s}' | \mathbf{p}, \mathbf{s} \rangle = (2\pi)^3 2 E_{\mathbf{p}} \delta(\mathbf{p} - \mathbf{p}') \delta_{\mathbf{s},\mathbf{s}'}, \qquad s^2 = -m_p^2 . \tag{4.12}$$

The reduced matrix elements in Eq. (4.11) are equal to the moments of the leading twist parton distribution functions

$$\langle x^{n-1} \rangle^f = v_n^{(f)} . \tag{4.13}$$

### 4.1.2 Unpolarized Scattering: Higher twist

In the previous section, the leading twist part $F^{\rm lt}(x,Q^2)$ of the structure function $F_2(x,Q^2)$ has been introduced. This amounts to neglecting the $1/Q^2$ terms in the full structure functions, see Eq. (4.4). It is a good approximation in the high energy region, e.g. $Q^2 > 4$ GeV$^2$ and $W^2 = Q^2(1-x)/x > 10$ GeV$^2$ [MRST01]. For $Q^2$ between 1 GeV$^2$ and 4 GeV$^2$, this approximation becomes questionable. In the next order of the $1/Q^2$ expansion, we get two contributions arising from different sources.

- **twist four operators:** In the operator product expansion the order in which an operator contributes to the $1/Q^2$ series is given by $(t-2)/2$ for $t$ the (even) twist of the operator. Operators of higher twist are, e.g., the four-fermion operators we are going to compute in Sec. 4.4

$$\bar\psi\gamma_{\{\mu}\psi\bar\psi\gamma_{\nu\}}\psi \ . \tag{4.14}$$

- **target mass corrections:** In the leading twist approximation the mass of the target — the nucleon — is neglected. The correction of this effect amounts to terms which start at order $1/Q^2$. It is under good control and can be computed from the leading twist part alone [Nac73, GP76].[1]

However, it is much more difficult to extract the higher twist part from experiment than the leading twist contribution. This comes mainly from the mixing of a large number of operators under evolution. The coefficient functions are known only to the leading order [LWW81, LW82]. There are no higher order results for splitting and coefficient functions. Even if all these functions were known to appropriate precision, the extraction would be practically impossible. One would need extremely precise data to disentangle the power corrections, which are due to the higher twist contributions, and the logarithmic corrections, which stem from the evolution.

Some studies to get hold of the higher twist have been done in the past [VM92, Ale99, Ale00, MRST98]. Our own analysis is published in Ref. [SSS01]. All of them make a specific assumption on the shape and the evolution of the higher twist part. From this one can extract some information on the magnitude of the higher twist effects.

To get a feeling for the different contributions, we have included Fig. 4.2 from [SSS01]. The result of an analysis trying to disentangle the logarithmic dependence of the leading twist structure function on $Q^2$ from the power behavior of the higher twist part is shown. To this end we analyze BCDMS [BCDMS89] and old SLAC data [WRD$^+$92]. As ansatz for the structure function we use

$$F_2(x,Q^2) = F_2^{lt,TMC}(x,Q^2)(1+\frac{h(x)}{Q^2}) \ , \tag{4.15}$$

[1] Be aware of the different definition of the structure function in [GP76].

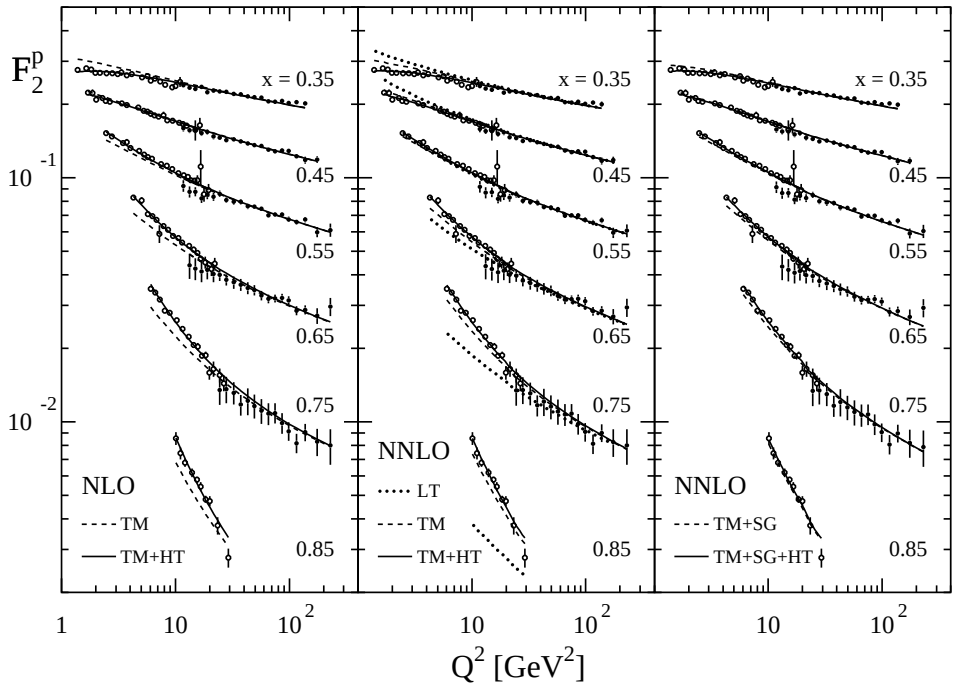


Figure 4.2: Fit to the structure function $F_2(x, Q^2)$. The dotted line is the leading twist contribution. The target mass corrections have been added in the dashed line. The higher twist effects are included in the solid line. The three figures show the results for different precision of the Wilson coefficient function. On the left, the NLO result has been used, in the middle plot the NNLO result. In the right plot we show the result for additional soft gluon corrections which improve the Wilson coefficient in the region $x \sim 1$.

where $F_2^{lt,TMC}(x,Q^2)$ denotes the leading twist structure function with target mass correction included. This introduces 6 parameters, as the data is binned into 6 $x$-bins (ranging from $x = 0.35$ to $x = 0.85$). Since we analyze data with comparatively large $x$, we are able to use the non-singlet approximation, i.e., we do not decompose the parton distribution into the individual flavors which is even not possible for these data sets alone. The aim is to study the dependence of the result on the improvement in the perturbative description of the leading twist part. So we perform fits with this part described in NLO, NNLO, and Wilson coefficients improved by so-called soft gluon resummations [Vog99].[2] The three resulting plots are shown in Fig. 4.2. In each plot the same data is given. The different $x$-bins are separated by horizontal gaps. In the middle plot the pure leading twist result is given by the dotted line. We see that this contribution dominates for large $Q^2$ and not too large $x$. Both, the higher twist as well as the TMC contribution are negligible in this region. For lower $Q^2$ the TMC contribution becomes sizeable. This is shown by the dashed line which gives the leading twist part with TMC included. The full result of the fit is shown in the solid curves. The higher twist contribution is non-vanishing. It is impossible to fit the data without the higher twist included. However, the necessity of higher twist diminishes as the description of the leading twist part is improved. This is shown in Fig. 4.3 where the function $h(x)$ used in ansatz (4.15) is plotted for the three different cases.

### 4.1.3 Polarized scattering

The same analysis as in the preceding sections can be performed for polarized scattering, where the spins of the lepton and the target are known. Then the different polarizations are not summed over but asymmetries in the cross-sections for different lepton and target polarizations are measured. The cross-section with the target polarization along the beam line can be parameterized by the two structure functions $g_1(x,Q^2)$ and $g_2(x,Q^2)$. We are interested in the former. Again, the leading twist parton distributions can be extracted, for the nucleon see, e.g. [GRSV01]. The moments of these are given by forward matrix elements of operators involving $\gamma_\sigma\gamma_5$. These define the reduced matrix elements $a_n^{(f)}$.

$$\langle \mathbf{p},\mathbf{s}|\mathcal{O}^{5(f)}_{\{\sigma\mu_1\cdots\mu_n\}}|\mathbf{p},\mathbf{s}\rangle = \frac{1}{n+1}a_n^{(f)}[s_\sigma p_{\mu_1}\cdots p_{\mu_n} + \cdots - \text{traces}] \quad (4.16)$$

$$\mathcal{O}^{5(f)}_{\sigma\mu_1\cdots\mu_n} = \left(\frac{\mathrm{i}}{2}\right)^n \psi^f\gamma_\sigma\gamma_5\overleftrightarrow{D}_{\mu_1}\cdots\overleftrightarrow{D}_{\mu_n}\psi^f - \text{traces} \quad (4.17)$$

[2]The contributions from soft gluons are terms which arise in each order of the perturbative expansion of the Wilson coefficient and dominate for $x \to 1$. We use the Wilson coefficient in which these contributions are resummed and one thus expects a more precise description of the data in this region.

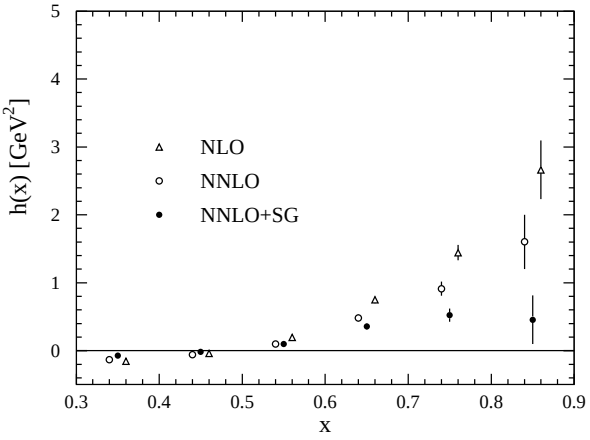


Figure 4.3: The function describing the higher twist part $h(x)$ from Eq. (4.15). The function values get smaller for higher precision of the perturbative input (from the NLO approximation to the soft gluon resummed coefficient functions in NNLO). However, a non-vanishing contribution remains.

The first moments of the parton distributions $a_0^{(f)}$ give the fraction of the spin carried by the $u$ and $d$ quarks $\Delta u$ and $\Delta d$, respectively.

$$a_0^{(u)} = 2\Delta u \qquad\qquad a_0^{(d)} = 2\Delta d \tag{4.18}$$

Similar interpretations hold for the operators with more derivatives which give higher moments of the structure functions.

A target polarization perpendicular to the beam line leads to the transversity distributions. Analogously to the spin content the so-called tensor charge $\delta q$ is defined in Minkowski space by [JJ91]

$$\langle \mathbf{p}, \mathbf{s} | \bar{\psi}^f i\sigma_{\mu\nu}\gamma_5 \psi^f | \mathbf{p}, \mathbf{s} \rangle = \frac{2}{m}(s_\mu p_\nu - s_\nu p_\mu)\delta q \ . \tag{4.19}$$

### 4.1.4 Outline of the rest of the chapter

The moments of leading twist structure functions of the nucleon have been studied for a long time on the lattice in the quenched approximation (e.g. [G$^+$96b]) and, more recently, in full QCD, e.g., [QCDSF02a, LHPC02]. Our investigations extend these efforts in two directions. First, we study the lowest moments of leading twist structure functions in the $\Lambda$ hyperon. There we emphasize in particular the flavor symmetry breaking effects due to, both, the different wave functions of the $\Lambda$ and the proton and the different masses of the strange and the light quarks. Second, we compute matrix elements of four-fermion operators in the nucleon which contribute to the higher twist structure functions. In both projects we use the quenched approximation. To lay the grounds for these

computations we first have to describe how to compute such matrix elements on the lattice. The results for the $\Lambda$ can be found in Section 4.3. These results are already published in Refs. [QCDSF02b, QCDSF02c]. The results on four-fermi operators inside the proton, which are published in Refs. [C$^+$01a, G$^+$02c, G$^+$02d], are reported in Section 4.4.

## 4.2 Computation of three-point functions

In this section, the method to get matrix elements of operators inside hadrons from three-point functions measured on the lattice is described. From now on, the formulae are given in Euclidean space-time again. We want to compute matrix elements of two- and four-fermion operators. Forward means in this context that the momentum of the bra and the ket hadron are the same. For a baryon $B$ with spatial momentum $\mathbf{p}$, we want to measure the following matrix elements

$$\langle B, \mathbf{p}|\mathcal{O}|B, \mathbf{p}\rangle \ . \tag{4.20}$$

The general form of a two-fermion operator, using a matrix $F$ to generate the flavor structure and $\Gamma$ for the Dirac structure, is

$$\mathcal{O} = \Gamma_{\alpha,\beta} F_{f,f'} \bar{\psi}^{f,c}_{\alpha} \psi^{f',c}_{\beta} \ . \tag{4.21}$$

The operators in Euclidean space differ from the ones in Eqs. (4.9) and (4.17) only by factors of $i$. The operators that we use in our computations are given below. To put this operator on the lattice, we use the same trick as in the case of the two-point functions from which we extracted the masses. We substitute the physical hadrons by currents which have the same quantum numbers.

We take as interpolating fields for the proton Eqs. (3.21) and (3.22), which we already used in the calculation of its mass; for the $\Lambda$ see Eq. (4.36) below. We now consider the following three-point function

$$C_{\Gamma^s}(t, \tau; \mathbf{p}, \mathcal{O}) = \Gamma^s_{\alpha\beta} \langle B_\alpha(\mathbf{p}, t) \mathcal{O}(\tau) \bar{B}_\beta(\mathbf{p}, 0)\rangle \tag{4.22}$$

with $0 < \tau < t < T$. $\Gamma^s$ gives the polarization of the hadrons in the matrix element.

$$\Gamma^s = \begin{cases} \frac{1}{2}(1+\gamma_4) & \text{for the sum over the polarizations} \\ \frac{1}{2}(1+\gamma_4) i\gamma_2\gamma_5 & \text{for polarization in the 2–direction} \end{cases} \tag{4.23}$$

We follow the same line of argument as in the case of the two-point function. We insert complete sets of eigenstates of the Hamilton operator $H$ and let the time separations become large. As the time evolution operator in Euclidean space-time is $\exp(-Ht)$ the higher states are exponentially suppressed by the difference of

their energies. These differences are relatively large. In this way only the lowest states contribute.

$$C_{\Gamma^s}(t,\tau;\mathbf{p},\mathcal{O}) = \Gamma^s_{\alpha\beta}\frac{\sum_n \langle n|B_\alpha(\mathbf{p})e^{-(t-\tau)H}\mathcal{O}e^{-\tau H}\bar{B}_\beta(\mathbf{p})e^{-(T-t)H}|n\rangle}{\sum_m \langle m|e^{-TH}|m\rangle} \tag{4.24}$$

We only keep the contributions with the lowest energy and set the vacuum energy to zero. We get for $0 \ll \tau \ll t \ll T$

$$C_{\Gamma^s}(t,\tau;\mathbf{p},\mathcal{O}) \overset{T\to\infty}{=} \Gamma^s_{\alpha\beta}e^{-tE_p}\langle 0|B_\alpha(\mathbf{p})|B\rangle\langle B|\mathcal{O}|B\rangle\langle B|\bar{B}_\beta(\mathbf{p})|0\rangle + \dots \tag{4.25}$$

Now we have to compare this to the corresponding hadron two-point function $C_{\tilde{\Gamma}^s}(t;\mathbf{p})$ which in the region $0 \ll t \ll T$ gives

$$\begin{aligned} C_{\tilde{\Gamma}^s}(t;\mathbf{p}) \equiv& \tilde{\Gamma}^s_{\alpha\beta}\langle B_\alpha(\mathbf{p},t)\bar{B}_\beta(\mathbf{p},0)\rangle \\ \overset{0\ll t\ll T}{=}& \tilde{\Gamma}^s_{\alpha\beta}(e^{-tE_B}\langle B|\bar{B}_\beta(\mathbf{p})|0\rangle\langle 0|B_\alpha(\mathbf{p})|B\rangle \\ &+ e^{-(T-t)E_{B^*}}\langle \bar{B}^*|B_\alpha(\mathbf{p})|0\rangle\langle 0|\bar{B}_\beta(\mathbf{p})|\bar{B}^*\rangle) \end{aligned} \tag{4.26}$$

with $\tilde{\Gamma}^s = \frac{1}{2}(1+\gamma_4)$ and $\bar{B}^*$ the parity partner of the baryon $B$. Let us now consider the region where the second contribution in the two- and three-point function is small. If we divide the three-point by the two-point function, the exponentials as well as the overlap of the interpolating field with the physical hadron state cancel out.

$$R(\mathbf{p},\Gamma^s,\mathcal{O}) = \frac{C_{\Gamma^s}(t,\tau;\mathbf{p},\mathcal{O})}{C_{\tilde{\Gamma}^s}(t;\mathbf{p})} = \langle B,\mathbf{p}|\mathcal{O}|B,\mathbf{p}\rangle \tag{4.27}$$

The ratio $R$ is independent of $t$ as well as of $\tau$. So if we keep $t$ fixed and vary $\tau$, we expect to have a *plateau* in $\tau$ for $0 < \tau < t$. In the region of $\tau > t$, the three-point function Eq. (4.25) is exponentially suppressed with respect to the region of $\tau < t$. Examples of plateaus in our simulation can be found in Fig. 4.6 in the next section. It is a simulation on a $16^3 \times 32$ lattice. There the source is placed at $t = 0$, the sink at $t = 13$. The position of the operator is varied between $\tau = 0$ and $\tau = 31$. The function is non-zero and almost constant where the operator is between source and sink, whereas it vanishes otherwise.

The computation of the three-point functions themselves follows the same lines as in Section 3.1. We now have to compute the following correlator:

$$\langle B_\alpha(0)\mathcal{O}(\tau)\bar{B}_\beta(t)\rangle \ . \tag{4.28}$$

As the source and sink have three quark fields each, we get for a two-fermi operator the two kinds of contribution depicted in Fig. 4.4. The graph on the left is called — for obvious reasons – connected, the one on the right disconnected. As the disconnected graph involves some kind of pair creation, one might argue that this is not consistent with the quenched approximation. Furthermore, it is very hard to compute and neglected in the following.

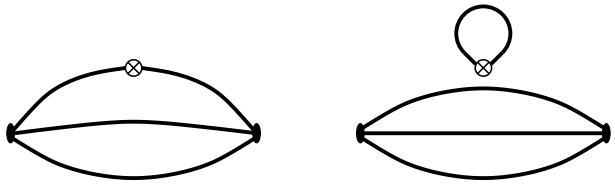

Figure 4.4: The two contributions to the three-point function of a two fermi operator in a baryon. The source and the sink are on the left and right of each graph. The operator insertion is marked as $\otimes$. On the left is the connected diagram. The disconnected graph on the right hand side is frequently ignored in the quenched approximation.

## 4.3 Structure of the $\Lambda$ hyperon

The $\Lambda$ hyperon is in the quark picture a *uds* state. Its mass is 1116 MeV. It is frequently produced in high energy reactions. There have been proposals to use the spin of a produced $\Lambda$ to learn more about the nucleon spin structure [BJ93]. This is connected to the "self-analyzing decay" $\Lambda \to p\pi^-$, which makes it easy to measure the polarization of the $\Lambda$: The angular distribution of the proton is given by

$$\frac{\mathrm{d}N_p}{\mathrm{d}\Omega} \propto 1 + \alpha \mathbf{P} \cdot \hat{\mathbf{p}} \tag{4.29}$$

with $\alpha = 0.642 \pm 0.013$, $\mathbf{P}$ the $\Lambda$ polarization vector and $\hat{\mathbf{p}}$ the unit vector of the proton momentum in the $\Lambda$'s rest frame.

Therefore, we need information about the $\Lambda$ spin structure. In the naïve SU(6) quark model, the spin of the $\Lambda$ is carried entirely by the $s$ quark. The $u$ and the $d$ quark are coupled to spin zero and isospin zero. Another possibility to gain information about the $\Lambda$ spin structure is to assume SU(3) flavor symmetry and combine proton data with parameters from the hyperon $\beta$-decay. Perfect $\mathrm{SU(3)_F}$ predicts

$$\begin{aligned} \Delta s_\Lambda &= \frac{1}{3}(2\Delta u_p - \Delta d_p + 2\Delta s_p) \ , \\ \Delta d_\Lambda &= \frac{1}{6}(\Delta u_p + 4\Delta d_p + \Delta s_p) \ . \end{aligned} \tag{4.30}$$

This leads to a contribution of the $s$ and $\bar{s}$ quarks to the $\Lambda$'s spin of $\approx 60\%$. The $u$, $\bar{u}$ and $d$, $\bar{d}$ quarks contribute $\approx -40\%$.

As the $\Lambda$ decays quickly — its lifetime is $\tau = 2.6 \cdot 10^{-10}$s — it is not possible to create a target out of it. The experimental investigations are restricted to the fragmentation of partons into a $\Lambda$.[3] Roughly speaking, the correlation between a polarized $s$ quark and the polarization of the outgoing $\Lambda$ is measured. If the $s$

[3]Fragmentation is the transition of a high energy parton into hadrons. It is a non-perturbative effect and hard to handle. But there exist successful phenomenological models.

quark has the same polarization as the $\Lambda$, it is interpreted as the $s$ quark carrying the $\Lambda$'s spin. All this is blurred by the unknown fragmentation effects and the possible decay of other hyperons. One relevant experiment has been done with $e^+e^-$ annihilation at the $Z^0$ pole [ALEPH96, OPAL98]. The produced $Z^0$ can decay into a $s\bar{s}$ pair. The $s$ quark which may fragment into a $\Lambda$ has a polarization of $-0.91$.

Another type of experiments is the fragmentation in polarized deep inelastic scattering [HERMES01]. In the DIS limit, the polarization of the exchanged photon is known. By angular momentum conservation, this implies the helicity of the struck quark. A $\Lambda$ most likely originates from the fragmentation of a strange quark. Its polarization is again measured in the self-analyzing decay.

### 4.3.1 The simulation

In order to compute the first moments of the $\Lambda$ structure functions, we have to compute the matrix elements of twist two operators, see Sec. 4.1.1 and Sec. 4.1.3. On the lattice, the choice of the operators $\mathcal{O}$ is a non-trivial task, because the discretization reduces the symmetry group of (Euclidean) space-time from $O(4)$ to the hypercubic group $H(4) \subset O(4)$. Therefore, one has to find combinations of operators, which avoid the problem of operator mixing [MS88, G$^+$96a]. After renormalization, the matrix elements of these operators are expressed in terms of the reduced matrix elements $v_2$, $a_0$, $a_1$ and $t_0$, which correspond to moments of the parton distribution functions. We work with the operators

$$\mathcal{O}_{v_2} = \frac{1}{2}\,\bar{q}\left(\gamma_4 \overleftrightarrow{D}_4 - \frac{1}{3}\left(\gamma_1 \overleftrightarrow{D}_1 + \gamma_2 \overleftrightarrow{D}_2 + \gamma_3 \overleftrightarrow{D}_3\right)\right) q \quad , \tag{4.31}$$

$$\mathcal{O}_{a_0} = \bar{q}\gamma_2\gamma_5 q \quad , \tag{4.32}$$

$$\mathcal{O}_{a_1} = \frac{1}{4}\,\bar{q}\left(\gamma_4\gamma_5 \overleftrightarrow{D}_2 + \gamma_2\gamma_5 \overleftrightarrow{D}_4\right) q \quad , \tag{4.33}$$

$$\mathcal{O}_{t_0} = \bar{q}\sigma_{24}\gamma_5 q \quad . \tag{4.34}$$

To compute the matrix elements of these operators, we look at the ratio of the corresponding three- and two-point functions

$$R = \frac{\Gamma^s_{\beta\alpha}\langle B_\alpha \mathcal{O} \bar{B}_\beta\rangle}{\tilde{\Gamma}^s_{\beta\alpha}\langle B_\alpha \bar{B}_\beta\rangle} \tag{4.35}$$

and hope to find the plateau. There are two properties which make the $\Lambda$ different from the proton, the wave function and the different quark mass of the strange quark. As interpolating fields we use

$$\begin{aligned} B_\alpha(t,\mathbf{p}) &= \sum_{\substack{x\\ x_4=t}} \mathrm{e}^{-\mathrm{i}\mathbf{p}\cdot\mathbf{x}} \epsilon_{ijk}\, s^i_\alpha(x)\, u^j_\beta(x)\, \hat{C}_{\beta\gamma}\, d^k_\gamma(x) \\ \bar{B}_\alpha(t,\mathbf{p}) &= \sum_{\substack{x\\ x_4=t}} \mathrm{e}^{\mathrm{i}\mathbf{p}\cdot\mathbf{x}} \epsilon_{ijk}\, \bar{d}^i_\beta(x)\, \hat{C}_{\beta\gamma}\, \bar{u}^j_\gamma(x)\, \bar{s}^k_\alpha(x) \end{aligned} \tag{4.36}$$

with $\hat{C} = C\gamma_5$. The quark fields in the interpolating fields Eq. (4.36) are smeared with the Jacobi method, see Sec. 3.2.3, to get a good overlap with the ground state. Furthermore, we use different quark masses for the $s$ quarks and the light $u$ and $d$ quarks. The mass of the $s$ is in nature between 80 MeV and 155 MeV [G$^+$00] whereas the light quark masses are $\approx 5$ MeV. Thus the physical strange quark mass is in the range of the quark masses which we can simulate.

The results are based on $\sim 140$ Wilson gauge configurations with $\beta = 6.0$ on a $16^3 \times 32$ lattice. We use clover improved Wilson fermions, see Sec. 1.6.3, with a non-perturbatively determined clover coefficient $c_{\mathrm{SW}} = 1.769$. To study the flavor symmetry breaking effects, we work with nine combinations of the hopping parameter $\kappa$, i.e., three different values $\kappa_s$ and $\kappa_d = \kappa_u$ for the strange and non-strange quarks respectively. So each quark mass can have three different physical values, which have been determined previously [Ple99]. For $\kappa = 0.1324$, 0.1333, and 0.1342 this leads to quark masses of approximately 166 MeV, 112 MeV, and $\approx 58$ MeV, respectively. We have to extrapolate in the light quark mass to the chiral limit. But we can, thus, interpolate in the strange quark mass to get the physical result.

To be consistent with the clover improvement, the operators have to be improved too. Only then, the $\mathcal{O}(a)$ terms are cancelled. The improvement for, e.g. the axial-vector, has the following form

$$A_\mu^{imp} = (1 + b_A am)(A_\mu + ac_a \partial_\mu P) \ . \tag{4.37}$$

The form is similar for the other operators. Only the improvement operators (here $\partial_\mu P$) differ as well as the value of $b$. However, the coefficients of the improvement operators are of order $g^2$, i.e. small. We neglect these contributions in the following and include only the factor $(1 + b_{\mathcal{O}} am)$ with $b_{\mathcal{O}}$ determined from tadpole improved perturbation theory.

To get from the ratios $R$ to the reduced matrix elements, one has to take into account the normalization of the hadron states in Eq. (4.12). Each quark field is multiplied by $\sqrt{2\kappa}$ to get the correct continuum normalization. With the renormalization constants $Z$ this leads to the following formulae [G$^+$96b, G$^+$97]

$$R_{v_{2,b}} = -\frac{1}{Z_{v_{2,b}}(1 + b_{v_{2,b}} am)} \frac{1}{2\kappa} \frac{E^2 + \frac{1}{3}\mathbf{p}^2}{E} v_{2,b} \ , \tag{4.38}$$

$$R_{a_0} = \frac{\mathrm{i}}{Z_{a_0}(1 + b_{a_0} am)} \frac{1}{2\kappa} \frac{m}{2E} a_0 \ , \tag{4.39}$$

$$R_{a_1} = -\frac{\mathrm{i}}{Z_{a_1}(1 + b_{a_1} am)} \frac{1}{2\kappa} \frac{m}{4} a_1 \ , \tag{4.40}$$

$$R_{t_0} = \frac{1}{Z_{t_0}(1 + b_{t_0} am)} \frac{1}{2\kappa} \frac{1}{2} t_0 \ . \tag{4.41}$$

The renormalization constants have been calculated in a variant of tadpole im-

proved perturbation theory [QCDSF, QCDSF02a, QCDSF02b].[4]

$$Z_{v_{2b}}(\mu^2 = 4\ \mathrm{GeV}^2, \beta = 6.0) = 1.11106 \qquad b_{v_{2b}} = 1.25803 \tag{4.42}$$

$$Z_{a_0}(\beta = 6.0) = 0.83232 \qquad b_{a_0} = 1.27134 \tag{4.43}$$

$$Z_{a_1}(\mu^2 = 4\ \mathrm{GeV}^2, \beta = 6.0) = 1.11800 \qquad b_{a_1} = 1.24313 \tag{4.44}$$

$$Z_{t_0}(\mu^2 = 4\ \mathrm{GeV}^2, \beta = 6.0) = 0.88924 \qquad b_{t_0} = 1.24626 \tag{4.45}$$

These results are obtained, first, in renormalization group invariant form (accurate to two loop perturbation theory) and then converted back to the $\overline{MS}$-scheme at $\mu^2$=4 GeV$^2$, using two-loop perturbation theory for $t_0$ and three-loop perturbation theory for $a_1$ and $v_2$ [C$^+$01b]. $Z_{a_0}^{\overline{\mathrm{MS}}}$ has been determined non-perturbatively in [BGLS01], too

$$Z_{a_0} = 0.807(2)(8) \qquad b_{a_0} = 1.28(3)(4) \tag{4.46}$$

which deviates for our parameters by $\approx 4\%$ from the perturbative value in Eq. (4.43).

### 4.3.2 Determination of the physical $\kappa_s$

Whereas the critical hopping parameter $\kappa_\mathrm{c} = 0.1352$ — to which the light quark mass has to be extrapolated — has been determined previously, we have to set the value for the strange quark $\kappa_s^*$ ourselves. We choose $\kappa_\mathrm{s}^*$ such that the spectrum of light strange hadrons is reproduced.

The lightest particle containing a strange quark is the kaon $K$. We compute the square of its mass for the nine different combinations of $\kappa_d$ and $\kappa_s$. The lattice constant was determined previously via the Sommer parameter. We get nine values for the kaon mass, see Fig. 4.5 on the left. For each $\kappa_s$ we extrapolated the three masses with different $\kappa_d$ to the chiral limit. This extrapolation is done linearly in $1/\kappa_d$ (the dotted lines in Fig. 4.5). This results in three values with $\kappa_d = \kappa_\mathrm{c}$. The interpolation of these values to the experimental mass of the kaon $m_K = 493.7$ MeV yields $\kappa_s^* = 0.1341$.

The second particle is the $\Lambda$ itself. In general, the baryon masses from quenched simulations turn out to be too heavy, but ratios and differences have reasonable values. We consider the ratio of the $\Lambda$ mass to the proton mass. This has the advantage that we do not need to rely on an external scale setting. So we compute the square of the $\Lambda$ mass for the nine combinations of $\kappa_d$ and $\kappa_s$ and divide each of these by the square of the proton mass in the chiral limit, see Fig. 4.5 on the right. Again we extrapolate in $1/\kappa_d$ to the chiral limit and interpolate in $1/\kappa_s$. The physical value of $(m_\Lambda/m_p)^2 = 1.42$ translates to $\kappa_s^* = 0.1342$.

The two values for $\kappa_s^*$ are in pretty good agreement. So the final result for the matrix elements is always closely above the smallest value for $1/\kappa_s$, i.e. the

[4]The author is indebted to M. Göckeler for the communication of the numbers.

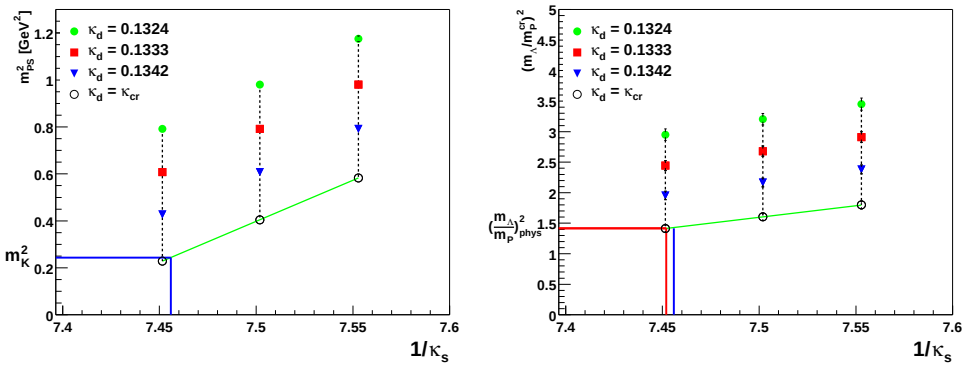


Figure 4.5: Left: The square of the kaon mass as a function of $1/\kappa_s$. For each $\kappa_s$ the three measurements for the three values of $\kappa_d$ are connected by dotted lines and linearly extrapolated to the chiral limit in $1/\kappa_d$. The resulting three values are interpolated to match the physical kaon mass. This gives the $\kappa_s^* = 0.1341$. Right: Same for the square of the ratio $m_\Lambda/m_p$. The nucleon mass is taken in the chiral limit. The $\kappa_s^*$ agrees with the previous result.

smallest quark mass. Let us finally discuss the flavor symmetry breaking. The points on the diagonal $\kappa_d = \kappa_s$ are flavor symmetric. The more the other six points spread, the larger is the flavor symmetry breaking. For the masses this breaking is quite large, see Fig. 4.5.

### 4.3.3 Results

In this section, we show results for the first two moments of the spin structure functions, the first non-trivial moment of the unpolarized structure function, and the tensor matrix element related to transversity. For higher moments of these structure functions the quality of the plateaus doesn't match our requirements. We do not take into account the clover improvement operators as their coefficients are small and some of them are hard to determine.

#### The spin content: $a_0$

The spin content of the $\Lambda$ hyperon is in the focus of our investigation. By Eq. (4.18) it is given up to a factor of two by the reduced matrix element $a_0$. At first we get nine plateaus, which can be seen in Fig. 4.6. The source is at time slice 0, the sink at $t = 13$. The time slice $\tau$ in which the operator is located is varied. We determine the plateaus in a range $5 \leq \tau < 10$ with a $\chi^2$ fit. The results of this fit are shown in Fig. 4.7, the numbers can be found in Table 4.1. For a fixed $\kappa_s$ the three values are extrapolated linearly in $1/\kappa_d$ to the chiral limit $1/\kappa_c$ — analogous to the masses. The error of the extrapolated value is deter-

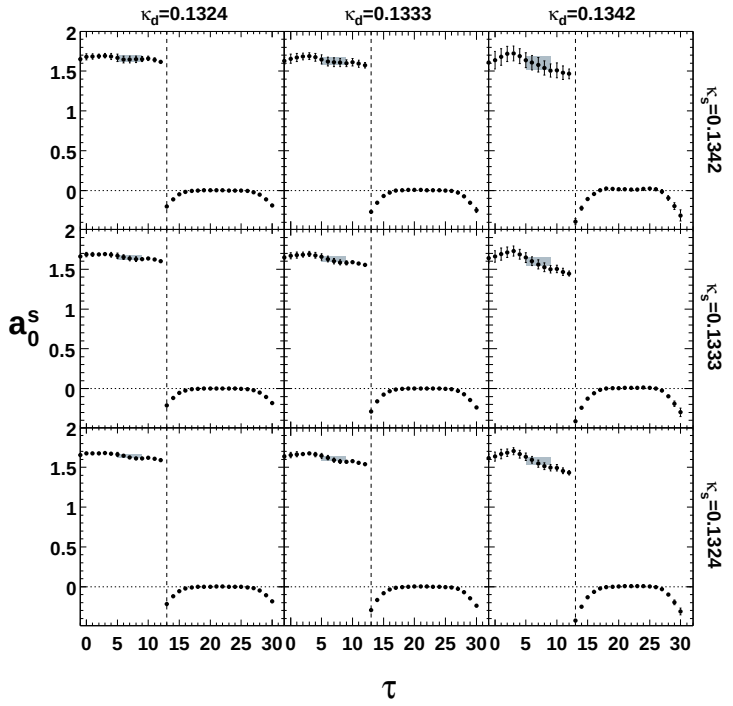


Figure 4.6: The nine plateaus for $a_0^s$. The $\Lambda$ source is at 0 the sink is at $t = 13$. On the $x$ axis is the operator position $\tau$. For $\tau > t$ the three-point function is exponentially suppressed. Heavier quarks give better signals, i.e., for $\kappa_d = \kappa_s = 0.1324$ which translates to $m_q \approx 170$ MeV. For lighter quarks (in the upper right corner) the errors get larger. The flavor symmetry breaking effects are small. The grey boxes denote the $1\sigma$ band of the fitted values; the fit range is $5 \leq \tau < 10$.

mined by the jackknife method, see App. C. The result is interpolated linearly to $1/\kappa_s^*$. The error of this value is, again, a jackknife error.

For the contribution of the $s$ and $d$ quarks to the spin of the $\Lambda$ we find using the non-perturbative renormalization constants from Eq. (4.46)

$$\Delta d = \frac{1}{2} a_0^d = -\,0.02 \pm 0.04 \qquad \Delta s = \frac{1}{2} a_0^s = 0.68 \pm 0.04\ . \tag{4.47}$$

Thus, the $s$ quark carries most of the $\Lambda$'s spin. The light quarks carry almost none.

In contrast to the situation for the masses, flavor symmetry works well for this matrix element. In Fig. 4.7 we see that there is almost no deviation from the mass diagonal elements. The different masses of the light and $s$ quarks have almost no impact on the spin content. To get a feeling for the result, let us compare it to specific models. We take a value from the naïve quark

| $\kappa_d$ | $\kappa_s$ | $a_0^d$ | $a_0^s$ | $a_1^d$ | $a_1^s$ |
|---|---|---|---|---|---|
| 0.1324 | 0.1324 | −0.02(1) | 1.64(2) | 0.014(4) | 0.350(7) |
| 0.1333 | 0.1324 | −0.02(2) | 1.65(3) | 0.019(5) | 0.378(9) |
| 0.1342 | 0.1324 | −0.05(4) | 1.66(4) | 0.027(7) | 0.42(2) |
| 0.1324 | 0.1333 | −0.01(2) | 1.61(3) | 0.017(4) | 0.321(8) |
| 0.1333 | 0.1333 | −0.02(3) | 1.63(3) | 0.024(6) | 0.35(1) |
| 0.1342 | 0.1333 | −0.05(5) | 1.63(5) | 0.037(9) | 0.39(2) |
| 0.1324 | 0.1342 | −0.00(3) | 1.58(4) | 0.022(6) | 0.29(1) |
| 0.1333 | 0.1342 | −0.01(5) | 1.59(6) | 0.032(7) | 0.32(2) |
| 0.1342 | 0.1342 | −0.05(7) | 1.60(9) | 0.051(12) | 0.33(3) |
| $\kappa_c$ | 0.1324 | −0.05(4) | 1.67(5) | 0.03(1) | 0.45(2) |
| $\kappa_c$ | 0.1333 | −0.05(6) | 1.64(6) | 0.05(1) | 0.42(2) |
| $\kappa_c$ | 0.1342 | −0.06(10) | 1.61(10) | 0.06(2) | 0.38(3) |
| $\kappa_c$ | $\kappa_s^*$ | −0.06(9) | 1.62(9) | 0.06(2) | 0.39(3) |

Table 4.1: Measured bare values for $a_0$ and $a_1$

| $\kappa_d$ | $\kappa_s$ | $v_2^d$ | $v_2^s$ | $t_0^d$ | $t_0^s$ |
|---|---|---|---|---|---|
| 0.1324 | 0.1324 | 0.188(2) | 0.207(3) | 0.02(1) | 1.58(2) |
| 0.1333 | 0.1324 | 0.179(3) | 0.223(4) | 0.02(1) | 1.60(3) |
| 0.1342 | 0.1324 | 0.169(5) | 0.244(5) | 0.04(2) | 1.61(3) |
| 0.1324 | 0.1333 | 0.194(3) | 0.193(4) | 0.03(1) | 1.57(3) |
| 0.1333 | 0.1333 | 0.186(4) | 0.209(4) | 0.03(1) | 1.58(3) |
| 0.1342 | 0.1333 | 0.177(7) | 0.230(6) | 0.05(3) | 1.59(4) |
| 0.1324 | 0.1342 | 0.202(3) | 0.177(5) | 0.03(1) | 1.55(5) |
| 0.1333 | 0.1342 | 0.195(4) | 0.192(6) | 0.04(2) | 1.57(6) |
| 0.1342 | 0.1342 | 0.188(9) | 0.213(9) | 0.08(4) | 1.57(8) |
| $\kappa_c$ | 0.1324 | 0.159(7) | 0.262(6) | 0.04(3) | 1.62(4) |
| $\kappa_c$ | 0.1333 | 0.168(8) | 0.248(7) | 0.06(4) | 1.61(5) |
| $\kappa_c$ | 0.1342 | 0.180(11) | 0.229(10) | 0.08(5) | 1.59(10) |
| $\kappa_c$ | $\kappa_s^*$ | 0.178(10) | 0.233(10) | 0.08(5) | 1.59(8) |

Table 4.2: Measured bare values for $v_2$ and $t_0$

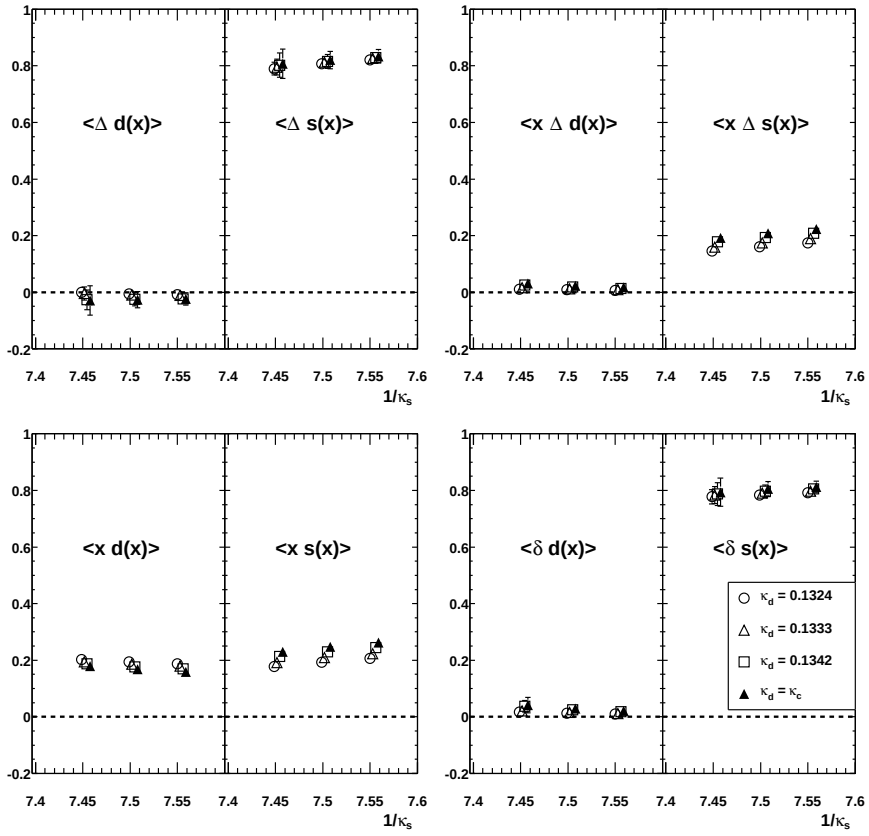


Figure 4.7: The chiral extrapolation for the four moments. On the left of each plot the result for the $d$ quarks, on the right for the $s$ quarks. In the top left plot the spin contribution $\Delta q$ is shown. The symmetry breaking effects are small. In the lower left plot we see the momentum fraction where symmetry breaking is stronger. On the right the second moment of the polarized structure function and the tensor charge are plotted.

model and the one computed under the assumption of SU(3) flavor symmetry from experimental and Monte Carlo proton data. For the experimental data, both, the full and the valence distribution are taken from Ashery and Lipkin [AL00]. As we work in the quenched approximation, the comparison to the valence data is natural. In hindsight, the SU(3) rotation of experimental data has to work well for this matrix element as SU(3) breaking effects are small. The different approaches are summarized in Table 4.3. Our result is quite close to the experimental value for the valence distribution. This might be a consequence of the quenched approximation where the sea quarks are explicitly neglected.

| | $\Delta d$ | $\Delta s$ |
|---|---|---|
| quark model | 0 | 1 |
| exp. + SU(3) | -0.17(3) | 0.63(3) |
| exp. (val) + SU(3) | -0.07(4) | 0.73(4) |
| MC + SU(3) | -0.16(9) | 0.65(2) |
| this work | -0.02(4) | 0.68(4) |

Table 4.3: Comparison of the $\Lambda$ spin structure from the different approaches.

**Momentum:** $v_2$

The reduced matrix element $v_2^{(f)}$ gives the first non-trivial moment of the unpolarized structure functions. It can be interpreted as the average momentum contribution of quarks of flavor $f$ to a high energy $\Lambda$. From the bottom left plot of Fig. 4.7 and Table 4.2 we learn that light and strange quarks contribute to the momentum by the same order of magnitude. Also the dependence on the quark mass can be understood. For fixed $d$ quark mass the contribution of the $s$ quark is larger for larger quark mass. If the $d$ quark mass is decreased, $\langle x \rangle$ increases for the $s$ quarks. The results for the $d$ are analogous. Including the renormalization constant we find

$$\langle x \rangle^d = v_{2b}^d = 0.20 \pm 0.01 \qquad \langle x \rangle^s = v_{2b}^s = 0.27 \pm 0.02 \ . \tag{4.48}$$

**Spin structure: The second moment** $a_1$

The second moment of the polarized parton distribution is given by

$$a_1^f = 2\langle x \Delta q(x) \rangle^f \ . \tag{4.49}$$

The results are collected in Fig. 4.7 in the top right plot and Table 4.1. The renormalized result at $\kappa_d = \kappa_c$ and $\kappa_s = \kappa_s^*$ is

$$a_1^d = 0.07 \pm 0.02 \qquad a_1^s = 0.45 \pm 0.04 \quad . \tag{4.50}$$

**The tensor charge**

Finally, let us present the results for the tensor charge $t_0 = 2\delta q$ in Fig. 4.7 (bottom, right) and Table 4.2. In the heavy quark limit it should be the same as $a_0$. This is confirmed by our simulation. The flavor symmetry breaking is again tiny. The matrix element is almost independent of, both, the $s$ and the $d$ quark mass. We get as final renormalized result

$$t_0^d = 0.07 \pm 0.04 \qquad t_0^s = 1.47 \pm 0.08 \quad . \tag{4.51}$$

### 4.3.4 Summary

We have computed moments of the $\Lambda$ hyperon quark distribution functions. In four of the matrix elements we had reasonably good signals, i.e., in the first and second moment of the polarized distribution function, the second moment of the unpolarized one and for the tensor charge. We found a good agreement of the spin fraction carried by the light and the $s$ quarks with phenomenological models. But there are significant systematic uncertainties:

- The quenched approximation neglects the sea quarks. It might, therefore, be advisable to compare our results to valence quark distributions.
- We use Wilson fermions which explicitly break chiral symmetry. The effect of this is unknown. The clover improvement should help, but for matrix elements it seems to be not as successful as for masses.
- The chiral extrapolation is done linearly. For small quark masses, chiral logarithms might significantly contribute. This effect is not under control, yet.
- The quark line disconnected contributions are neglected. One might argue that this is consistent with the quenched approximation. But for a complete analysis one has to solve the difficult task of computing it.
- We could not attempt a continuum extrapolation $a \to 0$ as we simulated only for one lattice spacing. But previous results for the proton have shown that this uncertainty is smaller than the other systematic errors.

The main goal was to study the flavor symmetry breaking effects in the matrix elements. Whereas these are large for the masses, the matrix elements themselves have a much weaker dependence on the different quark masses. So one can hope that — even in full QCD, with better fermions and better extrapolation — the application of a flavor SU(3) rotation on the proton structure into the $\Lambda$ structure leads to reasonable estimates.

## 4.4 Four-quark operators on the lattice

Until now we have studied the leading twist structure functions. They are related to matrix elements of two-fermion operators. To get further insight into the proton structure structure, higher correlators are interesting. Here, we want to learn more about four-fermion operators. These are of higher twist, i.e., they contribute with $1/Q^2$ to the structure functions. This makes them very hard to access experimentally. As the leading twist part of the structure function depends logarithmically on $Q^2$, it is difficult to disentangle it from the higher twist part, which has a $1/Q^2$ dependence on top of a logarithmic one.

On the other side, there exist phenomenological models, e.g., diquark based models or the chiral soliton model which make predictions for these correlators. Predictions based on large $N_c$ arguments exist too [LPPG01]. So any further knowledge is appreciated to check these.

Unfortunately, it is very difficult to compute these operators on the lattice. Contrary to the leading twist case, where mixing with lower dimensional operators becomes an issue only for the higher moments, all the relevant four-fermion operators suffer from it. On dimensional grounds these are accompanied by a coefficient which includes a power of $1/a$, which causes problems in the continuum limit. This implies that the mixing is not calculable in perturbation theory. As a first step, we circumvent this by choosing operators which cannot mix with lower dimensional ones. These have no immediate physical applications but can provide an indication of the magnitude of four-fermion matrix elements.

The section is organized as follows. In Section 4.4.1, we explain the problem of mixing in more detail. Then we present the operators which are free of the mixing with lower dimensional operators in Sec. 4.4.2. The details of the simulation are presented in Sec. 4.4.3. We give the results for the two sets of operators in Sections 4.4.4 and 4.4.5 and a short summary and outlook in Sec. 4.4.5.

### 4.4.1 Mixing

We have seen in Section 4.1 that the moments of the structure function $F_2(x, Q^2)$ can be related to the forward matrix elements of local operators in the nucleon. The twist of these operators gives the power with which these matrix elements contribute in the $1/Q^2$ expansion of the structure function. To leading twist the lowest moment is given by the matrix element of the operator

$$\mathcal{O}_{\mu\nu} = \frac{\mathrm{i}}{2}\bar{\psi}G^2\gamma_\mu\overleftrightarrow{D}_\nu\psi \tag{4.52}$$

where $G$ represents the flavor structure in question. Its contribution is quantified — after using the Poincaré invariance of the theory — by the reduced matrix element $A_2^{(2)}$, given by

$$\langle p|\mathcal{O}_{\{\mu\nu\}} - \text{trace}|p\rangle = 2A_2^{(2)}(p_\mu p_\nu - \text{trace}) \tag{4.53}$$

The Wilson coefficient, with which it contributes is to leading order, is given by $1+O(g^2)$. This has now to be compared to the higher twist four-fermion operator which we are interested in.

In particular, the twist four, spin two matrix element $A_2^{(4)}$ is given by (indices in $\{\dots\}$ are symmetrized)

$$\frac{1}{2}\sum_s \langle p,s|A^c_{\{\mu\nu\}} - \text{trace}|p,s\rangle \equiv \langle p|A^c_{\{\mu\nu\}} - \text{trace}|p\rangle = 2A_2^{(4)}(p_\mu p_\nu - \text{trace}) \tag{4.54}$$

with the four-quark operator

$$A^c_{\mu\nu} = (\bar{\psi} G \gamma_\mu \gamma_5 t^a \psi)(\bar{\psi} G \gamma_\nu \gamma_5 t^a \psi) \tag{4.55}$$

The operators (4.55) and (4.52) transform identically under Lorentz transformations, but (4.55) has dimension six, whereas (4.52) has only dimension four: four-quark operators will in general mix with two-quark operators of lower dimension. This fact complicates the investigation of four-quark operators, because the mixing with lower-dimensional operators cannot be calculated reliably within perturbation theory. A non-perturbative computation in lattice QCD could proceed along the same lines as in the case of the twist three matrix element $d_2$ [G$^+$01]. For the time being, we do not attempt such a non-perturbative calculation of the renormalization and mixing coefficients of four-quark operators. Instead we restrict ourselves to cases where mixing with lower-dimensional operators is prohibited by flavor symmetry. The results presented presented in this section were previously published in Refs. [C$^+$01a, G$^+$02d].

### 4.4.2 Operators

To avoid the mixing between the twist four operators and lower dimensional twist two operators in the pion, the authors of [C$^+$00] have used operators with isospin $I = 2$. As a single quark carries isospin $I = 1/2$ a two-quark operator cannot build up $I = 2$. Thus, mixing is prohibited by flavor symmetry. This works for the pion as it is an isospin $I = 1$ particle. Because the proton has $I = 1/2$, the $I = 2$ operator vanishes. However, we can use a similar trick if we extend the flavor symmetry group from the $\mathrm{SU(2)_F}$ isospin symmetry to $\mathrm{SU(3)_F}$, i.e., we assume three quarks of the same mass. The flavor structure of our operator in the OPE is now

$$\mathcal{O} = (e_u \bar{u} u + e_d \bar{d} d + e_s \bar{s} s)(e_u \bar{u} u + e_d \bar{d} d + e_s \bar{s} s)\,. \tag{4.56}$$

While two-quark operators transform under $\mathrm{SU(3)_F}$ according to $\overline{\mathbf{3}} \otimes \mathbf{3} = \mathbf{1} \oplus \mathbf{8}$, we have for four-quark operators: $(\overline{\mathbf{3}} \otimes \mathbf{3}) \otimes (\overline{\mathbf{3}} \otimes \mathbf{3}) = 2 \cdot \mathbf{1} \oplus 4 \cdot \mathbf{8} \oplus \mathbf{10} \oplus \overline{\mathbf{10}} \oplus \mathbf{27}$. Four-quark operators with $I = 0, 1$, $I_3 = 0$, and hypercharge $Y = 0$ belonging to the multiplets $\mathbf{10}$, $\overline{\mathbf{10}}$, $\mathbf{27}$ do not mix with two-quark operators and do not automatically vanish in a proton expectation value. The operators belonging to the $\mathbf{27}$ multiplet are (giving only the flavor structure)

$$\begin{aligned} \mathcal{O}^{I=1}_{\mathbf{27}} =& \frac{1}{10}(e_u^2 - e_d^2 - 2e_u e_s + 2e_d e_s)[(\bar{u}u)(\bar{u}u) - (\bar{d}d)(\bar{d}d) \\ & - (\bar{u}s)(\bar{s}u) - (\bar{s}u)(\bar{u}s) + (\bar{d}s)(\bar{s}d) + (\bar{s}d)(\bar{d}s) \\ & - (\bar{s}s)(\bar{u}u) - (\bar{u}u)(\bar{s}s) + (\bar{s}s)(\bar{d}d) + (\bar{d}d)(\bar{s}s)]\,, \end{aligned} \tag{4.57}$$

$$\begin{aligned}\mathcal{O}_{\mathbf{27}}^{I=0} =&\frac{1}{60}(e_u^2+e_d^2+e_ue_d-3e_ue_s-3e_de_s+3e_s^2)\\ &[2(\bar{u}u)(\bar{u}u)+2(\bar{d}d)(\bar{d}d)+(\bar{d}d)(\bar{u}u)+(\bar{d}u)(\bar{u}d)\\ &+(\bar{u}d)(\bar{d}u)+(\bar{u}u)(\bar{d}d)-3(\bar{u}s)(\bar{s}u)-3(\bar{s}u)(\bar{u}s)\\ &-3(\bar{d}s)(\bar{s}d)-3(\bar{s}d)(\bar{d}s)-3(\bar{s}s)(\bar{u}u)-3(\bar{u}u)(\bar{s}s)\\ &-3(\bar{s}s)(\bar{d}d)-3(\bar{d}d)(\bar{s}s)+6(\bar{s}s)(\bar{s}s)]\ .\end{aligned} \tag{4.58}$$

Inserting the values of the quark charges one finds

$$e_u^2-e_d^2-2e_ue_s+2e_de_s=e_u^2+e_d^2+e_ue_d-3e_ue_s-3e_de_s+3e_s^2=1\ . \tag{4.59}$$

As the operators belong to the same multiplet, the Wigner-Eckart theorem tells us that the proton matrix elements of these two operators are proportional to each other:

$$\langle P|\mathcal{O}_{\mathbf{27}}^{I=0}|P\rangle=\frac{1}{2}\langle P|\mathcal{O}_{\mathbf{27}}^{I=1}|P\rangle\,. \tag{4.60}$$

Furthermore, the Wigner-Eckart theorem relates proton matrix elements to neutron matrix elements. Thus our results can easily be rephrased in terms of neutron expectation values. However, unless otherwise stated, we shall only present the proton results. The operators of multiplets **10** and $\overline{\mathbf{10}}$ read

$$\begin{aligned}\mathcal{O}_{\mathbf{10}}^{I=1} =&(\bar{d}d)(\bar{u}u)-(\bar{d}u)(\bar{u}d)+(\bar{u}d)(\bar{d}u)-(\bar{u}u)(\bar{d}d)\\ &+(\bar{u}u)(\bar{s}s)+(\bar{d}s)(\bar{s}d)-(\bar{d}d)(\bar{s}s)-(\bar{u}s)(\bar{s}u)\\ &-(\bar{s}d)(\bar{d}s)+(\bar{s}u)(\bar{u}s)+(\bar{s}s)(\bar{d}d)-(\bar{s}s)(\bar{u}u)\ ,\end{aligned} \tag{4.61}$$

$$\begin{aligned}\mathcal{O}_{\overline{\mathbf{10}}}^{I=1} =&(\bar{d}d)(\bar{u}u)+(\bar{d}u)(\bar{u}d)-(\bar{u}d)(\bar{d}u)-(\bar{u}u)(\bar{d}d)\\ &+(\bar{u}u)(\bar{s}s)-(\bar{d}s)(\bar{s}d)-(\bar{d}d)(\bar{s}s)+(\bar{u}s)(\bar{s}u)\\ &+(\bar{s}d)(\bar{d}s)-(\bar{s}u)(\bar{u}s)+(\bar{s}s)(\bar{d}d)-(\bar{s}s)(\bar{u}u)\ .\end{aligned} \tag{4.62}$$

As these are antisymmetric with respect to the interchange of the two quark–anti-quark pairs, they do not appear in the flavor decomposition of the OPE operator (4.56).

In Fig. 4.8, the three types of contributions to a general three-point function in a baryon are plotted. The two graphs in the first row are the ones that give rise to the mixing with lower dimensional two-fermion operators. However, we have chosen the operators such that these two contributions cancel. So we are left with the type of contribution in the lower row.

The propagator is diagonal in flavor space. As the proton is a *uud* state, only some of the terms in the operators contribute to proton matrix elements, e.g., the $(\bar{d}d)(\bar{d}d)$ terms and those containing $s$ quarks vanish. Therefore, the expectation

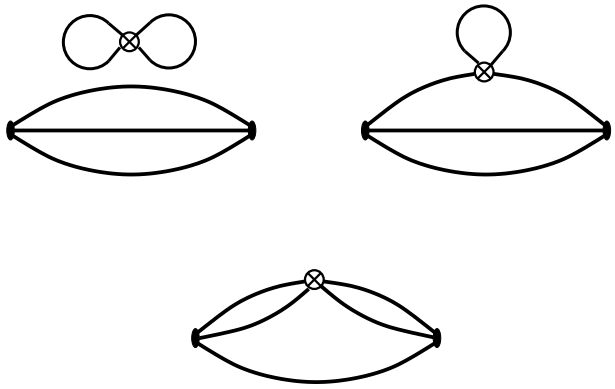

Figure 4.8: The three types of contributions to the three-point function of a four-fermion operator in a baryon. In our calculations we had an operator such that the two contributions on top cancelled and we were left with the lower diagram.

values of the operators (4.57), (4.61), (4.62) reduce to

$$\begin{aligned}
\langle P|\mathcal{O}^{I=1}_{\mathbf{27}}|P\rangle &= \frac{1}{10}\langle P|(\bar{u}u)(\bar{u}u)|P\rangle\Big|^{\mathbf{27}}\,,\\
\langle P,S|\mathcal{O}^{I=1}_{\mathbf{10}}|P,S\rangle &= \langle P,S|(\bar{d}d)(\bar{u}u)-(\bar{d}u)(\bar{u}d)+(\bar{u}d)(\bar{d}u)-(\bar{u}u)(\bar{d}d)|P,S\rangle\Big|^{\mathbf{10}}\,,\\
\langle P,S|\mathcal{O}^{I=1}_{\overline{\mathbf{10}}}|P,S\rangle &= \langle P,S|(\bar{d}d)(\bar{u}u)+(\bar{d}u)(\bar{u}d)-(\bar{u}d)(\bar{d}u)-(\bar{u}u)(\bar{d}d)|P,S\rangle\Big|^{\overline{\mathbf{10}}}\,.
\end{aligned} \tag{4.63}$$

### 4.4.3 Technical details

We use an ensemble of quenched configurations generated with the Wilson gauge action at $\beta = 6.0$ on a $16^3 \times 32$ lattice. This corresponds to a lattice constant of $a = 0.093$ fm or $a^{-1} = 2.12$ GeV [G$^+$01], which is obtained under the assumption of $r_0 = 0.5$ fm. We don't attempt a continuum extrapolation. But this $\beta$ has proven to give reasonable results with the errors of the other approximations in mind. We simulate Wilson fermions at three different values of the hopping parameter $\kappa$, which determines the quark mass. For $\kappa = 0.1515$, 0.1530, and 0.1545 we have a physical quark mass of roughly 190 MeV, 130 MeV and 90 MeV, respectively. We extrapolated our results linearly in $1/\kappa$ to the chiral limit, i.e. to $1/\kappa = 1/\kappa_c = 6.3642$. An example of such an extrapolation of a matrix element is shown in Fig. 4.9. This is motivated by the perturbative relation Eq. (1.49), i.e., that the quark mass goes linearly in $1/\kappa$ to zero as this approaches $1/\kappa_c$. As it is in general advisable to extrapolate dimensionless quantities, we divide the matrix elements by $m_p^4$ before the extrapolation.

The matrix elements are computed by the methods described in Section 4.2. Here, we keep the position of the operator $\tau = 5$ fixed and search for a plateau in the time-position of the sink $t$, see Eq. (4.27) and the discussion afterwards.

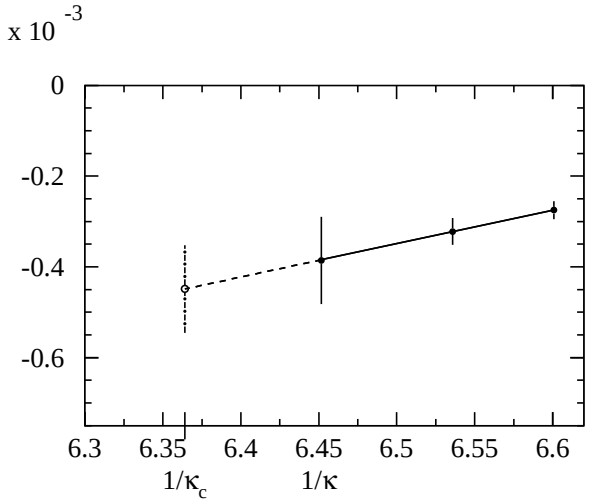


Figure 4.9: Chiral extrapolation of the bare proton matrix element of $\mathcal{O}_{\mathbf{27}}^{I=1}$ for the operator $V_{44}^c$ − trace (see Eq. (4.66)), divided by $m_p^4$.

The spatial momentum of the proton $\mathbf{P}$ is always zero. We fit the plateaus in the interval $11 \leq t \leq 17$. An example of the plateaus is plotted in Fig. 4.10.

The continuum proton states with momentum $P$ and spin vector $S$ are normalized such that

$$\langle P, S|P', S'\rangle = (2\pi)^3 2E_P \delta(\mathbf{P} - \mathbf{P}')\delta_{SS'} \tag{4.64}$$

In order to obtain the fields in the continuum normalization, we have to multiply each lattice quark field by $\sqrt{2\kappa}$. To normalize the states according to Eq. (4.64) we must multiply $R$ by an additional factor of $2m_p$.

### 4.4.4 Operators from the 27 multiplet

The twist four contribution in the $F_2$ structure function comes from the four-quark operator $A_{\mu\nu}^c$, see Eq. (4.55). In order to access the flavor-**27** component experimentally one has to combine the structure functions of several baryons ($p$, $n$, $\Lambda$, $\Sigma$, $\Xi$) in such a way as to project out the desired flavor combination, e.g.,

$$\begin{aligned}
\langle p|\mathcal{O}_{\mathbf{27}}^{I=1}|p\rangle &= \langle\Sigma^+|\mathcal{O}|\Sigma^+\rangle - 2\langle\Sigma^0|\mathcal{O}|\Sigma^0\rangle + \langle\Sigma^-|\mathcal{O}|\Sigma^-\rangle \\
&= -\langle\Sigma^+|\mathcal{O}|\Sigma^+\rangle - \langle\Sigma^-|\mathcal{O}|\Sigma^-\rangle \\
&\quad -6\langle\Lambda|\mathcal{O}|\Lambda\rangle + 2\langle\Xi^0|\mathcal{O}|\Xi^0\rangle + 2\langle\Xi^-|\mathcal{O}|\Xi^-\rangle \\
&\quad +2\langle p|\mathcal{O}|p\rangle + 2\langle n|\mathcal{O}|n\rangle\,.
\end{aligned} \tag{4.65}$$

Unfortunately, most of these terms will not be measured in the foreseeable future. A direct comparison with data is out of question. On the other hand, they can be

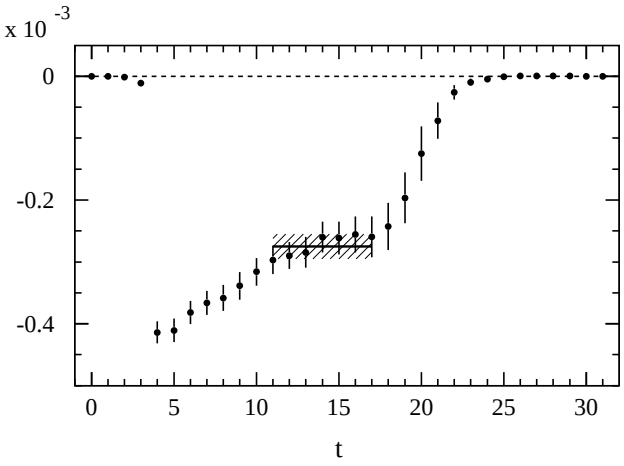


Figure 4.10: Plateau for the bare matrix element of $\mathcal{O}^{I=1}_{\mathbf{27}}$ for the operator $V^c_{44}$ − trace (see Eq. (4.66)), divided by $m_p^4$, with $\kappa = 0.1515$.

used as a testing ground for models of hadrons, taking the role of experimental data. Note that the **27** contribution can also be isolated by studying combinations of electromagnetic and weak structure functions [Got78].

Of course, we need to know the renormalized operators. Although, due to our choice of the flavor-**27** component, mixing with two-quark operators is absent, different four-quark operators may still mix under renormalization. We have to compute the matrix elements of the following operators (using the nomenclature introduced in Ref. [C$^+$00]):

$$\begin{aligned}
V^c_{\mu\nu} &= \bar{\psi} G \gamma_\mu t^a \psi \, \bar{\psi} G \gamma_\nu t^a \psi, \\
A^c_{\mu\nu} &= \bar{\psi} G \gamma_\mu \gamma_5 t^a \psi \, \bar{\psi} G \gamma_\nu \gamma_5 t^a \psi, \\
T^c_{\mu\nu} &= \bar{\psi} G \sigma_{\mu\rho} t^a \psi \, \bar{\psi} G \sigma_{\nu\rho} t^a \psi, \\
V_{\mu\nu} &= \bar{\psi} G \gamma_\mu \psi \, \bar{\psi} G \gamma_\nu \psi, \\
A_{\mu\nu} &= \bar{\psi} G \gamma_\mu \gamma_5 \psi \, \bar{\psi} G \gamma_\nu \gamma_5 \psi, \\
T_{\mu\nu} &= \bar{\psi} G \sigma_{\mu\rho} \psi \, \bar{\psi} G \sigma_{\nu\rho} \psi.
\end{aligned} \tag{4.66}$$

with $G$ the flavor matrix suitable to generate the flavor structures in Eq. (4.57), Eq. (4.61) and Eq. (4.62).

The bare expectation values divided by $m_p^4$ and extrapolated to the chiral limit are given in Table 4.4 for the spin two components, while the traces are given in Table 4.5. E.g. the number shown for the operator $A^c_{\mu\nu}$ − trace in Table 4.4 is what we obtain for $\langle P|\frac{1}{10}(\bar{u}\gamma_4\gamma_5 t^a u)(\bar{u}\gamma_4\gamma_5 t^a u) - \text{trace}|P\rangle/m_p^4$ in the chiral limit.

| operator | |
|---|---|
| $A^c_{\{\mu\nu\}}$ − trace | $(-0.9 \pm 0.8) \cdot 10^{-4}$ |
| $V^c_{\{\mu\nu\}}$ − trace | $(-4.5 \pm 1.0) \cdot 10^{-4}$ |
| $T^c_{\{\mu\nu\}}$ − trace | $(4.9 \pm 0.8) \cdot 10^{-4}$ |
| $A_{\{\mu\nu\}}$ − trace | $(-0.0 \pm 1.3) \cdot 10^{-4}$ |
| $V_{\{\mu\nu\}}$ − trace | $(8.4 \pm 1.4) \cdot 10^{-4}$ |
| $T_{\{\mu\nu\}}$ − trace | $(-4.6 \pm 1.9) \cdot 10^{-4}$ |

Table 4.4: Matrix elements of the spin two operators from the **27** multiplet, divided by $m_p^4$ and extrapolated to the chiral limit.

| Dirac structure | $t_a \otimes t_a$ | $1 \otimes 1$ |
|---|---|---|
| $\gamma_5 \otimes \gamma_5$ | $(2.8 \pm 0.7) \cdot 10^{-4}$ | $(-13.4 \pm 2.6) \cdot 10^{-4}$ |
| $1 \otimes 1$ | $(-7.1 \pm 1.2) \cdot 10^{-4}$ | $(17.8 \pm 2.9) \cdot 10^{-4}$ |
| $\gamma_\mu\gamma_5 \otimes \gamma_\mu\gamma_5$ | $(17.2 \pm 2.0) \cdot 10^{-4}$ | $(-12.1 \pm 3.9) \cdot 10^{-4}$ |
| $\gamma_\mu \otimes \gamma_\mu$ | $(-18.2 \pm 2.2) \cdot 10^{-4}$ | $(7.4 \pm 4.0) \cdot 10^{-4}$ |
| $\sigma_{\mu\nu} \otimes \sigma_{\mu\nu}$ | $(-4 \pm 7) \cdot 10^{-4}$ | $(17.6 \pm 9.6) \cdot 10^{-4}$ |

Table 4.5: Matrix elements of the spin zero operators from the **27** multiplet, divided by $m_p^4$ and extrapolated to the chiral limit.

We have checked that these operators fulfill their Fierz identities.

The renormalization constants have been calculated in one-loop perturbation theory [C+00]. The renormalized spin two piece of the operator $A^c_{\mu\nu}$ reads

$$\begin{aligned}\left[A^c_{\mu\nu}(\mu)\right]^{\text{ren}} = A^c_{\mu\nu} - \frac{g_0^2}{16\pi^2}\Big[ &(3\ln(a\mu) + 46.072285)\, A^c_{\mu\nu} \\ &+ \left(-\frac{8}{9}\ln(a\mu) + 0.083982\right) V_{\mu\nu} \\ &+ \left(-\frac{5}{3}\ln(a\mu) + 0.157467\right) V^c_{\mu\nu} \\ &- 1.071448\; T_{\mu\nu} - 2.008965\; T^c_{\mu\nu}\Big]\,,\end{aligned} \tag{4.67}$$

where $g_0$ is the bare coupling constant ($\beta \equiv 6/g_0^2$). The renormalization scale $\mu$ will be identified with the inverse lattice spacing $1/a$. In our simulations this has a value of $1/a \approx 2.12$ GeV (using $r_0 = 0.5$ fm to set the scale). In terms of the renormalized operator the reduced matrix element $A_2^{(4)}$ is then given by

$$\frac{1}{m_p^2} A_2^{(4)}\Big|^{\mathbf{27},\mathrm{I}=1} = \frac{2}{3}\frac{\langle P|\frac{1}{10}(\bar{u}\gamma_4\gamma_5 t^a u)(\bar{u}\gamma_4\gamma_5 t^a u) - \text{trace}|P\rangle}{m_p^4}\,, \tag{4.68}$$

and we obtain for the lowest moment of $F_2$ in our special flavor channel

$$\int_0^1 \mathrm{d}x\, F_2(x,Q^2)\big|^{\mathbf{27},I=1}_{\text{Nachtmann}} = -0.0005(5)\frac{m_p^2\alpha_s(Q^2)}{Q^2} + O(\alpha_s^2)\,, \tag{4.69}$$

where we take the Nachtmann moment [Nac73] to get rid of the target mass corrections. The analogous result for the neutron differs from the above only by the sign.

In the proton, the corresponding twist two contribution is about 0.14 at $Q^2 = 5$ GeV$^2$. As in the pion, the twist four correction is tiny. Our result may be compared with bag model estimates. In this model the scale for the prefactor in Eq. (4.69) is set by $B/m_p^4 \approx 0.0006$, where $B \approx (145\text{ MeV})^4$ is the bag constant. The factor $B/m_p^4$ is however multiplied by a relatively large (and negative) number [JS81].

It is rather difficult to determine the first moment of the higher-twist contribution to $F_2(x)$ experimentally. Phenomenological fits to the available data give a positive value of about 0.005(4) GeV$^2/Q^2$ [Ale01, CHKL93]. Our matrix element, which is due to its flavor structure only one contribution to the full moment, is considerably smaller than this phenomenological number.

### 4.4.5 Operators from the 10 and $\overline{\mathbf{10}}$ multiplets

Having found rather small matrix elements for our four-quark operators from the **27** one may ask if operators from the **10** or $\overline{\mathbf{10}}$ of SU(3)$_\mathrm{F}$ (although not contributing to $F_2$ in the OPE) have larger matrix elements. With the two possible color structures which can form color singlet operators, these operators are linear combinations of terms of the form $(\bar\psi G\,\Gamma t^a\psi)(\,\bar\psi G'\,\Gamma' t^a\psi)$ and $(\bar\psi G\,\Gamma\psi)(\,\bar\psi G'\,\Gamma'\psi)$, respectively, where $\Gamma$ and $\Gamma'$ are Dirac matrices. We have chosen the flavor matrices $G$, $G'$ such that we get the following flavor structures:

$$(\bar d d)(\bar u u) - (\bar u u)(\bar d d) \tag{4.70}$$

and

$$(\bar d u)(\bar u d) - (\bar u d)(\bar d u)\ . \tag{4.71}$$

These can be combined to yield the **10** and $\overline{\mathbf{10}}$ structures in Eq. (4.63).

Discrete symmetries impose restrictions on the matrix elements of these operators. We have

$$\langle P,S|\mathcal{O}|P,S\rangle^* = \langle P,-S|\mathcal{T}\mathcal{P}\mathcal{O}\mathcal{P}^{-1}\mathcal{T}^{-1}|P,-S\rangle = \langle P,S|\mathcal{O}^\dagger|P,S\rangle \tag{4.72}$$

where $\mathcal{P}$ is the parity and $\mathcal{T}$ is the time inversion operator. For the Dirac matrices used in our computations we define sign factors $s_1$, $s_1'$, $s_2$, and $s_2'$ by

$$\begin{array}{ccc} \gamma_4\Gamma^\dagger\gamma_4 = s_1\Gamma & , & \gamma_4\Gamma'^\dagger\gamma_4 = s_1'\Gamma'\ , \\ \gamma_4\gamma_5 C\Gamma^* C^{-1}\gamma_5\gamma_4 = s_2\Gamma & , & \gamma_4\gamma_5 C\Gamma'^* C^{-1}\gamma_5\gamma_4 = s_2'\Gamma'\,. \end{array} \tag{4.73}$$

Here $C$ is the charge conjugation matrix defined in Eq.(A.9). One more sign $\epsilon_{\mathcal{O}}$ is determined by

$$\langle P, -S|\mathcal{O}|P, -S\rangle = \epsilon_{\mathcal{O}}\langle P, S|\mathcal{O}|P, S\rangle \ . \tag{4.74}$$

From Eq. (4.72) we now get for the flavor structure (4.70)

$$\langle P, S|\mathcal{O}|P, S\rangle^* = \epsilon_{\mathcal{O}} s_2 s_2' \langle P, S|\mathcal{O}|P, S\rangle = s_1 s_1' \langle P, S|\mathcal{O}|P, S\rangle \tag{4.75}$$

and for the flavor structure (4.71)

$$\langle P, S|\mathcal{O}|P, S\rangle^* = \epsilon_{\mathcal{O}} s_2 s_2' \langle P, S|\mathcal{O}|P, S\rangle = -s_1 s_1' \langle P, S|\mathcal{O}|P, S\rangle \ . \tag{4.76}$$

Thus the matrix element $\langle P, S|\mathcal{O}|P, S\rangle$ is real if $\epsilon_{\mathcal{O}} s_2 s_2' = 1$ and purely imaginary if $\epsilon_{\mathcal{O}} s_2 s_2' = -1$; the matrix element vanishes if $\epsilon_{\mathcal{O}} s_2 s_2' = -s_1 s_1'$ for the flavor structure (4.70) or $\epsilon_{\mathcal{O}} s_2 s_2' = s_1 s_1'$ for the flavor structure (4.71). We have checked that these restrictions are satisfied by our results within statistical errors. We restrict ourselves in the following to the matrix elements which are not forced to be zero by the above relations. Note that for a given Dirac structure at most one of the flavor structures (4.70) and (4.71) yields a non-vanishing result.

The definite Lorentz transformation properties of our operators could be used to define reduced matrix elements, e.g., in Minkowski space one gets

$$\langle P, S|(\bar{d}\gamma_\mu\gamma_5 d)(\bar{u}\gamma_\nu\gamma_5 u) - (\bar{u}\gamma_\mu\gamma_5 u)(\bar{d}\gamma_\nu\gamma_5 d)|P, S\rangle = A\epsilon_{\mu\nu\alpha\beta}(P^\alpha S^\beta - S^\alpha P^\beta)\,. \tag{4.77}$$

Thus in this case the matrix element with $\mu = 1$, $\nu = 2$ and $S^\alpha = \delta_{\alpha 3}$ is equal to the one with $\mu = 2$, $\nu = 3$ and $S^\alpha = \delta_{\alpha 1}$. This holds only on average, so in order to increase the statistics we averaged over these matrix elements to reduce the statistical error. The bare expectation values divided by $m_p^4$ are given together with their statistical errors in Tables 4.6 and 4.7.

The order of magnitude of the results does not differ greatly from those found for the operators in the **27**. The renormalization constants for the **10** and $\overline{\mathbf{10}}$ operators are not known, but we do not expect that the renormalized operators have much larger matrix elements than the bare ones.

### 4.4.6 Summary

As a first attempt to compute four-fermion operators in the nucleon we have restricted ourselves to those which don't suffer from mixing with lower dimensional operators. Even though these matrix elements are not those which contribute to the structure function $F_2(x, Q^2)$, they can serve as a first estimate of the order of magnitude. The matrix elements are found to be small. This fits to the results from a perturbative analysis of the data, where the extracted higher twist has been reduced drastically by a better precision of the perturbative description of the leading twist part, see Sec. 4.1.2.

| Dirac structure | flavor | $t_a \otimes t_a$ | $1 \otimes 1$ |
|---|---|---|---|
| $1 \otimes \gamma_4$ | (4.70) | $(0.4 \pm 0.6) \cdot 10^{-3}$ | $(3.0 \pm 1.6) \cdot 10^{-3}$ |
| $\epsilon_{4\alpha\beta\delta}\gamma_\alpha\gamma_5 \otimes \sigma_{\beta\delta}$ | (4.70) | $(-5.6 \pm 2.8) \cdot 10^{-3}\mathrm{i}$ | $(5.9 \pm 3.6) \cdot 10^{-3}\mathrm{i}$ |
| $\gamma_5 \otimes \gamma_4\gamma_5$ | (4.71) | $(0.6 \pm 0.5) \cdot 10^{-3}$ | $(-3.3 \pm 1.8) \cdot 10^{-3}$ |
| $\gamma_\alpha \otimes \sigma_{4\alpha}$ | (4.71) | $(-3.1 \pm 1.2) \cdot 10^{-3}\mathrm{i}$ | $(0.1 \pm 1.9) \cdot 10^{-3}\mathrm{i}$ |

Table 4.6: Expectation values of operators with the flavor structures (4.70) and (4.71) in an unpolarized proton, divided by $m_p^4$ and extrapolated to the chiral limit.

| Dirac structure | flavor | $t_a \otimes t_a$ | $1 \otimes 1$ |
|---|---|---|---|
| $1 \otimes \gamma_3\gamma_5$ | (4.70) | $(-3.3 \pm 0.6) \cdot 10^{-3}\mathrm{i}$ | $(15.9 \pm 1.6) \cdot 10^{-3}\mathrm{i}$ |
| $1 \otimes \sigma_{21}$ | (4.70) | $(-4.1 \pm 0.6) \cdot 10^{-3}$ | $(10.7 \pm 1.8) \cdot 10^{-3}$ |
| $\gamma_5 \otimes \sigma_{43}$ | (4.70) | $(2.2 \pm 0.5) \cdot 10^{-3}$ | $(-4.4 \pm 1.3) \cdot 10^{-3}$ |
| $\gamma_4 \otimes \gamma_3\gamma_5 - \gamma_3 \otimes \gamma_4\gamma_5$ | (4.70) | $(-9.1 \pm 0.9) \cdot 10^{-3}\mathrm{i}$ | $(13.0 \pm 2.1) \cdot 10^{-3}\mathrm{i}$ |
| $\epsilon_{3\alpha\lambda\rho}\gamma_\alpha \otimes \sigma_{\lambda\rho}$ | (4.70) | $(42 \pm 4) \cdot 10^{-3}$ | $(-51 \pm 5) \cdot 10^{-3}$ |
| $\gamma_5 \otimes \gamma_3$ | (4.71) | $(4.9 \pm 0.5) \cdot 10^{-3}\mathrm{i}$ | $(-15.6 \pm 1.4) \cdot 10^{-3}\mathrm{i}$ |
| $\gamma_2 \otimes \gamma_1$ | (4.71) | $(2.4 \pm 0.5) \cdot 10^{-3}\mathrm{i}$ | $(-5.6 \pm 0.9) \cdot 10^{-3}\mathrm{i}$ |
| $\gamma_2\gamma_5 \otimes \gamma_1\gamma_5$ | (4.71) | $(6.1 \pm 0.8) \cdot 10^{-3}\mathrm{i}$ | $(-7.6 \pm 1.1) \cdot 10^{-3}\mathrm{i}$ |
| $\gamma_\alpha\gamma_5 \otimes \sigma_{3\alpha}$ | (4.71) | $(21.5 \pm 1.8) \cdot 10^{-3}$ | $(-19.2 \pm 2.6) \cdot 10^{-3}$ |
| $\sigma_{2\alpha} \otimes \sigma_{1\alpha}$ | (4.71) | $(-8.9 \pm 1.5) \cdot 10^{-3}\mathrm{i}$ | $(8.1 \pm 1.8) \cdot 10^{-3}\mathrm{i}$ |

Table 4.7: Expectation values of operators with the flavor structures (4.70) and (4.71) in a polarized proton ($\mathbf{S} = \mathbf{e}_3$), divided by $m_p^4$ and extrapolated to the chiral limit.

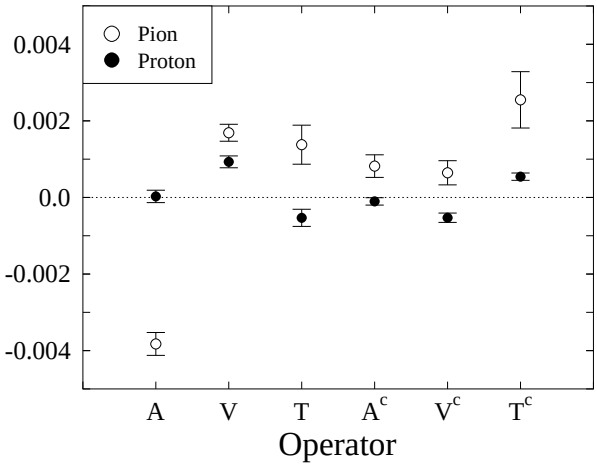


Figure 4.11: Renormalized four-quark matrix elements in the pion and in the proton (in lattice units).

Thus we arrive for the nucleon at a conclusion which is similar to what has been observed in the pion [C+00]. For a more detailed comparison we plot in Fig. 4.11 the renormalized pion matrix elements [C+00] with the flavor structure

$$\begin{aligned}\langle\pi^+|(\bar{u}u)(\bar{u}u) + (\bar{d}d)(\bar{d}d) - (\bar{u}u)(\bar{d}d) - (\bar{d}d)(\bar{u}u) \\ - (\bar{u}d)(\bar{d}u) - (\bar{d}u)(\bar{u}d)|\pi^+\rangle/m_{\rm PS}^2\end{aligned} \tag{4.78}$$

together with the corresponding renormalized matrix elements for the proton $\langle p|10\cdot\mathcal{O}_{\mathbf{27}}^{I=1}|p\rangle/m_p^2$ (in lattice units). We display the results for the spin two components setting $\mu=\nu=4$ (with the trace term subtracted). The normalization of the operators is chosen such that the flavor structure $(\bar{u}u)(\bar{u}u)$ appears with the factor 1 in both cases. (Alternatively, it may be remarked that $\mathrm{SU}(3)_{\rm F}$ makes the above pion matrix element equal to the expectation value of $10\cdot\mathcal{O}_{\mathbf{27}}^{I=1}$ in the meson-octet analogue of the proton, the $K^+$.) It is no great surprise that the numbers do not show many similarities — after all, the pion and the proton are very different particles. The largest difference seems to be in the axial-vector operators.

We have proven that, in principle, it is possible to compute four-fermion matrix elements with current computer power. But the full computation including the mixing with lower dimensional operators will remain a challenge for lattice QCD for the years to come.

# Chapter 5

# Summary and outlook

In the course of the preceding pages, several investigations concerning the non-perturbative structure of QCD have been presented. In the first chapter, we introduced the formulations of lattice QCD used throughout the rest of the work. We focused on the possibility to formulate chirality on the lattice, which has become feasible only a few years ago, by using Dirac operators that solve the Ginsparg-Wilson equation. As the exact solutions of this equation are very expensive with respect to computer time, we decided to use an approximate solution, the chirally improved Dirac operator. This allowed us to look into the mechanism of chiral symmetry breaking below and above the phase transition in great detail. We confirmed predictions of the standard instanton picture by examining low lying eigenmodes of the Dirac operator. We were able to demonstrate a strong localization of the near-zero modes together with a correlation between chirality and density. Furthermore, we wanted to see how this picture changes across the transition to the chirally symmetric phase. There we found signals for localized chiral excitations and interpreted our results such, that their density is not large enough to build up a chiral condensate.

Next we turned to hadronic observables, i.e., quantities which can be compared with experimental data. First, we used the chirally improved operator to compute the light meson masses along with the proton mass. We showed that the spectrum and dispersion relations are reproduced satisfactorily well. The scaling properties turned out to be good, too. This is important to know as it proves that the operator delivers reasonable results even at finite lattice spacing and volume. It is an indispensable requirement before one can use such an operator in the computation of experimentally less known quantities.

In the last chapter, we used the predictive power of lattice QCD to compute moments of structure functions inside the $\Lambda$ hyperon and the nucleon. For the $\Lambda$ hyperon, we computed the first moments of the polarized and unpolarized leading twist parton distributions. We looked in particular into flavor symmetry breaking effects. These turned out to be much smaller than for the masses.

Finally, we computed four-fermion matrix elements inside the proton. Un-

fortunately, the problem of operator mixing is far from being solved for such complicated operators. We had to limit ourselves to operators that are save from mixing with lower dimensional ones. However, these do not contribute to the proton structure function. We were able to demonstrate the feasibility to compute these operators and we hope that the results give a hint for the typical size of these matrix elements. We found them to be small which is consistent with our extractions from experimental data.

Until now, the results from lattice QCD do not exactly reproduce the experimental values. As we have to make several approximations due to limited computer resources, this is not surprising. Today, we have to apply at least one of the major approximations, namely the quenched approximation or the explicit breaking of chiral symmetry. However, the difference between dynamical and quenched simulations is significant only at small quark masses. We proved that we can simulate small pion masses with an approximate solution to the Ginsparg-Wilson equation. Using this operator in a dynamical simulation can, thus, be a next step into the direction of a complete solution of QCD under continuum conditions.

# Appendix A

# Definitions

Lattice QCD is formulated in Euclidean space-time. The metric tensor in Minkowski space $g_{\mu\nu}$ is therefore replaced by the Euclidean metric $\delta_{\mu\nu}$

$$\delta_{\mu\nu} = \begin{cases} 1 & \mu = \nu \\ 0 & \mu \neq \nu \end{cases} \tag{A.1}$$

with $\mu, \nu = 1, \ldots, 4$. Usually, indices that appear twice in an expression are summed over. We use the convention that the time is in the 4 direction.

## A.1 Dirac matrices

The Dirac matrices $\gamma_\mu$ ($\mu = 1, \ldots, 4$) are hermitian $4 \times 4$ matrices which in Euclidean space fulfill the commutation relation

$$\{\gamma_\mu, \gamma_\nu\} = 2\delta_{\mu\nu} \ . \tag{A.2}$$

We use for our calculations with the chirally improved Dirac operator the following representation of the Dirac matrices

$$\begin{aligned} \gamma_1 &= \begin{pmatrix} 0 & 0 & 0 & -1 \\ 0 & 0 & 1 & 0 \\ 0 & 1 & 0 & 0 \\ -1 & 0 & 0 & 0 \end{pmatrix} \quad \gamma_2 = \begin{pmatrix} 0 & 0 & -i & 0 \\ 0 & 0 & 0 & i \\ i & 0 & 0 & 0 \\ 0 & -i & 0 & 0 \end{pmatrix} \\ \gamma_3 &= \begin{pmatrix} 0 & 0 & 1 & 0 \\ 0 & 0 & 0 & 1 \\ 1 & 0 & 0 & 0 \\ 0 & 1 & 0 & 0 \end{pmatrix} \quad \gamma_4 = \begin{pmatrix} 0 & 0 & 0 & -i \\ 0 & 0 & -i & 0 \\ 0 & i & 0 & 0 \\ i & 0 & 0 & 0 \end{pmatrix} \end{aligned} \tag{A.3}$$

and define $\gamma_5$ as

$$\gamma_5 = \gamma_1\gamma_2\gamma_3\gamma_4 = \begin{pmatrix} 1 & 0 & 0 & 0 \\ 0 & 1 & 0 & 0 \\ 0 & 0 & -1 & 0 \\ 0 & 0 & 0 & -1 \end{pmatrix} . \tag{A.4}$$

Note that $\gamma_5$ anticommutes with all Dirac matrices

$$\{\gamma_5, \gamma_\mu\} = 0 . \tag{A.5}$$

The commutators of the Dirac matrices define the $\sigma_{\mu\nu}$ matrices by

$$\sigma_{\mu\nu} = -\frac{i}{2}[\gamma_\mu, \gamma_\nu] . \tag{A.6}$$

By definition $\sigma_{\mu\nu}$ is anti-symmetric in $\mu$ and $\nu$. Thus it vanishes if $\mu = \nu$. We are left with 6 independent $\sigma$ matrices.

A basis for the $4 \times 4$ matrices is given by the following set of 16 matrices:

$$\{1, \gamma_\mu, \sigma_{\mu\nu}, \gamma_5\gamma_\mu, \gamma_5\} \tag{A.7}$$

To specify their symmetry these are called the *scalar*, *vector*, *tensor*, *axial-vector* and *pseudoscalar* components, respectively. This leads to the following abbreviation for the set (A.7)

$$\{S, V_\mu, T_{\mu\nu}, A_\mu, P\} . \tag{A.8}$$

The charge conjugation matrix $C$ is defined by its property

$$C\gamma_\mu^{\mathrm{T}}C^{-1} = -\gamma_\mu . \tag{A.9}$$

It is representation dependent and has a certain arbitrariness. We use for the computations with the chirally improved operator

$$C = i\gamma_1\gamma_3 . \tag{A.10}$$

## A.2 The Gell-Mann matrices

The generators of the su($n$) algebra are denoted by $t_a$. They are hermitian $n \times n$ matrices

$$\mathrm{tr}\, t_a = 0 , \qquad t_a^+ = t_a \tag{A.11}$$

and fulfill the following normalization and commutation relations

$$\mathrm{tr}\, t_a t_b \;=\; \frac{1}{2}\delta_{ab}[t_a, t_b] = i f_{abc} t_c . \tag{A.12}$$

The structure constants $f_{abc}$ are completely antisymmetric in the indices and real. The Gell-Mann matrices are usually defined as

$$t_a = \frac{\lambda_a}{2} \tag{A.13}$$

and the completeness relation reads

$$\sum_{a=1}^{N^2-1} (\lambda_a)_{cd}(\lambda_a)_{ef} = 2(\delta_{cf}\delta_{de} - \frac{1}{N}\delta_{cd}\delta_{ef}) \ . \tag{A.14}$$

For $N = 3$ the usual representation of the $N^2 - 1$ generators is:

$$\lambda_1 = \begin{pmatrix} 0 & 1 & 0 \\ 1 & 0 & 0 \\ 0 & 0 & 0 \end{pmatrix} \quad \lambda_2 = \begin{pmatrix} 0 & -i & 0 \\ i & 0 & 0 \\ 0 & 0 & 0 \end{pmatrix} \quad \lambda_3 = \begin{pmatrix} 1 & 0 & 0 \\ 0 & -1 & 0 \\ 0 & 0 & 0 \end{pmatrix}$$

$$\lambda_4 = \begin{pmatrix} 0 & 0 & 1 \\ 0 & 0 & 0 \\ 1 & 0 & 0 \end{pmatrix} \quad \lambda_5 = \begin{pmatrix} 0 & 0 & -i \\ 0 & 0 & 0 \\ i & 0 & 0 \end{pmatrix} \quad \lambda_6 = \begin{pmatrix} 0 & 0 & 0 \\ 0 & 0 & 1 \\ 0 & 1 & 0 \end{pmatrix}$$

$$\lambda_7 = \begin{pmatrix} 0 & 0 & 0 \\ 0 & 0 & -i \\ 0 & i & 0 \end{pmatrix} \quad \lambda_8 = \begin{pmatrix} \frac{1}{\sqrt{3}} & 0 & 0 \\ 0 & \frac{1}{\sqrt{3}} & 0 \\ 0 & 0 & \frac{-2}{\sqrt{3}} \end{pmatrix} \tag{A.15}$$

# Appendix B

# Detailed specification of the chirally improved Dirac operator

In this appendix, we describe in more detail the terms in chirally improved Dirac operator and give the values for the coefficients which we use for the seven ensembles of quenched gauge field configurations.

As has been pointed out in Section 1.6.5, the most general Dirac operator $D$ can be expanded in the series (1.60). Each term in this series is characterized by three pieces: A generator of the Clifford algebra, a group of paths and a real coefficient. The paths within a group can have different signs which are determined by the symmetries, C, P, $\gamma_5$-hermiticity and rotation invariance. The symmetries also determine which paths are grouped together. Thus it is sufficient to characterize a group of paths by a single generating path and all the other paths in the group as well as their relative sign factors can be determined by applying the symmetries.

In addition, for the vector and tensor terms appearing in our $D$ it is sufficient to give the paths only for one vector (tensor) since rotation invariance immediately fixes the structure for the other vector (tensor) terms. In order to describe our $D$, we start with listing the three determining pieces for each term in Table B.1. In Table B.2 we list the values of the coefficients $s_i, v_i, t_i$, and $p_1$ for the different values of the inverse gauge coupling $\beta_1$ for the ensembles used in this work.

| Clifford generator | Generating path | Name of coefficient |
|---|---|---|
| $\mathbb{1}$ | $<>$ | $s_1$ |
| $\mathbb{1}$ | $<1>$ | $s_2$ |
| $\mathbb{1}$ | $<1,2>$ | $s_3$ |
| $\mathbb{1}$ | $<1,2,3>$ | $s_5$ |
| $\mathbb{1}$ | $<1,1,2>$ | $s_6$ |
| $\mathbb{1}$ | $<1,2,-1>$ | $s_8$ |
| $\mathbb{1}$ | $<1,2,3,4>$ | $s_{10}$ |
| $\mathbb{1}$ | $<1,2,-1,3>$ | $s_{11}$ |
| $\mathbb{1}$ | $<1,2,-1,-2>$ | $s_{13}$ |
| $\gamma_1$ | $<1>$ | $v_1$ |
| $\gamma_1$ | $<1,2>$ | $v_2$ |
| $\gamma_1$ | $<1,2,3>$ | $v_4$ |
| $\gamma_1$ | $<2,1,3>$ | $v_5$ |
| $\gamma_1\gamma_2$ | $<1,2>$ | $t_1$ |
| $\gamma_1\gamma_2$ | $<1,2,3>$ | $t_2$ |
| $\gamma_1\gamma_2$ | $<1,3,2>$ | $t_3$ |
| $\gamma_1\gamma_2$ | $<1,2,-1>$ | $t_5$ |
| $\gamma_1\gamma_2$ | $<1,2,-1,-2>$ | $t_{15}$ |
| $\gamma_5$ | $<1,2,3,4>$ | $p_1$ |

Table B.1: Description of the terms in our $D$.

| | $\beta_1 = 7.90$ | $\beta_1 = 8.10$ | $\beta_1 = 8.20$ | $\beta_1 = 8.30$ | $\beta_1 = 8.35$ | $\beta_1 = 8.45$ | $\beta_1 = 8.70$ |
|---|---|---|---|---|---|---|---|
| $s_1$ | +1.437291 | +1.54498 | +1.54590 | +1.54688 | +1.42655 | +1.54737 | +1.42300 |
| $s_2$ | −0.044551 | −0.06169 | −0.06063 | −0.05997 | −0.04295 | −0.05892 | −0.04244 |
| $s_3$ | −0.013933 | −0.01448 | −0.01449 | −0.01448 | −0.01368 | −0.01451 | −0.01361 |
| $s_5$ | −0.001870 | −0.00262 | −0.00258 | −0.00255 | −0.00180 | −0.00251 | −0.00178 |
| $s_6$ | +0.001856 | +0.00220 | +0.00215 | +0.00210 | +0.00179 | +0.00206 | +0.00177 |
| $s_8$ | −0.003323 | −0.00540 | −0.00534 | −0.00532 | −0.00318 | −0.00525 | −0.00315 |
| $s_{10}$ | −0.000440 | −0.00053 | −0.00052 | −0.00051 | −0.00042 | −0.00050 | −0.00042 |
| $s_{11}$ | −0.000844 | −0.00118 | −0.00117 | −0.00117 | −0.00081 | −0.00116 | −0.00081 |
| $s_{13}$ | +0.006939 | +0.00780 | +0.00778 | +0.00777 | +0.00678 | +0.00775 | +0.00673 |
| $v_1$ | +0.234488 | +0.10975 | +0.11083 | +0.11063 | +0.24195 | +0.11240 | +0.24433 |
| $v_2$ | +0.005570 | +0.01770 | +0.01724 | +0.01707 | +0.00510 | +0.01654 | +0.00497 |
| $v_4$ | +0.004069 | +0.00744 | +0.00767 | +0.00784 | +0.00383 | +0.00804 | +0.00376 |
| $v_5$ | +0.001295 | +0.00182 | +0.00193 | +0.00198 | +0.00120 | +0.00209 | +0.00118 |
| $t_1$ | −0.079693 | −0.09874 | −0.09862 | −0.09860 | −0.07771 | −0.09843 | −0.07706 |
| $t_2$ | −0.002148 | −0.00309 | −0.00303 | −0.00299 | −0.00206 | −0.00292 | −0.00204 |
| $t_3$ | +0.001843 | +0.00227 | +0.00224 | +0.00221 | +0.00178 | +0.00218 | +0.00177 |
| $t_5$ | −0.004706 | −0.00663 | −0.00651 | −0.00641 | −0.00453 | −0.00627 | −0.00447 |
| $t_{15}$ | −0.003118 | −0.00361 | −0.00358 | −0.00356 | −0.00304 | −0.00354 | −0.00302 |
| $p_1$ | −0.007402 | −0.00911 | −0.00907 | −0.00905 | −0.00722 | −0.00901 | −0.00715 |

Table B.2: The numerical values of the coefficients $s_i, v_i$, $t_i$ and $p_1$ for the different gauge ensembles of the Lüscher-Weisz action. The gauge fields are modified by the HYP blocking for $\beta_1 = 7.90$, 8.35, and 8.70.

# Appendix C

# Error analysis

In lattice QCD, we usually generate $N$ gauge configurations and measure on them the quantities we are interested in. There are two types of quantities. First, there are primary quantities which can be measured on a single configuration, e.g., the expectation value of the plaquette or the Polyakov loop. Let us denote these individual measurements by $A_i$ with $i = 1, \ldots, N$. Their expectation value is given by the average $\bar{A}$ over the individual measurements. The error is the variance $\sigma$ divided by $\sqrt{N-1}$.

$$\begin{aligned} \bar{A} &= \frac{1}{N}\sum_{i=1}^{N} A_i \\ \sigma^2 &= \frac{1}{N}\sum_{i=1}^{N}(A_i - \bar{A})^2 = \frac{1}{N}(\sum_{i=1}^{N} A_i^2) - \bar{A}^2 \\ \Delta A &= \sqrt{\frac{\sigma^2}{N-1}} \end{aligned} \tag{C.1}$$

These formulae hold only if there is no correlation between the different values $A_i$. If the measurements are correlated, we have to include a correlation matrix in the average.

Now we turn to the so-called secondary quantities. These are observables which can only be determined from a set of configurations, e.g., a mass is extracted by fitting an exponential to a two-point function. This two-point function is given by the average over the ensemble. To give the error of this quantity the *jackknife* method is employed. We look at various subensembles, each of which consists of the complete ensemble from which some consecutive configurations have been removed. We measure our observable on each of these subensembles. From this method we profit twofold. First we get a more stable estimate for the central value by averaging over the results for the subensembles. The error of this average is proportional to the variation of the single measurements.

To be more precise, we generate the jackknife subensembles from the $N$ configurations by leaving out $n$ consecutive configurations. If $n$ is a divisor of $N$, we

get $N_{\rm sub} \equiv N/n$ subensembles. On each of them, we can measure the secondary quantity $B_i$.

| quantity | is measured on configurations |
|---|---|
| $B_1$ | $\{n+1,\ n+2, \ldots, N\}$ |
| $B_2$ | $\{1,\ 2, \ldots,\ n,\ 2n+1,\ 2n+2, \ldots, N\}$ |
| $B_3$ | $\{1,\ 2, \ldots,\ 2n,\ 3n+1,\ 2n+2, \ldots, N\}$ |
| $\vdots$ | $\vdots$ |
| $B_{N_{\rm sub}}$ | $\{1,\ 2, \ldots,\ N-n\}$ |

Given these $N_{\rm sub}$ values $B_i$, we can define the jackknife average $\bar{B}$ and the jackknife error $\Delta B$ are given by

$$\begin{aligned} \bar{B} =& \frac{1}{N_{\rm sub}} \sum_{i=1}^{N_{\rm sub}} B_i \\ \Delta B \equiv& \sqrt{\frac{N_{\rm sub}-1}{N_{\rm sub}} \sum_{i=1}^{N_{\rm sub}} (B_i - \bar{B})^2} \quad . \end{aligned} \tag{C.2}$$

For primary quantities these formulae reduce for $n = 1$ to the formulae given in Eq. (C.1).

One studies the jackknife error for different numbers of excluded $n$. If there are correlations in the observable between subsequent subsets, the jackknife error grows with larger numbers of $n$. In a typical case it grows from $n = 1$ to $n = 3$ then it remains rather constant. If $n$ gets too large and $N_{\rm sub}$ gets to small, the error of the error becomes large. Then we do not get a reliable estimate of the error. As a rule of thumb, we get a good estimate of the error if we choose $n = N/10$. In our simulations the configurations are well enough decorrelated such that there is no significant change in the error from $n = 1$ to $n = 2$. For further information on resampling methods see, e.g., [Efr82].

# Bibliography


[ADL+95] M. G. Alford, W. Dimm, G. P. Lepage, G. Hockney and P. B. Mackenzie, *Lattice QCD on small computers*, Phys. Lett. **B361**, 87–94 (1995), hep-lat/9507010.

[AGJ+94] C. Alexandrou, S. Güsken, F. Jegerlehner, K. Schilling and R. Sommer, *The Static approximation of heavy - light quark systems: A systematic lattice study*, Nucl. Phys. **B414**, 815–855 (1994), hep-lat/9211042.

[AL00] D. Ashery and H. J. Lipkin, *The contribution of $\Sigma^* \to \Lambda\pi$ to measured $\Lambda$ polarization*, (2000), hep-ph/0002144.

[Ale99] S. I. Alekhin, *On the value of $\alpha_s$ from the analysis of the SLAC/BCDMS deep inelastic scattering data*, Phys. Rev. **D59**, 114016 (1999), hep-ph/9809544.

[Ale00] S. I. Alekhin, *The QCD renormalization scale stability of high twists and $\alpha_s$ in deep inelastic scattering*, Phys. Lett. **B488**, 187–193 (2000), hep-ph/9912484.

[Ale01] S. I. Alekhin, *Global fit to the charged leptons DIS data: $\alpha_s$, parton distributions, and high twists*, Phys. Rev. **D63**, 094022 (2001), hep-ph/0011002.

[ALEPH96] D. Buskulic et al. (ALEPH Collaboration), *Measurement of Lambda polarization from Z decays*, Phys. Lett. **B374**, 319–330 (1996).

[ALPHA98] M. Guagnelli, R. Sommer and H. Wittig (ALPHA Collaboration), *Precision computation of a low-energy reference scale in quenched lattice QCD*, Nucl. Phys. **B535**, 389–402 (1998), hep-lat/9806005.

[B+97] C. Best et al., *Pion and rho structure functions from lattice QCD*, Phys. Rev. **D56**, 2743–2754 (1997), hep-lat/9703014.

[B+00] T. Blum et al., *Quenched lattice QCD with domain wall fermions and the chiral limit*, (2000), hep-lat/0007038.

[B+02] T. Blum et al., *Chirality correlation within Dirac eigenvectors from domain wall fermions*, Phys. Rev. **D65**, 014504 (2002), hep-lat/0105006.

[BB+98] M. E. Berbenni-Bitsch et al., *Crossover to non-universal microscopic spectral fluctuations in lattice gauge theory*, Phys. Lett. **B438**, 14–20 (1998), hep-ph/9804439.

[BBMS+98] M. E. Berbenni-Bitsch, S. Meyer, A. Schäfer, J. J. M. Verbaarschot and T. Wettig, *Microscopic universality in the spectrum of the lattice Dirac operator*, Phys. Rev. Lett. **80**, 1146–1149 (1998), hep-lat/9704018.

[BC80] T. Banks and A. Casher, *Chiral symmetry breaking in confining theories.*, Nucl. Phys. **B169**, 103 (1980).

[BCDMS89] A. C. Benvenuti et al. (BCDMS Collaboration), *A high statistics measurement of the proton structure functions $F_2(x, Q^2)$ and r from deep inelastic muon scattering at high $Q^2$*, Phys. Lett. **B223**, 485 (1989).

[BDET00] W. Bardeen, A. Duncan, E. Eichten and H. Thacker, *Anomalous chiral behavior in quenched lattice QCD*, Phys. Rev. **D62**, 114505 (2000), hep-lat/0007010.

[BG92] C. W. Bernard and M. F. L. Golterman, *Chiral perturbation theory for the quenched approximation of QCD*, Phys. Rev. **D46**, 853–857 (1992), hep-lat/9204007.

[BGLS01] T. Bhattacharya, R. Gupta, W.-J. Lee and S. R. Sharpe, *Order a improved renormalization constants*, Phys. Rev. **D63**, 074505 (2001), hep-lat/0009038.

[BJ93] M. Burkardt and R. L. Jaffe, *Polarized $q \to \Lambda$ fragmentation functions from $e^+e^- \to \Lambda + X$*, Phys. Rev. Lett. **70**, 2537–2540 (1993), hep-ph/9302232.

[BPST75] A. A. Belavin, A. M. Polyakov, A. S. Shvarts and Y. S. Tyupkin, *Pseudoparticle solutions of the Yang-Mills equations*, Phys. Lett. **B59**, 85–87 (1975).

[C+00] S. Capitani et al., *Higher-twist contribution to pion structure function: 4-Fermi operators*, Nucl. Phys. **B570**, 393–406 (2000), hep-lat/9908011.

[C+01a] S. Capitani et al., *Four-quark operators in hadrons*, Nucl. Phys. Proc. Suppl. **94**, 299–302 (2001), hep-lat/0010043.

[C+01b] S. Capitani et al., *Renormalisation and off-shell improvement in lattice perturbation theory*, Nucl. Phys. **B593**, 183–228 (2001), hep-lat/0007004.

[CGHN94] M. C. Chu, J. M. Grandy, S. Huang and J. W. Negele, *Evidence for the role of instantons in hadron structure from lattice QCD*, Phys. Rev. **D49**, 6039–6050 (1994), hep-lat/9312071.

[CH02] T.-W. Chiu and T.-H. Hsieh, *Quenched chiral logarithms in lattice QCD with exact chiral symmetry*, (2002), hep-lat/0204009.

[CHKL93] S. Choi, T. Hatsuda, Y. Koike and S. H. Lee, *Twist four matrix elements of the nucleon from recent DIS data at CERN and SLAC*, Phys. Lett. **B312**, 351–357 (1993), hep-ph/9303272.

[CMP83] G. Curci, P. Menotti and G. Paffuti, *Symanzik's improved Lagrangian for lattice gauge theory*, Phys. Lett. **B130**, 205 (1983), [Erratum-ibid. B **135** (1983) 516].

[CP-PACS02] S. Aoki et al. (CP-PACS Collaboration), *Light hadron spectrum and quark masses from quenched lattice QCD*, (2002), hep-lat/0206009.

[Cre87] M. Creutz, *Overrelaxation and Monte Carlo simulation*, Phys. Rev. **D36**, 515 (1987).

[D+02a] S. J. Dong et al., *Chiral properties of pseudoscalar mesons on a quenched $20^4$ lattice with overlap fermions*, Phys. Rev. **D65**, 054507 (2002), hep-lat/0108020.

[D+02b] T. Draper et al., *Quenched chiral log and light quark mass from overlap fermions*, (2002), hep-lat/0208045.

[Das97] A. K. Das, *Finite temperature field theory*, World Scientific, Singapore, Singapore, 1997.

[DDH+02a] S. J. Dong, T. Draper, I. Horváth, F. X. Lee and J. B. Zhang, *Pion decay constant, $Z_A$ and chiral log from overlap fermions*, Nucl. Phys. Proc. Suppl. **106**, 341–343 (2002), hep-lat/0110220.

[DDH+02b] S.-J. Dong, T. Draper, I. Horváth, F. Lee and J.-b. Zhang, *Quenched chiral behavior of hadrons with overlap fermions*, Nucl. Phys. Proc. Suppl. **106**, 275–277 (2002), hep-lat/0110044.

[DH02] T. DeGrand and A. Hasenfratz, *Density peaks and chiral peaks of fermion eigenmodes in QCD*, Phys. Rev. **D65**, 014503 (2002).

[DHK99] P. H. Damgaard, U. M. Heller and A. Krasnitz, *Microscopic spectral density of the Dirac operator in quenched QCD*, Phys. Lett. **B445**, 366–370 (1999), hep-lat/9810060.

[DPW96] D. Diakonov, M. V. Polyakov and C. Weiss, *Hadronic matrix elements of gluon operators in the instanton vacuum*, Nucl. Phys. **B461**, 539–580 (1996), hep-ph/9510232.

[Efr82] B. Efron, *The jackknife, the bootstrap, and other resampling plans*, Society for Industrial and Applied Mathematics, Philadelphia, 1982.

[EH02] R. G. Edwards and U. M. Heller, *Are topological charge fluctuations in QCD instanton dominated?*, Phys. Rev. **D65**, 014505 (2002), hep-lat/0105004.

[EHK98] R. G. Edwards, U. M. Heller and T. R. Klassen, *The effectiveness of non-perturbative $\mathcal{O}(a)$ improvement in lattice QCD*, Phys. Rev. Lett. **80**, 3448–3451 (1998), hep-lat/9711052.

[EHKN99] R. G. Edwards, U. M. Heller, J. E. Kiskis and R. Narayanan, *Quark spectra, topology and random matrix theory*, Phys. Rev. Lett. **82**, 4188–4191 (1999), hep-th/9902117.

[ESW96] R. K. Ellis, W. J. Stirling and B. R. Webber, *QCD and collider physics*, Cambridge Monogr. Part. Phys. Nucl. Phys. Cosmol. **8**, 1–435 (1996).

[FLS+85] I. A. Fox, M. L. Laursen, G. Schierholz, J. P. Gilchrist and M. Göckeler, *A classical instanton on a four-dimensional periodic lattice*, Phys. Lett. **B158**, 332 (1985).

[FNG+95] A. Frommer, B. Nockel, S. Güsken, T. Lippert and K. Schilling, *Many masses on one stroke: Economic computation of quark propagators*, Int. J. Mod. Phys. **C6**, 627–638 (1995), hep-lat/9504020.

[FS95] V. Furman and Y. Shamir, *Axial symmetries in lattice QCD with Kaplan fermions*, Nucl. Phys. **B439**, 54–78 (1995), hep-lat/9405004.

[G+96a] M. Göckeler et al., *Lattice operators for moments of the structure functions and their transformation under the hypercubic group*, Phys. Rev. **D54**, 5705–5714 (1996), hep-lat/9602029.

[G+96b] M. Göckeler et al., *Polarized and unpolarized nucleon structure functions from lattice QCD*, Phys. Rev. **D53**, 2317–2325 (1996), hep-lat/9508004.

[G+97] M. Göckeler et al., *A lattice determination of the second moment of the polarised valence quark distribution*, Phys. Lett. **B414**, 340–346 (1997), hep-ph/9708270.

[G+00] D. E. Groom et al., *Review of Particle Physics*, The European Physical Journal **C15**, 1+ (2000).

[G+01] M. Göckeler et al., *A lattice calculation of the nucleon's spin-dependent structure function $g_2$ revisited*, Phys. Rev. **D63**, 074506 (2001), hep-lat/0011091.

[G+02a] C. Gattringer et al., *Quenched QCD with fixed-point and chirally improved fermions*, (2002), hep-lat/0209099.

[G+02b] C. Gattringer et al., *Chirally improved Dirac operators: Studying the sensitivity to topological excitations for zero and finite temperature*, Nucl. Phys. Proc. Suppl. **106**, 551–559 (2002), hep-lat/0110015.

[G+02c] M. Göckeler et al., *Applied lattice gauge calculations: Diquark content of the nucleon*, (2002), hep-lat/0208008.

[G+02d] M. Göckeler et al., *A lattice evaluation of four quark operators in the nucleon*, Nucl. Phys. **B623**, 287–300 (2002), hep-lat/0103038.

[Gat01] C. Gattringer, *A new approach to Ginsparg-Wilson fermions*, Phys. Rev. **D63**, 114501 (2001), hep-lat/0003005.

[GGL+01] C. Gattringer, M. Göckeler, C. B. Lang, P. E. L. Rakow and A. Schäfer, *Comparing lattice Dirac operators in smooth instanton backgrounds*, Phys. Lett. **B522**, 194–200 (2001), hep-lat/0108001.

[GGR+01a] C. Gattringer, M. Göckeler, P. E. L. Rakow, S. Schaefer and A. Schäfer, *A comprehensive picture of topological excitations in finite temperature lattice QCD*, Nucl. Phys. **B618**, 205–240 (2001), hep-lat/0105023.

[GGR+01b] C. Gattringer, M. Göckeler, P. E. L. Rakow, S. Schaefer and A. Schäfer, *Properties of near zero modes and chiral symmetry breaking*, Nucl. Phys. **B617**, 101–116 (2001), hep-lat/0107016.

[GH00] C. Gattringer and I. Hip, *New approximate solutions of the Ginsparg-Wilson equation: Tests in 2-d*, Phys. Lett. **B480**, 112–118 (2000), hep-lat/0002002.

[GHL01] C. Gattringer, I. Hip and C. B. Lang, *Approximate Ginsparg-Wilson fermions: A first test*, Nucl. Phys. **B597**, 451–474 (2001), hep-lat/0007042.

[GHR+99] M. Göckeler, H. Hehl, P. E. L. Rakow, A. Schäfer and T. Wettig, *Small eigenvalues of the SU(3) Dirac operator on the lattice and in random matrix theory*, Phys. Rev. **D59**, 094503 (1999), hep-lat/9811018.

[GHR01] L. Giusti, C. Hölbling and C. Rebbi, *Light quark masses with overlap fermions in quenched QCD*, Phys. Rev. **D64**, 114508 (2001), hep-lat/0108007.

[GHS02a] C. Gattringer, R. Hoffmann and S. Schaefer, *Setting the scale for the Lüscher-Weisz action*, Phys. Rev. **D65**, 094503 (2002), hep-lat/0112024.

[GHS02b] C. Gattringer, R. Hoffmann and S. Schaefer, *The topological susceptibility of SU(3) gauge theory near $T_c$*, Phys. Lett. **B535**, 358–362 (2002), hep-lat/0203013.

[GMGW98] T. Guhr, A. Müller-Groeling and H. A. Weidenmüller, *Random matrix theories in quantum physics: Common concepts*, Phys. Rept. **299**, 189–425 (1998), cond-mat/9707301.

[GMOR68] M. Gell-Mann, R. J. Oakes and B. Renner, *Behavior of current divergences under SU(3)×SU(3)*, Phys. Rev. **175**, 2195–2199 (1968).

[Got78] S. Gottlieb, *Contribution of twist four operators to deep inelastic scattering*, Nucl. Phys. **B139**, 125 (1978).

[GP76] H. Georgi and H. D. Politzer, *Freedom at moderate energies: Masses in color dynamics.*, Phys. Rev. **D14**, 1829 (1976).

[GRS+01] M. Göckeler, P. E. L. Rakow, A. Schäfer, W. Söldner and T. Wettig, *Calorons and localization of quark eigenvectors in lattice QCD*, Phys. Rev. Lett. **87**, 042001 (2001), hep-lat/0103031.

[GRSV01] M. Glück, E. Reya, M. Stratmann and W. Vogelsang, *Models for the polarized parton distributions of the nucleon*, Phys. Rev. **D63**, 094005 (2001), hep-ph/0011215.

[GRV98] M. Glück, E. Reya and A. Vogt, *Dynamical parton distributions revisited*, Eur. Phys. J. **C5**, 461–470 (1998), hep-ph/9806404.

[GW82] P. H. Ginsparg and K. G. Wilson, *A remnant of chiral symmetry on the lattice*, Phys. Rev. **D25**, 2649 (1982).

[H+01] P. Hasenfratz et al., *The construction of generalized Dirac operators on the lattice*, Int. J. Mod. Phys. **C12**, 691–708 (2001), hep-lat/0003013.

[Has98a] P. Hasenfratz, *Prospects for perfect actions*, Nucl. Phys. Proc. Suppl. **63**, 53–58 (1998), hep-lat/9709110.

[Has98b] P. Hasenfratz, *Lattice QCD without tuning, mixing and current renormalization*, Nucl. Phys. **B525**, 401–409 (1998), hep-lat/9802007.

[Hau02] S. Hauswirth, *Light hadron spectroscopy in quenched lattice QCD with chiral fixed-point fermions*, (2002), hep-lat/0204015.

[HERMES01] A. Airapetian et al. (HERMES Collaboration), *Measurement of longitudinal spin transfer to Lambda hyperons in deep-inelastic lepton scattering*, Phys. Rev. **D64**, 112005 (2001), hep-ex/9911017.

[HHK02] A. Hasenfratz, R. Hoffmann and F. Knechtli, *The static potential with hypercubic blocking*, Nucl. Phys. Proc. Suppl. **106**, 418–420 (2002), hep-lat/0110168.

[HIMT02] I. Horváth, N. Isgur, J. McCune and H. B. Thacker, *Evidence against instanton dominance of topological charge fluctuations in QCD*, Phys. Rev. **D65**, 014502 (2002), hep-lat/0102003.

[HJL99] P. Hernandez, K. Jansen and M. Lüscher, *Locality properties of Neuberger's lattice Dirac operator*, Nucl. Phys. **B552**, 363–378 (1999), hep-lat/9808010.

[HK01] A. Hasenfratz and F. Knechtli, *Flavor symmetry and the static potential with hypercubic blocking*, Phys. Rev. **D64**, 034504 (2001), hep-lat/0103029.

[HLN98] P. Hasenfratz, V. Laliena and F. Niedermayer, *The index theorem in QCD with a finite cut-off*, Phys. Lett. **B427**, 125–131 (1998), hep-lat/9801021.

[HLN+02] I. Hip, T. Lippert, H. Neff, K. Schilling and W. Schroers, *Instanton dominance of topological charge fluctuations in QCD?*, Phys. Rev. **D65**, 014506 (2002), hep-lat/0105001.

[Hor99] I. Horváth, *Some answered and unanswered questions about the structure of the set of fermionic actions with GWL symmetry*, (1999), hep-lat/9912030.

[IZ80] C. Itzykson and J. B. Zuber, *Quantum field theory*, International Series In Pure and Applied Physics, New York, USA: McGraw-Hill, 1980.

[Jeg96] B. Jegerlehner, *Krylov space solvers for shifted linear systems*, (1996), hep-lat/9612014.

[JJ91] R. L. Jaffe and X.-D. Ji, *Chiral odd parton distributions and polarized Drell-Yan*, Phys. Rev. Lett. **67**, 552–555 (1991).

[JLQCD97] S. Aoki et al. (JLQCD Collaboration), *Topics in light hadron mass spectrum in quenched QCD*, Nucl. Phys. Proc. Suppl. **53**, 209–211 (1997), hep-lat/9608144.

[JS81] R. L. Jaffe and M. Soldate, *Twist four in the QCD analysis of leptoproduction*, Phys. Lett. **B105**, 467–472 (1981).

[Kap92] D. B. Kaplan, *A Method for simulating chiral fermions on the lattice*, Phys. Lett. **B288**, 342–347 (1992), hep-lat/9206013.

[LDLZ01] K. F. Liu, S. J. Dong, F. X. Lee and J. B. Zhang, *Overlap fermions on a $20^4$ lattice*, Nucl. Phys. Proc. Suppl. **94**, 752–755 (2001), hep-lat/0011072.

[LHPC02] D. Dolgov et al. (LHPC Collaboration), *Moments of nucleon light cone quark distributions calculated in full lattice QCD*, (2002), hep-lat/0201021.

[LM93] G. P. Lepage and P. B. Mackenzie, *On the viability of lattice perturbation theory*, Phys. Rev. **D48**, 2250–2264 (1993), hep-lat/9209022.

[LPPG01] N. Y. Lee, P. V. Pobylitsa, M. V. Polyakov and K. Goeke, *Meson twist-4 parton distributions in terms of twist-2 distribution amplitudes at large $N_c$*, J. Phys. **G27**, L127 (2001), hep-ph/0011166.

[LSS+97] M. Lüscher, S. Sint, R. Sommer, P. Weisz and U. Wolff, *Non-perturbative $\mathcal{O}(a)$ improvement of lattice QCD*, Nucl. Phys. **B491**, 323–343 (1997), hep-lat/9609035.

[LSY98] R. Lehoucq, D. Sorensen and C. Yang, *Arpack users' guide: Solution of large scale eigenvalue problems with implicitly restarted Arnoldi methods*, SIAM Phildelphia, PA, 1998.

[Lüs98] M. Lüscher, *Exact chiral symmetry on the lattice and the Ginsparg-Wilson relation*, Phys. Lett. **B428**, 342–345 (1998), hep-lat/9802011.

[LW82] S. P. Luttrell and S. Wada, *The current product expansion of the two quark process at the twist four level*, Nucl. Phys. **B197**, 290 (1982).

[LW85] M. Lüscher and P. Weisz, *On-shell improved lattice gauge theories*, Commun. Math. Phys. **97**, 59 (1985), [Erratum-ibid. **98**, 433 (1985)].

[LWW81] S. P. Luttrell, S. Wada and B. R. Webber, *The Wilson coefficient functions of four quark operators and the four quark process in deep inelastic scattering*, Nucl. Phys. **B188**, 219 (1981).

[MM94] I. Montvay and G. Münster, *Quantum fields on a lattice*, Cambridge monographs on mathematical physics, Cambridge, UK: Univ. Press, 1994.

[Mor87] A. Morel, *Chiral logarithms in quenched QCD*, J. Phys. (France) **48**, 1111–1119 (1987).

[MRR+53] N. Metropolis, A. W. Rosenbluth, M. N. Rosenbluth, A. H. Teller and E. Teller, *Equation of state calculations by fast computing machines*, J. Chem. Phys. **21**, 1087–1092 (1953).

[MRST98] A. D. Martin, R. G. Roberts, W. J. Stirling and R. S. Thorne, *Scheme dependence, leading order and higher twist studies of MRST partons*, Phys. Lett. **B443**, 301–307 (1998), hep-ph/9808371.

[MRST01] A. D. Martin, R. G. Roberts, W. J. Stirling and R. S. Thorne, *MRST2001: Partons and $\alpha_s$ from precise deep inelastic scattering and Tevatron jet data*, (2001), hep-ph/0110215.

[MS88] G. Martinelli and C. T. Sachrajda, *A lattice calculation of the pion's form-factor and structure function*, Nucl. Phys. **B306**, 865 (1988).

[Nac73] O. Nachtmann, *Positivity constraints for anomalous dimensions*, Nucl. Phys. **B63**, 237–247 (1973).

[Nie99] F. Niedermayer, *Exact chiral symmetry, topological charge and related topics*, Nucl. Phys. Proc. Suppl. **73**, 105–119 (1999), hep-lat/9810026.

[NN81a] H. B. Nielsen and M. Ninomiya, *Absence of neutrinos on a lattice. 1. Proof by homotopy theory*, Nucl. Phys. **B185**, 20 (1981), [Erratum-ibid. B **195**, 541 (1981)].

[NN81b] H. B. Nielsen and M. Ninomiya, *Absence of neutrinos on a lattice. 2. Intuitive topological proof*, Nucl. Phys. **B193**, 173 (1981).

[NN93a] R. Narayanan and H. Neuberger, *Chiral fermions on the lattice*, Phys. Rev. Lett. **71**, 3251–3254 (1993), hep-lat/9308011.

[NN93b] R. Narayanan and H. Neuberger, *Infinitely many regulator fields for chiral fermions*, Phys. Lett. **B302**, 62–69 (1993), hep-lat/9212019.

[NN95] R. Narayanan and H. Neuberger, *A Construction of lattice chiral gauge theories*, Nucl. Phys. **B443**, 305–385 (1995), hep-th/9411108.

[OPAL98] K. Ackerstaff et al. (OPAL Collaboration), *Polarization and forward-backward asymmetry of Lambda baryons in hadronic $Z_0$ decays*, Eur. Phys. J. **C2**, 49–59 (1998), hep-ex/9708027.

[OV98] J. C. Osborn and J. J. M. Verbaarschot, *Thouless energy and correlations of QCD Dirac eigenvalues*, Phys. Rev. Lett. **81**, 268–271 (1998), hep-ph/9807490.

[P$^+$02] J. Pumplin et al., *New generation of parton distributions with uncertainties from global QCD analysis*, (2002), hep-ph/0201195.

[Ple99] D. Pleiter, *Untersuchung der Quantenchromodynamik mit verbesserten Wirkungen*, PhD thesis, Berlin, 1999.

[Pol78] A. M. Polyakov, *Thermal properties of gauge fields and quark liberation*, Phys. Lett. **B72**, 477–480 (1978).

[QCDSF] QCDSF collaboration, *in preparation*.

[QCDSF00] M. Göckeler et al. (QCDSF Collaboration), *Hadron masses and decay constants in quenched QCD*, Nucl. Phys. Proc. Suppl. **83**, 203–205 (2000), hep-lat/9909160.

[QCDSF02a] S. Capitani et al. (QCDSF Collaboration), *Progress towards a lattice determination of (moments of) nucleon structure functions*, Nucl. Phys. Proc. Suppl. **106**, 299–301 (2002), hep-lat/0111012.

[QCDSF02b] M. Göckeler et al. (QCDSF Collaboration), *A lattice study of the spin structure of the $\Lambda$ hyperon*, Phys. Lett. **B545**, 112–118 (2002), hep-lat/0208017.

[QCDSF02c] M. Göckeler et al. (QCDSF Collaboration), *The spin structure of the $\Lambda$ hyperon in quenched lattice QCD*, Nucl. Phys. Proc. Suppl. **106**, 305–307 (2002), hep-lat/0110057.

[Sha90] S. R. Sharpe, *Chiral logarithms in quenched $m_\pi$ and $f_\pi$*, Phys. Rev. **D41**, 3233 (1990).

[Sha93] Y. Shamir, *Chiral fermions from lattice boundaries*, Nucl. Phys. **B406**, 90–106 (1993), hep-lat/9303005.

[Som94] R. Sommer, *A New way to set the energy scale in lattice gauge theories and its applications to the static force and $\alpha_s$ in SU(2) Yang-Mills theory*, Nucl. Phys. **B411**, 839–854 (1994), hep-lat/9310022.

[Sor92] D. Sorensen, *Implicit application of polynomial filters in a k–step Arnoldi method*, SIAM J. Matrix Anal. Appl. **13**, 357–385. (1992).

[SS98] T. Schäfer and E. V. Shuryak, *Instantons in QCD*, Rev. Mod. Phys. **70**, 323–426 (1998), hep-ph/9610451.

[SSS01] S. Schaefer, A. Schäfer and M. Stratmann, *Impact of higher order and soft gluon corrections on the extraction of higher twist effects in DIS*, Phys. Lett. **B514**, 284–292 (2001), hep-ph/0105174.

[SW85] B. Sheikholeslami and R. Wohlert, *Improved continuum limit lattice action for QCD with Wilson fermions*, Nucl. Phys. **B259**, 572 (1985).

[SY82] B. Svetitsky and L. G. Yaffe, *Critical behavior at finite temperature confinement transitions*, Nucl. Phys. **B210**, 423 (1982).

[tH76] G. 't Hooft, *Computation of the quantum effects due to a four-dimensional pseudoparticle*, Phys. Rev. **D14**, 3432–3450 (1976).

[UKQCD93] C. R. Allton et al. (UKQCD Collaboration), *Gauge invariant smearing and matrix correlators using Wilson fermions at $\beta = 6.2$*, Phys. Rev. **D47**, 5128–5137 (1993), hep-lat/9303009.

[vdV92] H. A. van der Vorst, *Bi-CGStab: A fast and smoothly converging variant of Bi-CG for the solution of non-symmetric linear systems*, SIAM J. Scient. Stat. Comput. **13**, 631–644 (1992).

[VM92] M. Virchaux and A. Milsztajn, *A measurement of $\alpha_s$ and higher twists from a QCD analysis of high statistics $F_2$ data on hydrogen and deuterium targets*, Phys. Lett. **B274**, 221–229 (1992).

[vNZ91] W. L. van Neerven and E. B. Zijlstra, *Order $\alpha_s^2$ contributions to the deep inelastic Wilson coefficient*, Phys. Lett. **B272**, 127–133 (1991).

[Vog99] A. Vogt, *On soft gluon effects in deep-inelastic structure functions*, Phys. Lett. **B471**, 97–102 (1999), hep-ph/9910545.

[Wil74] K. G. Wilson, *Confinement of quarks*, Phys. Rev. **D10**, 2445–2459 (1974).

[Wil77] K. G. Wilson, *Quarks and strings on a lattice, New Phenomena In Subnuclear Physics. Part A. Proceedings of the First Half of the 1975 International School of Subnuclear Physics, Erice, Sicily, July 11 - August 1, 1975, ed. A. Zichichi*, Plenum Press, New York, 1977.

[WRD+92] L. W. Whitlow, E. M. Riordan, S. Dasu, S. Rock and A. Bodek, *Precise measurements of the proton and deuteron structure functions from a global analysis of the SLAC deep inelastic electron scattering cross-sections*, Phys. Lett. **B282**, 475–482 (1992).

[ZvN92] E. B. Zijlstra and W. L. van Neerven, *Order $\alpha_s^2$ QCD corrections to the deep inelastic proton structure functions $F_2$ and $F(L)$*, Nucl. Phys. **B383**, 525–574 (1992).

# Acknowledgments

It is a pleasure to thank for many indispensable contributions to this work.

Andreas Schäfer provided the enjoyable environment and introduced me into the various interesting subjects of this thesis. I am indebted to Christof Gattringer, Meinulf Göckeler, Paul Rakow and Marco Stratmann for patiently sharing their insight and answering innumerable questions. Without their enthusiasm, ideas and experience I would certainly have failed. I also profited a lot from discussions with Peter Hasenfratz, Simon Hauswirth, Holger Hehl, Roland Hoffmann, Christian Lang and Ferenc Niedermayer. I also want to thank all the other members of the QCDSF and BGR collaborations.

Lattice QCD is hardly possible without extensive computer resources. Therefore, I am grateful for the opportunity to use the Quadrix computers in Zeuthen as well as the SR8000-F1 at Leibniz Rechenzentrum in Munich. Finally, I thank Freistaat Bayern, DFG and BMBF for financial support during the last years.